OSMOTIC POWER FOR REMOTE COMMUNITIES IN QUEBEC

Jonathan Maisonneuve

A Thesis

In the Department

of

Electrical and Computer Engineering

Presented in Partial Fulfillment of the Requirements

For the Degree of

Doctor of Philosophy (Electrical and Computer Engineering) at

Concordia University

Montreal, Quebec, Canada

August 2015

CONCORDIA UNIVERSITY

SCHOOL OF GRADUATE STUDIES

This is to certify that the thesis prepared

By: Jonathan Maisonneuve

Entitled: Osmotic Power for Remote Communities in Quebec

and submitted in partial fulfillment of the requirements for the degree of

Doctor of Philosophy (Electrical and Computer Engineering)

complies with the regulations of the University and meets the accepted standards with respect to originality and quality.

Signed by the final examining committee:

Dr. D. Dysart-Gale	Chair
Dr. M. El-Hawary	External Examiner
Dr. A. Athienitis	External to Program
Dr. L. A. C. Lopes	Examiner
Dr. H. Zad	Examiner
Dr. P. Pillay	Thesis Supervisor

Approved by:

Dr. A. R. Sebak, Graduate Program Director

August 12, 2015

Dr. A. Asif, Dean
Faculty of Engineering and Computer Science

ABSTRACT

Osmotic Power for Remote Communities in Quebec

Jonathan Maisonneuve, Ph.D.

Concordia University, 2015

This work investigates the process of pressure retarded osmosis (PRO) for salinity gradient energy conversion in power production applications. A mathematical model of the PRO process is developed with consideration for non-ideal effects including internal concentration polarization, external concentration polarization, and spatial variations that are caused by mass transfer and by pressure drop along the length of the membrane. A mathematical model of the osmotic power plant is also developed with consideration for pre-filtration and pick-up head, and for mechanical and electrical equipment efficiencies. A distinction is made between the gross power developed by the PRO process, and the net power available to the grid after parasitic loads are accounted for. This distinction leads to observation of a trade-off that exists between the different non-ideal effects. A method is developed for adjusting operating conditions in order to minimize the overall impact of non-ideal effects and to achieve maximum net power. Important improvements in net power densities are realized as compared to results obtained when general rules of thumb are used for operating conditions. The mathematical model is validated by experimental investigation of PRO at the bench-scale. It is found that test conditions generally used in the literature may not be appropriate for power production applications. Test conditions which strike a balance between pressure drop and other non-ideal effects may provide more realistic results.

An analog electric circuit is developed for a simplified PRO process and osmotic power plant. The analog circuit is used to develop strategies for controlling operating conditions of the system, including by control of the load and by control of a flush valve. Both of these provide satisfactory tracking of the desired operating conditions and can also be used for tracking the maximum power point. The proposed strategies respond quickly to changes in source and load.

The osmotic power potential is evaluated for remote micro-grids in Quebec. The osmotic power potential of selected rivers is calculated and compared against peak power demand of nearby communities. In each case, only a small portion of river flow is needed to satisfy the peak power demand of the micro-grids. This suggests that osmotic power can serve as a reliable source of electricity in such applications. An osmotic power plant prototype is designed for Quebec and its potential for power production in remote communities is evaluated.

ACKNOWLEDGEMENTS

I would like to sincerely thank my supervisor Dr. Pragasen Pillay for his constant guidance and trusted direction throughout my Ph.D studies. I hope to emulate his honesty, integrity and wisdom throughout my career and beyond.

I would like to thank Dr. Claude B. Laflamme from Hydro-Québec for his close collaboration. It was a pleasure to work with such a passionate researcher and interesting individual.

I would also like to thank Mr. Guillaume Clairet from H_2O Innovation and Dr. Catherine Mulligan from Concordia University for their many contributions to the Osmotic Power (OSMOP) research project.

Many thanks to all of the professors and colleagues in the Power Electronics and Energy Research (PEER) group for their help and insights. It is a great privilege to have been part of such a world-class research group.

I would like to express my deepest gratitude to my parents for their unconditional support throughout my entire life, to my beloved wife Ariane Avril, for her emotional support and continuous encouragement, and to my two children Eva and Henri.

This research work was done as part of the NSERC/Hydro-Québec Industrial Research Chair entitled “Design and Performance of Special Electrical Machines”. It was also supported in part by the Fonds de Recherche du Québec - Nature et Technologies, and in part by Mitacs.

TABLE OF CONTENTS

LIST OF FIGURES

LIST OF TABLES

NOMENCLATURE

CA	Cellulose Acetate
ICP	Internal Concentration Polarization
ECP	External Concentration Polarization
FO	Forward Osmosis
OE	Osmotic Equilibrium
OSMOP	Osmotic Power Project
PRO	Pressure Retarded Osmosis
RO	Reverse Osmosis
TFC	Thin Film Composite

LIST OF SYMBOLS

A	Water permeability (m s^{-1} Pa^{-1})
a_c	Cross sectional area (m^2)
a_m	Membrane surface area (m^2)
B	Salt permeability (m s^{-1})
C	Salt capacitance (m)
c	Concentration (g l^{-1})
D	Salt diffusion coefficient (m^2 s^{-1})
d_h	Hydraulic diameter (m)
F	Turbulence correction factor
f	Friction factor
h	Channel height (m)
h*	Effective channel height (m)
i_v	Van't Hoff coefficient
J_w	Water permeate flux (m^3 s^{-1} m^{-2})
J_s	Salt permeate flux (kg s^{-1} m^{-2})
k	Mass transfer coefficient (m s^{-1})
L	Membrane length (m)
M	Molar mass (kg mol^{-1})
$\dot{m}$	Mass flow rate (kg s^{-1})
m	Number of finite layers in membrane profile
n	Number of finite pieces in membrane length

P	Hydraulic pressure (Pa)
R	Salt rejection ratio
R	Salt resistance (s m^{-3})
R	Water resistance (Pa s m^{-3})
R_g	Gas constant (J mol^{-1} K^{-1})
Re	Reynolds number
r	Radius (m)
S	Structure parameter (m)
Sc	Schmidt number
Sh	Sherwood number
T	Temperature (K)
t	Time (s)
u	Velocity (m s^{-1})
$\dot{V}$	Volumetric flow rate (m^3 s^{-1})
W	Power (W)
w	Power density (W m^{-2})
w	Width (m)
x	Axis along the membrane length
y	Axis perpendicular to membrane surface

Greek symbols:

Γ	Osmotic pressure (Pa)
α	Permeate to feed volume ratio

β	Draw to feed volume ratio
γ	Hydraulic to osmotic pressure ratio
δ	Boundary layer thickness (m)
ε	Support layer porosity
η	Efficiency
θ	Active membrane layer thickness (m)
κ	Mass transfer constant
λ	Support layer thickness (m)
μ	Viscosity (Pa s)
ρ	Density (kg m^{-3})
ρ	Salt resistivity (s m^{-1})
ρ	Water resistivity (Pa s m^{-1})
τ	Support layer tortuosity
φ	Friction factor constant

Subscripts:

b	Bulk
D	Draw
d	Diffusion
e	Electric
F	Feed
i	Piece of membrane length
j	Layer of membrane profile

m	Membrane
P	Permeate
S	Support layer
s	Salt
v	Convection
w	Water

1. INTRODUCTION

1.1. Background

One of the great challenges of our time is for society to adapt such that its activities become sustainable. Climate change and other socio-economic factors have created the incentive for renewable energy as an alternative to traditional fossil fuels [1]. The earth's hydrological cycle is a huge store of renewable energy, among which a significant portion is available in the form of salinity gradients. Solar radiation falling on the sea is absorbed by water as it is separated from solutes and evaporates into the atmosphere. When freshwater precipitation returns to the sea that potential energy is dissipated into the environment as heat and entropy. This source of power was first recognized in 1954 [2], when it was observed that the energy available from a river meeting the ocean is equivalent to that of a waterfall over 200 m high, or 0.66 kWh of energy per m^3 of freshwater. This means that all over the world, where rivers meet oceans there is a potential for power production. The global potential for this power is estimated at 2.6 TW [3], enough to supply 20% of the world's annual energy needs [4].

Several processes for salinity gradient energy conversion have been proposed [5, 6, 7, 8, 9]. Among the most developed is pressure retarded osmosis (PRO) [10, 11]. PRO is a membrane-based process that exploits the natural phenomenon of osmosis, which is driven by the chemical potential difference between solutions of different concentrations. In PRO a hydraulic pressure is applied to a volume of concentrated 'draw' solution, which is introduced to one side of a semi-permeable membrane. When a volume of

diluted ‘feed’ solution is introduced on the other side of the membrane, osmosis will cause water to permeate from the feed side to the draw side. The expanding volume of high-pressure draw solution can then be depressurized across a turbine and generator to produce electricity.

The PRO concept was proposed by Norman [12, 13] in 1974 and pioneered by Loeb [14, 15, 16, 17] who conducted the first experimental verifications of the concept and developed the basic osmotic power plant configuration that is used today. Over the last several years the PRO concept has gained momentum with the number of publications on the subject rising sharply [18]. This has been primarily driven by oil prices, but also due to advances in pressure exchanger and membrane performance. In 2009 the Norwegian power company Statkraft placed the first osmotic power prototype into operation, marking a milestone in the technology’s development [19].

The potential applications for PRO (and salinity gradient energy conversion in general) are many. They include power production in natural estuaries where rivers meet oceans, in coastal settlements where wastewater is discharged into the sea, and at super-concentrated water bodies such as the Great Salt Lake and the Dead Sea [20, 21]. It also has potential for power production from waste heat via the osmotic heat engine [22], for hybrid power production with other renewables [23] and for energy storage via a closed loop PRO and RO cycle [24]. Perhaps the most immediate application will be for energy recovery from super-concentrated waste at desalination plants [25, 26, 27].

Salinity gradient energy offers several advantages over other forms of energy. Perhaps the most important advantage is the consistency and predictability of the source, as compared to many other sources of renewable energy. Fluctuations in river and ocean concentration are usually minor and gradual. Energy density of salinity gradients also compares very favorably against other marine sources, as well as other common renewables such as wind and solar [3, 28].

Due to its predictability, salinity gradient energy may also find niche applications for stand-alone power production in isolated locations. In remote regions of Quebec where there are significant water resources, salinity gradient energy could possibly replace diesel-powered generating stations. The logistical challenges of transporting fuel into these remote regions, makes diesel-power production an expensive operation. Electricity generation in such regions currently costs an average of 0.46 $/kWh, and in some cases over 1.00 $/kWh [29]. There is also a strong environmental incentive for alternatives because electricity generation for a typical remote micro-grid in Quebec produces 10 000 tonnes of equivalent CO_2 emissions every year [30].

Energy conversion by PRO produces no greenhouse gas emissions and is environmentally benign. Osmotic power plants are run-of-river systems that require no damns (although they could also be integrated with conventional hydro-power plants). When only a small portion of river flow is consumed, the process should have limited impacts on local ecosystems [31]. However, estuaries are often ecologically sensitive areas and further investigation is needed. Other environmental impacts include disposal

of membrane units, and discharge of chemicals used for membrane maintenance. Detailed life cycle analysis of the technology has not yet been conducted.

1.2. Objectives

The objectives of this thesis are:

- Develop a detailed mathematical model for the PRO process and osmotic power plant
- Experimentally validate the PRO mathematical model
- Develop an analog electric circuit to model the PRO process and osmotic power plant
- Improve PRO power production by controlling operating conditions
- Evaluate the potential of PRO for power production in remote regions of Quebec

1.3. Thesis Outline

The thesis is divided into six chapters. Chapter two presents the mathematical model for the PRO process and osmotic power plant. This model is among the first in the literature to consider polarization across the feed side boundary layer, spatial variations along the membrane, cross-flow pressure drop, and system scale losses. The model is used to develop a novel approach to improving PRO performance, which consists of adjusting operating conditions in order to obtain significant increases in net power. In chapter three, an experimental investigation of PRO power is conducted and the results are used to validate the mathematical model across a range of operating conditions. A commercial

semi-permeable membrane is tested and yields power density that is among the highest reported in the literature. An important distinction between gross power and net power is made, and this leads to a novel analysis of the effect of operating conditions on power. Chapter four presents an analog electric circuit model for the PRO process and power plant, which is the first of its kind published in the literature. The analog circuit is a powerful tool for analysis and is used here to investigate control strategies for PRO power systems. In chapter five, the power potential of selected rivers in Quebec is evaluated. Also, the design is presented for an osmotic power plant prototype, which may become the first in Quebec and North America. Chapter six concludes the thesis and proposes future research.

2. MATHEMATICAL MODEL OF PRESSURE RETARDED OSMOSIS POWER SYSTEM

2.1. Introduction

Power production by PRO can be improved by reducing non-ideal effects at the semi-permeable membrane and throughout the osmotic power plant. Typically, research and development efforts have focused on improving membrane performance, especially by addressing the trade-off between water permeability and solute selectivity [32]. This approach requires a detailed understanding of the mass transport phenomena across the membrane. Most PRO mass transport models are based on the solution-diffusion model, which describes mass transport as a function of diffusion and convection [33]. The solution-diffusion model was first applied to PRO by [34], and then by many others, with minor changes and improvements [35, 36, 37, 38, 39].

These efforts have led to very important improvements in PRO membrane technology. Figure 1 provides a timeline of experimentally verified membrane power densities [10, 11]. The figure shows steady improvements since the technology's conception in the 1970s, and then rapid improvements in recent years. The threshold of 5 W/m^2 which was proposed as a target for commercial viability [40, 41, 42] has now been surpassed in several laboratories [38, 43, 44].

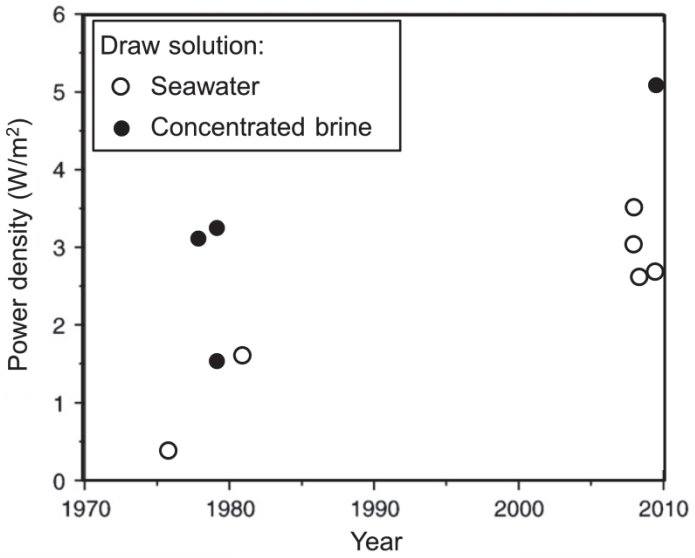

Figure 1. History of experimentally obtained power densities by PRO process with different draw solutions, modified from [10]

Another approach to improving PRO power involves considering the entire osmotic power plant. At this scale, additional non-ideal effects must be considered, both in the membrane module and throughout the system. This increases the complexity of the model but can lead to important improvements in power. For example, considering PRO at this scale reveals several trade-offs in operating conditions which can be controlled and optimized [45, 46]. Another advantage of this approach is that results can more accurately translate to commercial installations, whereas small scale simulations and experiments tend to over-estimate power. Only recently have some few models been proposed for considering the dynamics in commercial scale membrane modules [47, 48] and in full scale osmotic power plants [49].

In this chapter, a detailed mathematical model of the PRO process is developed, with consideration for several non-ideal effects including concentration polarization, spatial

variations in concentration and flow rate, and pressure drop along the membrane. The scale of the model is also expanded to consider dynamics at the power plant scale, including pick-up head and filtration losses and mechanical and electrical equipment losses. This is among the most detailed mathematical models in the literature and one of only a few to consider osmotic power at the power plant scale. The model is used to examine the effect of operating conditions on power output. From this, a novel method to improving system performance is developed which is based on adjusting operating conditions in order to significantly increase power.

2.2. Osmotically Driven Membrane Processes

Osmotic pressure is defined as the hydraulic pressure required to oppose permeate flow across a semi-permeable membrane, when solutions with different concentrations are present on opposite sides of the membrane. This naturally occurring flow of solvent is due to the chemical potential (or Gibbs free energy) difference that exists between solutions with different concentrations. Certain empirical relations for osmotic pressure Γ have been proposed [50] but it can reasonably be estimated by [51]:

$$\Gamma \approx i_v \cdot R_g \cdot T \cdot c/M \quad (1)$$

i_v is the number of ions in the solute, R_g is the ideal gas constant, T is the absolute temperature, c is the solution concentration, and M is the molar mass of the solute. Throughout this work the solute is assumed to be sodium chloride (NaCl), for which i_v = 2 and M = 58.44 g/mol.

The process of osmosis is sometimes referred to as forward osmosis (FO) and is illustrated in Figure 2 (a). The flow of solvent is driven by the difference in osmotic pressure $\Delta\Gamma$ that exists because of the concentration difference between the solutions. When some hydraulic pressure ΔP is applied against the osmotic pressure difference, the permeate flow rate is reduced. This process is known as pressure retarded osmosis (PRO), illustrated in Figure 2 (b). When hydraulic pressure increases to match the osmotic pressure $\Delta P = \Delta\Gamma$ the system reaches osmotic equilibrium (OE) and there is no permeate (Figure 2 (c)). When hydraulic pressure is greater than the osmotic pressure $\Delta P > \Delta\Gamma$ the permeate flow is reversed. This process is known as reverse osmosis (RO) and is shown in Figure 2 (d). Within the range of PRO ($0 < \Delta P < \Delta\Gamma$) there is an energy potential because both flow rate and hydraulic pressure are positive. In a sense, the direction of permeate flow rate can be considered 'up-hill'.

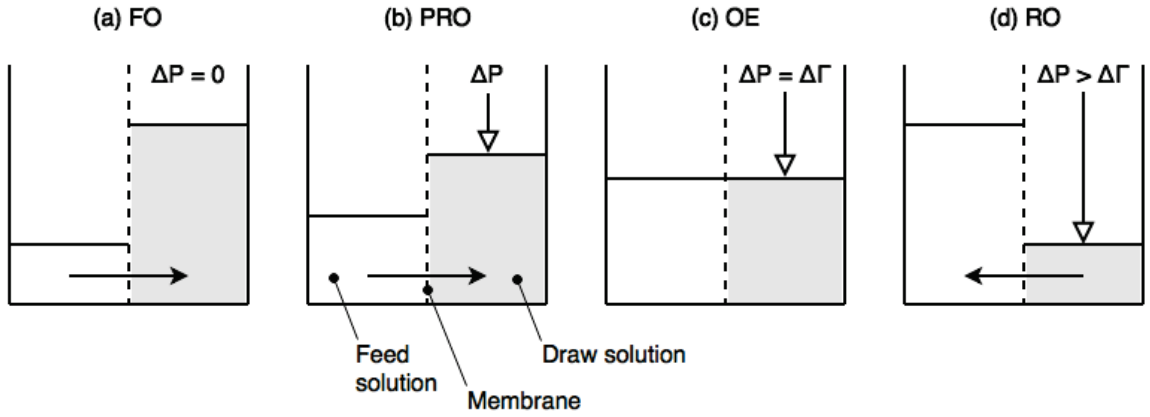

Figure 2. Osmotically driven membrane processes: (a) forward osmosis (FO), (b) pressure retarded osmosis (PRO), (c) osmotic equilibrium (OE), and (d) reverse osmosis (RO)

During PRO it is convention to refer to the diluted solution (or freshwater) as feed solution, and the concentrated solution (or seawater) as draw solution.

2.3. Water and Salt Permeate

The basic relationship that describes water permeate flux J_w (volumetric flow rate per unit membrane area) across a semi-permeable membrane is:

$$J_w = A \cdot (\Delta\Gamma_m - \Delta P) \quad (2)$$

A is the membrane water permeability, ΔP is the hydraulic pressure difference across the membrane, and $\Delta\Gamma_m$ is the osmotic pressure difference across the membrane. Figure 3 illustrates the relationship between water permeate flux and hydraulic pressure difference over the range between FO and RO. As ΔP increases J_w is reduced, until finally $J_w = 0$ when $\Delta P = \Delta\Gamma_m$.

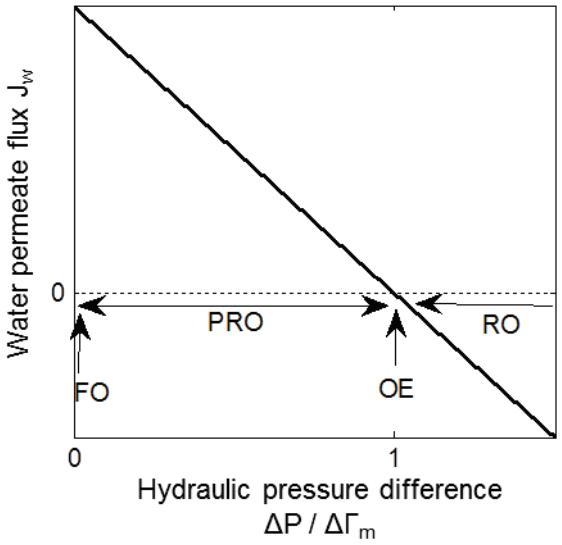

Figure 3. Water permeate flux J_w across a semi-permeable membrane as a function of hydraulic pressure difference ΔP (normalized over the osmotic pressure difference $\Delta\Gamma_m$)

From equation (2) it is clear that to maximize water permeate flux it is desirable that the membrane be highly water permeable. Practically however, this is limited by the competing desire for the membrane to be highly selective to salts. Because the membrane is not perfectly impermeable to salt, a small amount will leak through the membrane from the draw side to the feed side. This process is driven by diffusion, and leads to the movement of salt in the direction opposite to the water permeate and is therefore referred to as reverse salt flux. Because of its undesirability, it is also sometimes referred to as reverse salt leakage. The basic relationship that describes reverse salt flux J_s (mass flow rate per unit membrane area) in PRO is:

$$J_s = B \cdot \Delta c_m \tag{3}$$

B is the membrane salt permeability, and Δc_m is the concentration difference across the membrane. Recent efforts in membrane and material sciences have been made to optimize the trade-off between water permeability A and salt permeability B [32].

Figure 4 shows water and salt flux across a short section of hollow fiber membrane. Water permeate flux is driven by the balance between osmotic and hydraulic pressure. Reverse salt flux is driven by the concentration difference across the membrane. The semi-permeable membrane is composed of a thin active layer of thickness θ and a porous support layer of thickness λ. Feed solution flows on the inside of the fiber and draw solution flows on the outside. Generally, several thousand hollow fibers are bundled together within a single commercial membrane module [52]. Other membrane configurations include spiral wound [53] and flat sheet stacks [54, 55].

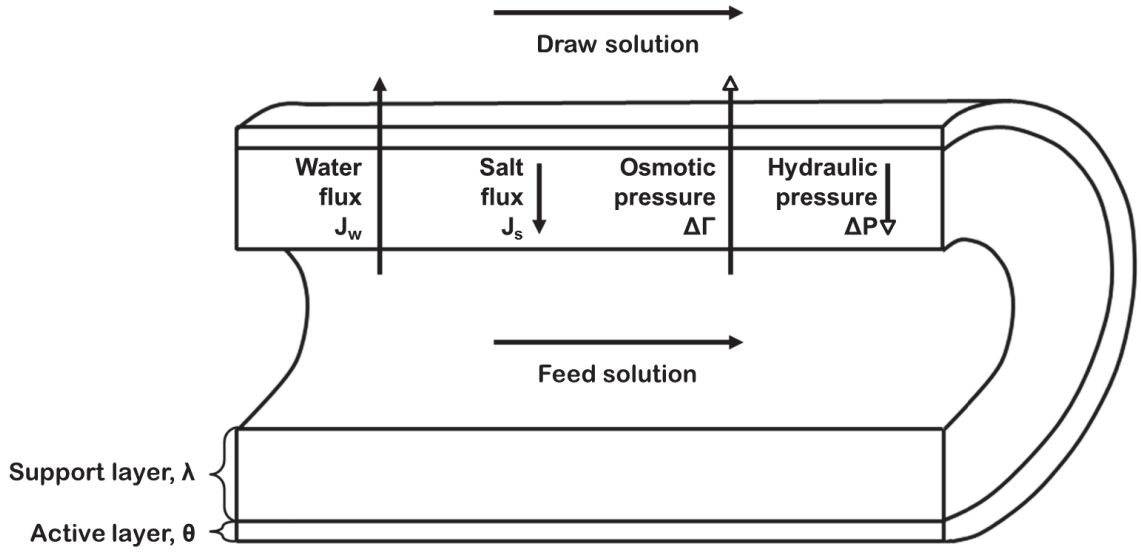

Figure 4. Water and salt flux across a short section of hollow fiber membrane

2.4. Gross PRO Power

Power from the PRO process is available from the expanding volume of high-pressure draw solution. Water permeate flux J_w describes the rate of expansion of the draw side solution and hydraulic pressure difference ΔP is the exploitable pressure gradient. It follows then that gross PRO power density w_{gross}^{PRO} (power per unit membrane area) is the product of the two:

$$w_{gross}^{PRO} = J_w \cdot \Delta P \tag{4}$$

The objective therefore in PRO is to increase both J_w and ΔP. These are inversely proportional however. By combining equations (2) and (4) it is possible to define the theoretical maximum power w_{max} of the PRO process. Gross PRO power density w_{gross}^{PRO} is written here as a function of hydraulic pressure difference ΔP:

$$w_{gross}^{PRO} = A \cdot (\Delta\Gamma_m - \Delta P) \cdot \Delta P \tag{5}$$

Solving for $dW_{gross}^{PRO} / d\Delta P = 0$ gives the theoretical maximum power point $\Delta P = \Delta\Gamma_m / 2$, as shown from the following operations:

$$\frac{d\, w_{gross}^{PRO}}{d\, \Delta P} = 0 \tag{6}$$

$$\frac{d\, A \cdot (\Delta\Gamma_m \cdot \Delta P - \Delta P^2)}{d\, \Delta P} = 0 \tag{7}$$

$$\frac{d\, \Delta\Gamma_m \cdot \Delta P}{d\, \Delta P} = \frac{d\, \Delta P^2}{d\, \Delta P} \tag{8}$$

$$\Delta\Gamma_m = 2 \cdot \Delta P \tag{9}$$

$$\Delta P = \frac{\Delta\Gamma_m}{2} \tag{10}$$

Therefore $w_{gross}^{PRO} = w_{max}$ when $\Delta P = \Delta\Gamma_m / 2$. Substituting this result in to equation (5) gives the maximum power available from the PRO process:

$$w_{max} = A \cdot \left(\frac{\Delta\Gamma_m}{2}\right)^2 \tag{11}$$

The relationship between gross PRO power density and hydraulic pressure difference is presented in Figure 5 and shows the theoretical maximum power point for the PRO process.

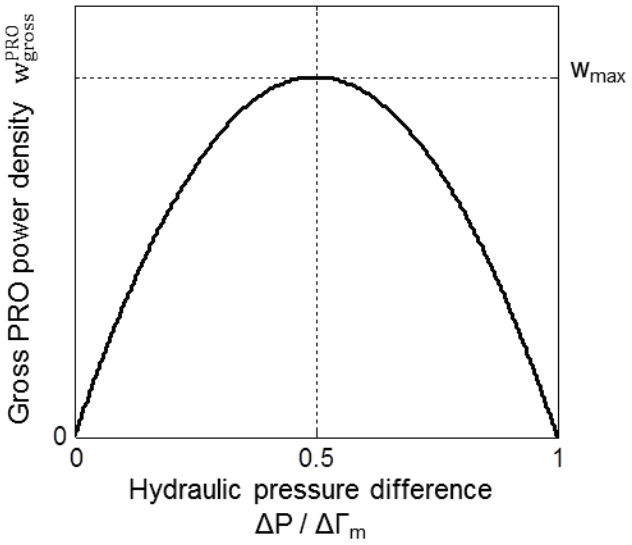

Figure 5. Gross PRO power density w_{gross}^{PRO} as a function of hydraulic pressure difference ΔP (normalized over the osmotic pressure difference $\Delta\Gamma_m$), where the theoretical maximum power w_{max} is obtained when $\Delta P = \Delta\Gamma_m / 2$

This result indicates that in order to produce maximum power from the PRO process only half of the osmotic pressure gradient can be exploited. In other words, for maximum PRO power production only half of the potential energy available between the solutions can be extracted. All of the energy could theoretically be extracted by setting ΔP just slightly lower than $\Delta\Gamma_m$, however at this point, water permeate approaches zero, and hence so does power. The trade-off between power production and energy harvesting in PRO has previously been analyzed [56].

Values of PRO power are generally normalized over the membrane surface area and expressed in W/m^2. This provides a measure of the systems efficiency because system cost is proportional to the surface area of the membrane. It also provides a measure of membrane performance. This is useful because until now membrane technology has been

the focus of most PRO power research and development. A power density of 5 W/m^2 has been proposed as a target for the technology to reach commercial viability [40].

2.5. Concentration Polarization

2.5.1. Modeling Concentration Polarization

Concentration polarization refers to the non-linear concentration gradient that develops across a semi-permeable membrane due to the accumulation of water and salt at the membrane surfaces and within the membrane support structure [57, 58]. The result is that the effective concentration difference across the membrane is much less than the concentration difference between the bulk solutions. Since osmotic pressure is a function of concentration, this ultimately leads to a drop in water permeate flux and power density.

A representation of the steady-state concentration profile across a semi-permeable membrane is provided in Figure 6. The bulk feed and draw concentrations $c_{F,b}$ and $c_{D,b}$ are initially supplied to the membrane. Across the draw side boundary layer δ_D the concentration reduces to $c_{D,m}$, which is the concentration on the draw side of the membrane skin. Across the feed side boundary layer δ_F the concentration increases to $c_{F,S}$, which is the concentration at the interface between the feed solution and the support layer. $c_{F,m}$ is the concentration on the feed side of the membrane skin. The effective concentration difference across the active membrane layer is therefore $\Delta c_m = c_{D,m} - c_{F,m}$, which is significantly less than the bulk concentration difference $\Delta c_b = c_{D,b} - c_{F,b}$. The particular orientation shown in Figure 6, with the active layer facing the draw solution

and the support layer facing the feed solution, has been shown to minimize polarization [58].

Concentration drop across the membrane support layer is generally referred to as internal concentration polarization (ICP), and concentration drop across the boundary layers is called external concentration polarization (ECP).

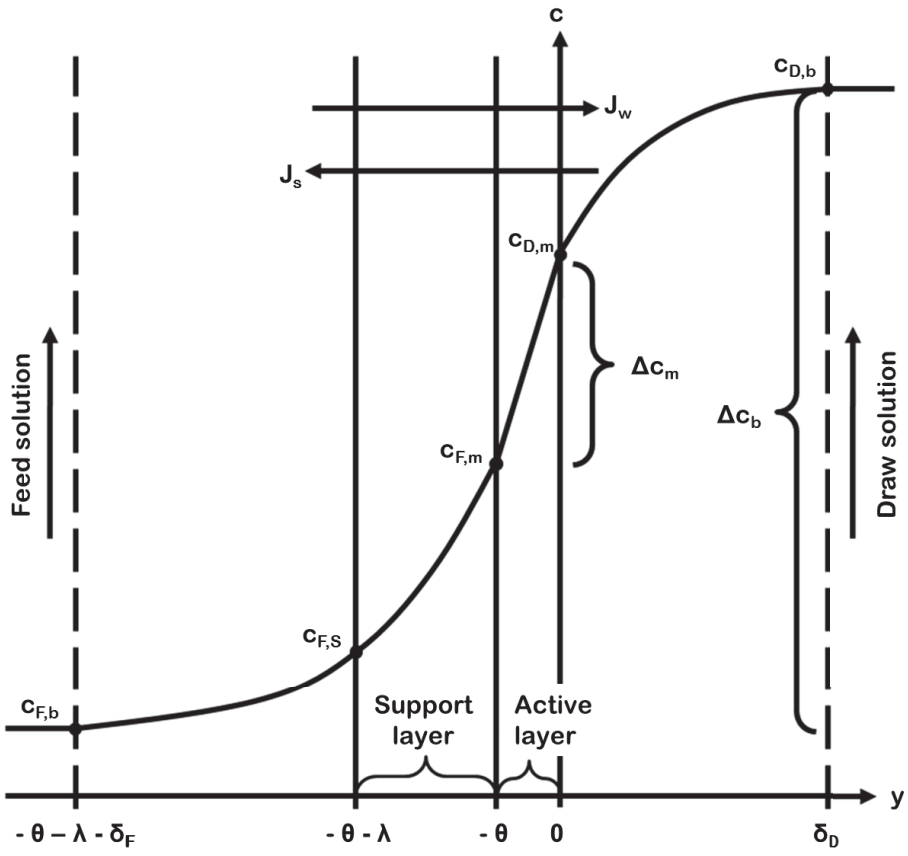

Figure 6. Concentration profile across a semi-permeable membrane due to polarization

The resulting steady-state concentration profile across the membrane is the equilibrium between diffusion and convection as described by the solution-diffusion model [33]:

$$J_s = D \cdot \frac{dc}{dy} - J_w \cdot c \tag{12}$$

The first term in this equation $D \cdot dc / dy$ accounts for diffusion as driven by the concentration gradient in the y-axis (perpendicular to the membrane surface), where D is the salt diffusion coefficient, which is a measure of the solution's permeability to salt. The second term in the equation $J_w \cdot c$ accounts for salt carried by convection (carried by the water permeate), where c is concentration at the point of interest across the profile (y-axis). Convection is osmotically-driven and is in the opposite direction to salt flux.

The balance of the first and second terms gives the salt flux across the differential element dy. By the conservation of mass, at steady-state the salt flux across the polarization layers must be equal to salt permeate across the membrane, and therefore equations (3) and (12) can be combined.

$$D \cdot \frac{dc}{dy} - J_w \cdot c = B \cdot \Delta c_m \tag{13}$$

This provides a differential equation that can be used to solve for the concentration at any or all points across the membrane profile. The general solution of the equation obtained by method of separation is:

$$c = Z \cdot \exp\left(\frac{J_w}{D} \cdot y\right) - B \cdot \frac{\Delta c_m}{J_w} \tag{14}$$

Z is a constant.

Using the boundary conditions for c and y described in Figure 6, expressions for $c_{F,S}$, $c_{F,m}$ and $c_{D,m}$ can be defined as,

$$c_{F,S} = \left[\left(c_{F,b} + B \cdot \frac{\Delta c_m}{J_w}\right) \cdot \exp\left(J_w \cdot \frac{\delta_F}{D_F}\right)\right] - B \cdot \frac{\Delta c_m}{J_w} \tag{15}$$

$$c_{F,m} = \left[\left(c_{F,b} + B \cdot \frac{\Delta c_m}{J_w}\right) \cdot \exp\left(J_w \cdot \left(\frac{\delta_F}{D_F} + \frac{\lambda}{D_S}\right)\right)\right] - B \cdot \frac{\Delta c_m}{J_w} \tag{16}$$

$$c_{D,m} = \left[\left(c_{D,b} + B \cdot \frac{\Delta c_m}{J_w}\right) \cdot \exp\left(-J_w \cdot \frac{\delta_D}{D_D}\right)\right] - B \cdot \frac{\Delta c_m}{J_w} \tag{17}$$

Finally, combining (16) and (17) provides an expression for the effective concentration difference $\Delta c_m = c_{D,m} - c_{F,m}$ across the active membrane layer [34, 36].

$$\Delta c_m = \frac{c_{D,b} \cdot \exp\left(-J_w \cdot \frac{\delta_D}{D_D}\right) - c_{F,b} \cdot \exp\left(J_w \cdot \left(\frac{\delta_F}{D_F} + \frac{\lambda}{D_S}\right)\right)}{1 + \frac{B}{J_w} \cdot \left[\exp\left(J_w \cdot \left(\frac{\delta_F}{D_F} + \frac{\lambda}{D_S}\right)\right) - \exp\left(-J_w \cdot \frac{\delta_D}{D_D}\right)\right]} \tag{18}$$

This expression has been derived elsewhere in the literature [35] [36] [38], however in those cases polarization across the feed side boundary layer was neglected. Although polarization across this layer is generally minor [59], this expression nonetheless improves upon previous work by providing a more complete solution that requires very little additional computation.

The expression can be slightly modified to obtain a more useful form:

$$\Delta c_m = \frac{c_{D,b} \cdot \exp(-J_w \cdot k_D) - c_{F,b} \cdot \exp\left(J_w \cdot \left(k_F + \frac{S}{D_F}\right)\right)}{1 + \frac{B}{J_w} \cdot \left[\exp\left(J_w \cdot \left(k_F + \frac{S}{D_F}\right)\right) - \exp(-J_w \cdot k_D)\right]} \quad (19)$$

k is the mass transfer coefficient and S is the support layer's structure parameter.

In general form, the mass transfer coefficient k is a function of the Sherwood number Sh, which is a function of the Reynolds number Re and the Schmidt number Sc [20]:

$$k = \frac{D}{\delta} \quad (20)$$

$$k = Sh \cdot \frac{D}{d_h} \quad (21)$$

$$k = \kappa_1 \cdot Re^{\kappa_2} \cdot Sc^{\kappa_3} \cdot \frac{D}{d_h} \quad (22)$$

κ_1, κ_2, and κ_3 are constants, and d_h is the hydraulic diameter of the flow channel. Because the mass transfer coefficient is included as an exponential term in equation (19) it is very important to accurately define it. This can be challenging however, with many different expressions having been proposed in the literature and with relative errors on the order of ± 30% [60, 61, 62, 63, 64, 65, 66].

The structure parameter S can be determined through standard experimental testing [67] and is generally available from the membrane manufacturer. It is a measure of the effective thickness of the support layer, based on the porosity ε and tortuosity τ of the material [68].

$$S = \lambda \cdot \frac{D_F}{D_S} \tag{23}$$

$$S = \lambda \cdot \frac{\tau}{\varepsilon} \tag{24}$$

In the literature, a constant value is often assumed for the salt diffusion coefficient D [13, 15], however for improved accuracy it can be calculated from the empirical equation provided by [22]:

$$D = 6.725 \cdot 10^{-6} \cdot \exp\left(1.546 \cdot 10^{-4} \cdot c - \frac{2513}{T_K}\right) \tag{25}$$

Equations (1), (2) and (19) form a complete solution for the osmotic pressure difference $\Delta\Gamma_m$, the water permeate flux J_w, and the effective concentration difference Δc_m which can be solved numerically. A MATLAB-based computer program is developed and described in Figure 7. The system of equations is solved by providing an initial guess and then updating iteratively.

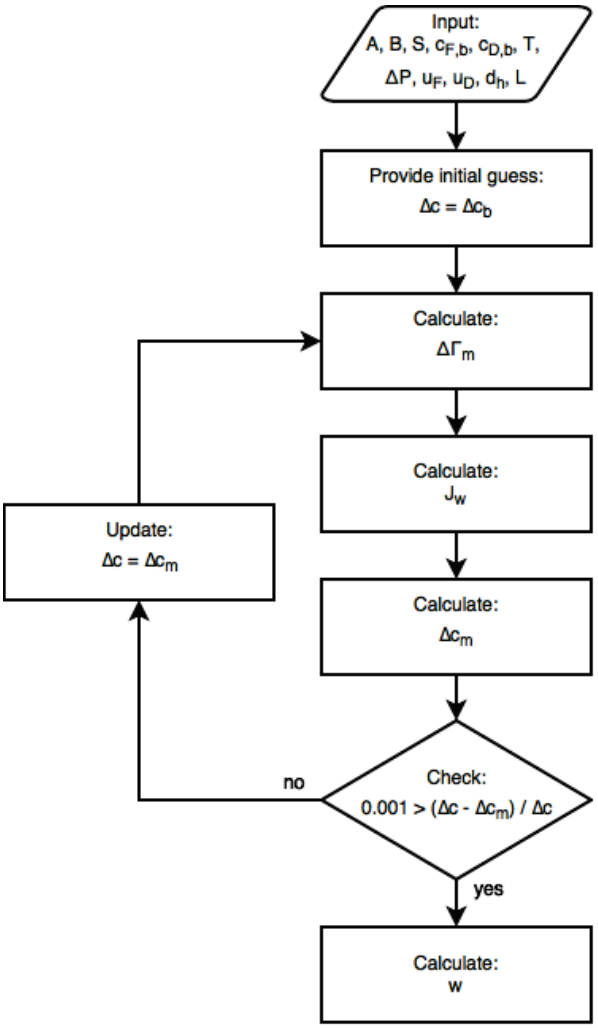

Figure 7. Model for solving polarization equation and determining power density

2.5.2. Concentration Polarization in Small Scale Membrane Samples

Efficiency in the PRO process depends on achieving high water permeate while minimizing reverse salt leakage and the tendency of salt to accumulate in the boundary layers and support layer of the membrane. Previously, when RO membranes have been used for PRO applications low power densities have been reported. This is because RO membranes have thick and dense support layers that are needed in order to withstand the

large hydraulic pressures used during RO processes. This thick support layer hinders osmosis because it provides an area for the accumulation of salt. Consider for example membrane 2 shown in Table 1, which is a commercial RO cellulose-acetate (CA) membrane. The high structure parameter S leads to low peak power densities of only 1.6 W/m^2 as reported in experimental tests with freshwater and seawater [42].

Table 1. Membrane parameters

	Description	Water permeability A ($\times 10^{-12}$ $m^3/m^2 \cdot s \cdot Pa$)	Salt permeability B ($\times 10^{-7}$ $m^3/m^2 \cdot s$)	Structure parameter S ($\times 10^{-6}$ m)	Source
1	Commercial FO-CTA	1.87	1.11	678	[36]
2	Commercial RO-CA	2.00	0.60	1000	[42]
3	Lab FO-TFC	7.10	1.10	670	[42]
4	Lab PRO-TFC	16.14	2.44	349	[38]

During PRO and FO processes, membranes are subjected to much lower hydraulic pressures than during RO processes. The thickness of the support layer can therefore be significantly reduced (and its negative effect on osmosis can be minimized). This has been done in the case of membrane 1 (Table 1) which is a cellulose-triacetate (CTA) membrane designed for commercial FO applications. Experimental results reported power densities of 2.7 W/m^2 using freshwater and seawater [36].

In addition to a minimal support structure, the ideal membrane for PRO applications should have high water permeability A and low salt permeability B. In reality, a trade-off between A and B must be optimized. This is necessary because as A increases, so does B. As the membrane becomes more permeable to water an increase in power is not always observed because of the accompanying increase in salt permeability. Membranes 3 and 4 (Table 1) were developed by carefully balancing these competing design objectives. Both are thin-film composite (TFC) experimental membranes and both show high water permeability. Lab tests using membrane 3 have reported power densities of 2.7 W/m^2 [42], and tests using membrane 4 have reported 10.0 W/m^2 [15]. These are encouraging results and represent a significant advance in the potential for PRO power development. In comparing these reported power densities it is important to note that different test conditions were used from one experiment to the next [40].

The effect of concentration polarization on a small scale sample of the membranes from Table 1 is simulated using the computer program described in Figure 7. The conditions for the simulation are listed in Table 2. A draw concentration of $c_{D,b}$ = 30 g/l is used since this is typical for seawater. Rivers typically have concentrations < 0.1 g/l and so for simplicity feed concentration of $c_{F,b}$ = 0 g/l is assumed here [70]. Solution temperature of T = 10 °C is used. This is more representative of ocean temperatures than what is often used in the literature (T ≈ 20 °C), and leads to more conservative power estimates. However, the B and S membrane parameters are functions of temperature and are defined under test conditions where usually T ≈ 20 °C [67]. This makes it difficult to evaluate PRO performance under different climatic conditions. For improved accuracy the B and

S parameters can be adjusted by referring to the definitions provided in [40]. In general, a decrease in T will lead to a decrease in both B and S. The effect of temperature on PRO performance is the subject of on-going research [67, 68]. A constant salt diffusion coefficient D is assumed [47]. Flow rates are set so as to obtain inlet flow velocities of u = 0.25 m/s [67].

Table 2. Conditions for simulation of PRO with small scale membrane samples

Membrane length L	mm	10
Feed channel hydraulic diameter $d_{h,F}$	mm	0.2
Draw channel hydraulic diameter $d_{h,D}$	mm	0.1
Feed concentration $c_{F,b}$	g/l	0
Draw concentration $c_{D,b}$	g/l	30
Feed cross-flow velocity u_F	m/s	0.25
Draw cross-flow velocity u_D	m/s	0.25
Salt diffusion coefficient D	m^2/s	$1.5 \cdot 10^{-9}$
Temperature T	°C	10

Figure 8 shows the simulation results, where effective concentration difference Δc_m, water permeate flux J_w and gross PRO power density w_{gross}^{PRO} are plotted as functions of hydraulic pressure difference ΔP. The solid line shows performance when both ICP and ECP are considered. The peak $\hat{w}_{gross}^{PRO}$ available from the membrane samples are 2.0, 2.1, 4.8 and 7.7 W/m^2 for membranes 1 to 4 respectively. These results suggest that

membrane 3 and 4 may have potential for commercial power applications based on the target of 5 W/m^2.

These are quite different from the results reported in the literature. This is because of the different conditions used for simulation and experiments. When the test conditions are replicated the results obtained from the simulation corresponds to the published data. For example in the case of membrane 1, using simulation conditions T = 24 °C, u = 0.133 m/s, Δc_b = 35 g/l, L = 75 mm, and d_h = 0.95 mm gives peak $\widehat{w}_{gross}^{PRO}$ = 2.7 W/m^2, just as reported in [36].

Maximum PRO power density occurs when hydraulic pressure difference $\Delta P = \Delta\Gamma_m / 2$, however it may be preferable to use a lower ΔP given the power curve's diminishing rate of return. For example, in the case of membrane 4 a 5% increase in w_{gross}^{PRO} (from 7.3 to 7.7 W/m^2) requires a 30% increase in ΔP (from to 8.8 to 11.4 bar). Identifying the best ΔP will depend on the net balance between increased pumping loads and increased power output at the generator.

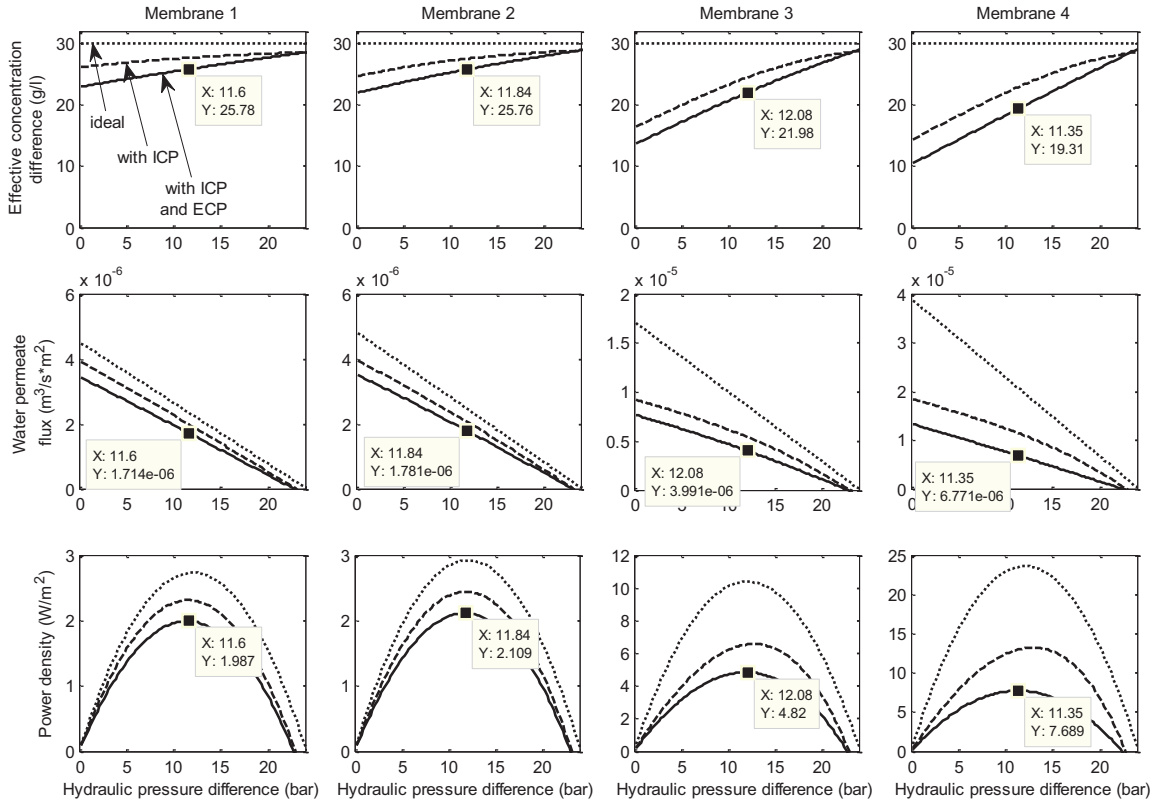

Figure 8. Effective concentration difference Δc_m, water permeate flux J_w, and gross PRO power density w_{gross}^{PRO} as functions of hydraulic pressure difference ΔP for small scale samples of membranes 1-4

Equation (19) shows that concentration polarization can be minimized by reducing the structure parameter S, by reducing the salt permeability B, and by reducing the feed side and draw boundary layers δ_F and δ_D respectively. It is interesting to consider the potential improvements in PRO power that can be achieved by these approaches.

Analyzing equation (22) and expanding the expression for Reynolds number reveals that film thickness is inversely proportional to flow velocity to the power of κ_1. During operation, high feed and draw flow rates can be supplied over the membrane surface in

order to achieve high flow velocity, and thereby minimize external concentration polarization. This option is simulated here by letting $u \rightarrow \infty$, in which case ECP becomes negligible and only ICP affects the performance. The results are shown by the large hatched line in Figure 8.

The option of reducing structure parameter S is simulated here by letting $S \rightarrow 0$. The short hatched line in Figure 8 shows this ideal case where both ICP and ECP are eliminated. Although physically impossible, these conditions allow for the effects of ICP and ECP to be isolated and compared.

Figure 8 confirms that the effect of ICP is more important than ECP, accounting for a 15%, 17%, 37% and 44% decrease in power density relative to ideal in membranes 1-4 respectively. On the other hand, ECP accounts for a 12%, 11%, 17% and 23% drop in power density relative to ideal. Results indicate that the portion of losses attributed to ECP could potentially be eliminated by controlling flow velocities over the membrane.

Another scenario is also simulated to show the effect of minimizing structure parameter in each of the membranes. The structure parameter does not have a direct relation with A and B and therefore S = 349 μm can theoretically be used for each of the membranes listed in Table 1. Figure 9 shows gross PRO power density w_{gross}^{PRO} as a function of hydraulic pressure difference ΔP for membranes 1-4 when their structure parameter is reduced to S = 349 μm. Despite the improvement, membranes 1 and 2 still yield less than 2.5 W/m^2. However in the case of membrane 3 the approach is effective, leading to peak $\hat{w}_{gross}^{PRO}$ = 5.9 W/m^2.

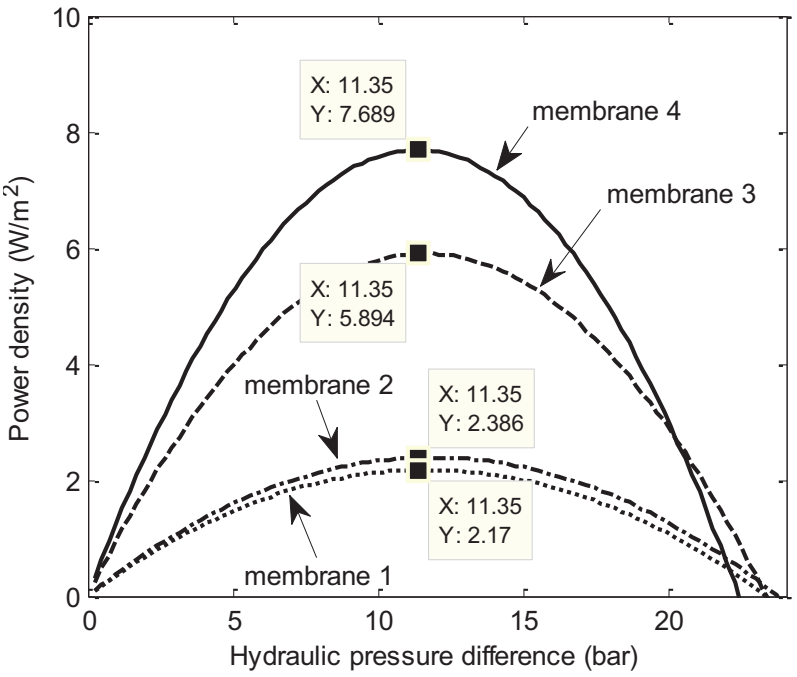

Figure 9. Gross PRO power density w_{gross}^{PRO} as a function of hydraulic pressure difference ΔP for small scale samples of membranes 1-4 when structure parameter is reduced to S = 349 μm

2.6. Variations along the Length of the Membrane

2.6.1. Modeling Variations along the Length of the Membrane

Variations along the length of the membrane (x axis) are caused by water and salt permeate [45, 47]. Water permeate flux J_w causes feed flow rate $\dot{V}_F$ to decrease and draw flow rate $\dot{V}_D$ to increase along the length of the membrane (as functions of x). Also, water permeate flux J_w and reverse salt flux J_s combine to cause bulk feed concentration $c_{F,b}$ to increase and bulk draw concentration $c_{D,b}$ to decrease along the length of the membrane (again as functions of x). Spatial variations between the membrane inlet at x = 0 and the

membrane outlet at x = L are illustrated in Figure 10, where L is the length of the membrane.

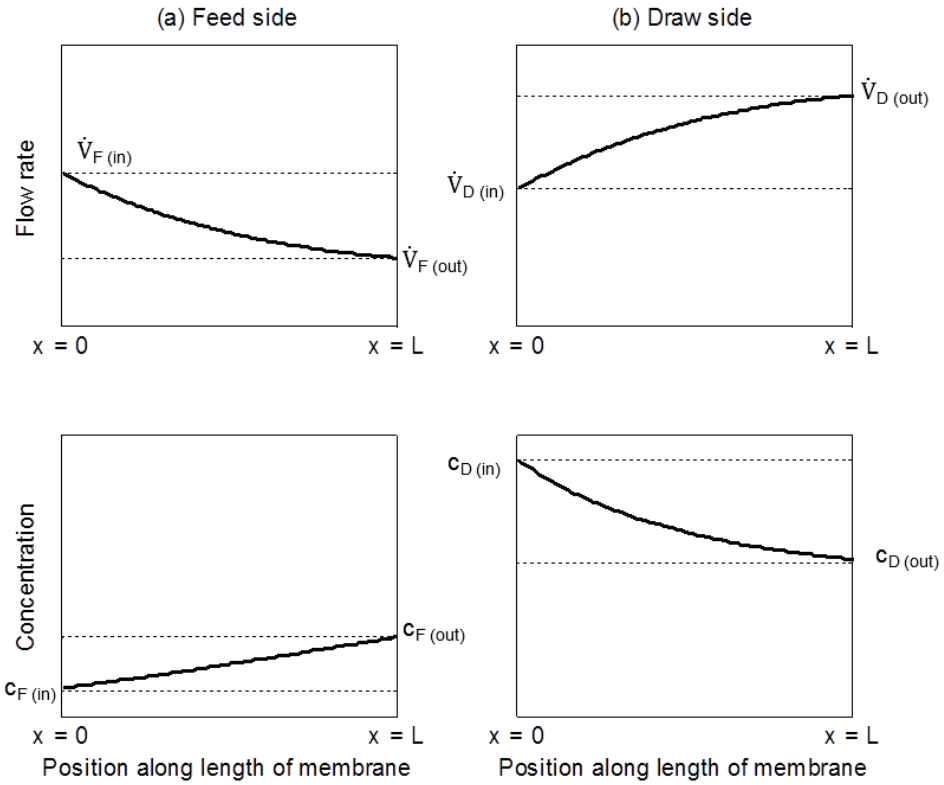

Figure 10. Variation in flow rate and concentration on the (a) feed side and (b) draw side of the membrane

The primary effect of these variations is a reduction in power density, resulting from the drop in concentration difference, $\Delta c\ (x = L) < \Delta c\ (x = 0)$. A secondary effect is a change in the thickness of the polarization boundary layers. As draw flow increases so does mixing, and the boundary layer δ_D is reduced. On the other hand, the feed side boundary layer δ_F increases because of the drop in feed flow. As a result feed side polarization

becomes more significant and draw side polarization becomes less significant as flow advances along the membrane length.

These variations and their effects are often neglected in the literature, on the assumption that permeate volumes are insignificant relative to much larger feed and draw volumes [35, 36, 37, 38]. This is sometimes the case at the bench scale, where small membrane samples yield only small volumes of permeate. But this is far from the case at the commercial scale, where a significant portion of the feed solution permeates across the membrane, for example 80% [42]. Very few mathematical models have included this effect [45, 47] and as a result membrane power potentials are often over-evaluated.

Flow rates and concentrations along the length of the membrane can be evaluated by taking the membrane surface integral $\iint \mathrm{dS}$ of the water and salt fluxes as shown:

$$\dot{V}_F(x) = \dot{V}_F(x = 0) - \iint J_w(x) \cdot dS \tag{26}$$

$$\dot{V}_D(x) = \dot{V}_D(x = 0) + \iint J_w(x) \cdot dS \tag{27}$$

$$c_{F,b}(x) = \frac{c_{F,b}(x = 0) \cdot \dot{V}_F(x = 0)}{\dot{V}_F(x)} + \iint \frac{J_s(x)}{\dot{V}_F(x)} \cdot dS \tag{28}$$

$$c_{D,b}(z) = \frac{c_{D,b}(x = 0) \cdot \dot{V}_D(x = 0)}{\dot{V}_D(x)} - \iint \frac{J_s(x)}{\dot{V}_D(x)} \cdot dS \tag{29}$$

Using volumetric flow rates assumes that densities remain constant along the membrane length [72].

Equations (26)-(29) show that variations in flow rate and concentration can be minimized by increasing flow rates. For example, as $\dot{V}(x = 0) \rightarrow \infty$, $\dot{V}(x) \rightarrow \dot{V}(x = 0)$, and $c(x) \rightarrow c(x = 0)$.

Variations along the length of the membrane (x axis) are also caused by the drop in hydraulic pressure P_{drop} that occurs on each side of the membrane due to friction [58]. These pressure losses are generally ignored during PRO modeling in the literature. Some recent publications have mentioned their importance in commercial scale modeling but not included them [13, 17]. This is among the first models to consider spatial variations caused by pressure drop during PRO. Pressure drop can be described by [60, 73]:

$$P_{drop}(x) = \int \frac{\rho \cdot f(x) \cdot u(x)^2}{2 \cdot d_h} \cdot dx \tag{30}$$

ρ is density, and f is the friction factor.

The general form of the dimensionless friction factor is [60, 73]:

$$f = \varphi_1 \cdot Re^{\varphi_2} \tag{31}$$

φ_1 and φ_2 are constants.

Pressure drops on the feed side $P_{F,drop}$ and on the draw side $P_{D,drop}$ are usually uneven. This leads to spatial variation in the hydraulic pressure difference across the membrane, i.e. $\Delta P(x = 0) \neq \Delta P(x = L)$. Hydraulic pressure difference as a function of position can be evaluated from:

$$\Delta P(x) = \Delta P(x = 0) - \left(P_{D,drop}(x) - P_{F,drop}(x)\right) \tag{32}$$

Equations (30) and (31) show that pressure drop is proportional to flow velocity to the power of $(2 + \varphi_2)$. In other words, as flow rates increase so will parasitic pressure losses. This is therefore in competition with and sets a limit to the previously identified approach of reducing concentration polarization and spatial variations via increased flow rates.

When spatial variations are considered, the fundamental flux equations (2) and (3) and the gross PRO power density equation (4) can be rewritten as functions of position x along the length of the membrane:

$$J_w(x) = A \cdot (\Delta\Gamma_m(x) - \Delta P(x)) \tag{33}$$

$$J_s(x) = B \cdot \Delta c_m(x) \tag{34}$$

$$w_{gross}^{PRO}(x) = J_w(x) \cdot \Delta P(x) \tag{35}$$

When comparing membrane performance, it is useful to consider the average water permeate flux $\overline{J_w}$ and average gross PRO power density $\overline{w}_{gross}^{PRO}$ that are obtained over the whole length of the membrane:

$$\overline{J_w} = \frac{1}{L} \cdot \int_0^L A \cdot (\Delta\Gamma_m(x) - \Delta P(x)) \cdot dx \tag{36}$$

$$\overline{w}_{gross}^{PRO} = \frac{1}{L} \cdot \int_0^L J_w(x) \cdot \Delta P(x) \cdot dx \tag{37}$$

The total water permeate flow rate $\dot{V}_P$ available at the membrane outlet is therefore the surface integral of J_w over the whole membrane area:

$$\dot{V}_P = \iint J_w \cdot dS \tag{38}$$

Spatial variations can be modeled by either taking an average of inlet and outlet variables, or by finite element analysis of the membrane length [45, 47]. The latter approach is more accurate and is the one employed here. The finite difference model is illustrated in Figure 11, where a simple mass balance of water and salt is accounted for at each finite section of membrane length. The membrane is divided in to n number of pieces each with surface area a_m / n, where a_m is the total membrane surface area. Water and salt flow rates at membrane piece i + 1 are calculated based on water and salt permeate at membrane piece i. Flow rates and concentrations can then be calculated from the updated mass flow rates.

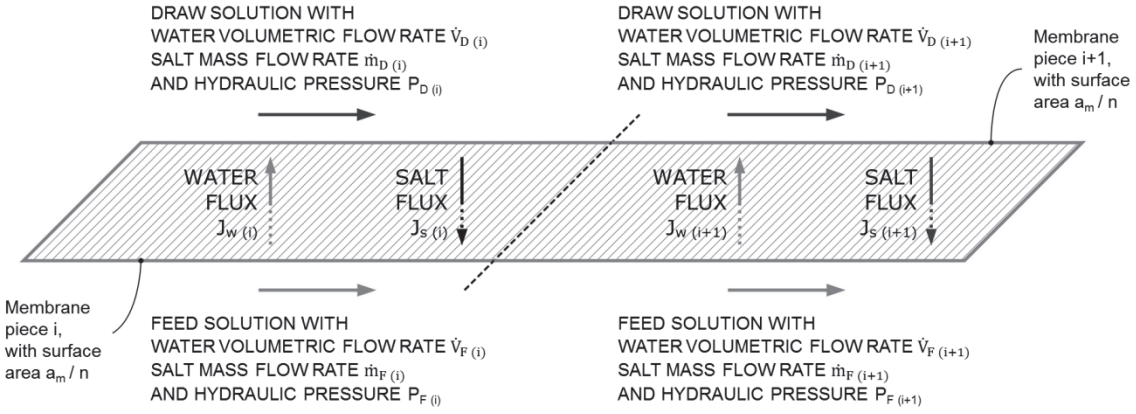

Figure 11. Variation in flow rates, concentrations and hydraulic pressures along the length of the membrane

The finite difference equations for flow rates, concentrations and hydraulic pressure are provided in equations (39)–(44).

$$\dot{V}_{F_{(i+1)}} = \dot{V}_{F_{(i)}} - J_{w\,(i)} \cdot \frac{a_m}{n} \tag{39}$$

$$\dot{V}_{D_{(i+1)}} = \dot{V}_{D_{(i)}} + J_{w\,(i)} \cdot \frac{a_m}{n} \tag{40}$$

$$c_{F,b_{(i+1)}} = \frac{c_{F,b_{(i)}} \cdot \dot{V}_{F_{(i)}} + J_{s_{(i)}} \cdot a_m/n}{\dot{V}_{F_{(i+!)}}} \tag{41}$$

$$c_{D,b_{(i+1)}} = \frac{c_{D,b_{(i)}} \cdot \dot{V}_{D_{(i)}} - J_{s_{(i)}} \cdot a_m/n}{\dot{V}_{D_{(i+1)}}} \tag{42}$$

$$P_{drop_{(i)}} = \frac{\rho \cdot f_{(i)} \cdot u_{(i)}{}^2}{2 \cdot d_h} \cdot \frac{L}{n} \tag{43}$$

$$\Delta P_{(i+1)} = \Delta P_{(i)} - \left(P_{D,drop_{(i)}} - P_{F,drop_{(i)}}\right) \tag{44}$$

A MATLAB-based computer program was developed using these equations, and is shown in the flow chart in Figure 12. The program contains two feedback loops. The first is used to solve the concentration polarization system of equations, as previously explained. The second is the finite difference cycle used to consider variation along the length of the membrane, where output from membrane piece i is used as input for membrane piece i + 1.

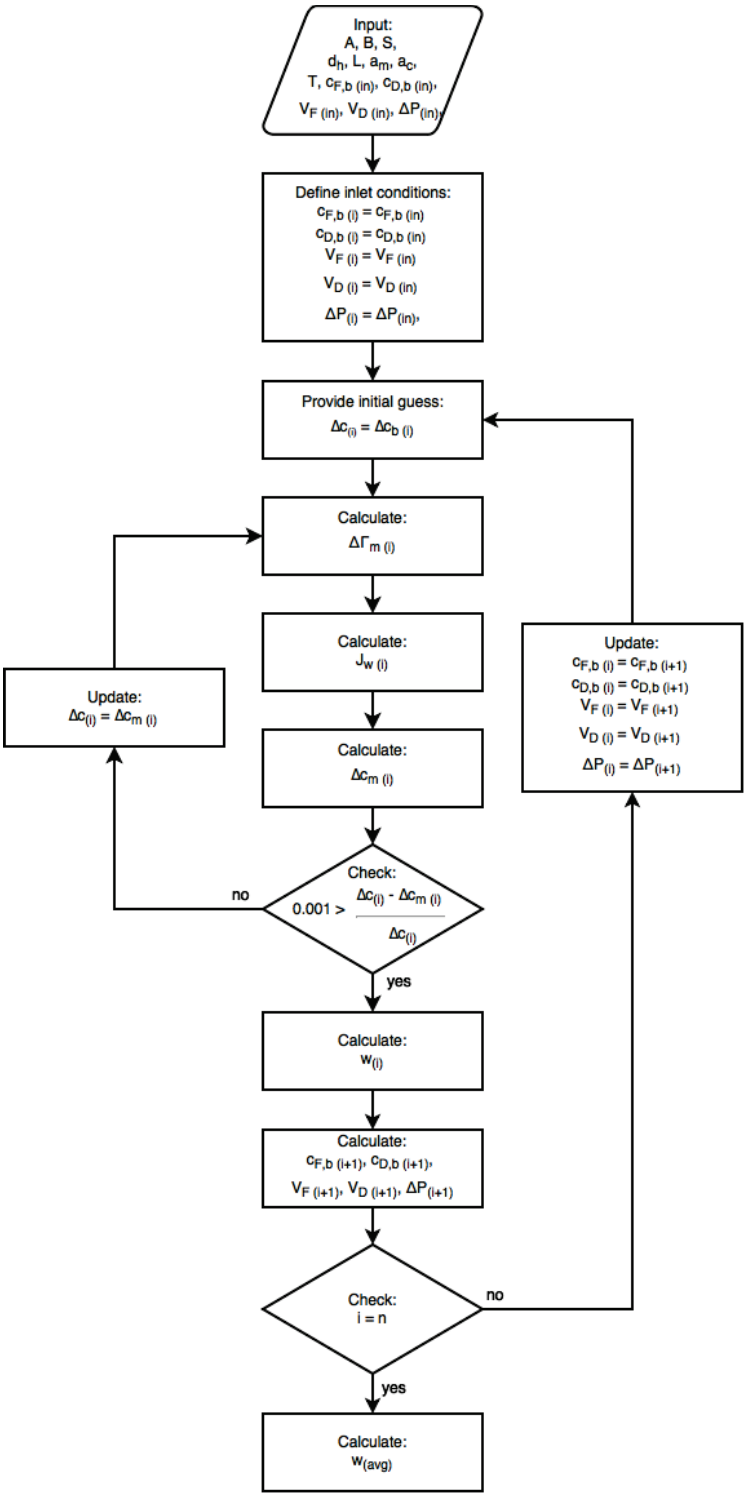

Figure 12. Model for solving polarization equation and considering spatial variations along the length of membrane

2.6.2. Variations in Commercial Length Membranes

The simulation results for small scale samples of membranes 3 and 4 (from Table 1) showed gross PRO power densities of $\hat{w}_{gross}^{PRO} > 5$ W/m^2 (when their structure parameters were adjusted to S = 349 μm). These results suggest the potential for commercial feasibility but neglect the influence of spatial variations that will be significant at the commercial scale. Their performance at the commercial scale is here evaluated by simulation, using the mathematical model described in Figure 12. Membranes 1 and 2 are not considered since they failed to generate acceptable power densities at even small scales.

A single hollow fiber membrane configuration was considered, as shown in Figure 13. Feed solution flows through the inside of the hollow fiber while draw solution flows on the outside of the fiber. A hollow fiber with length L = 1 m was considered during simulation. The other simulation conditions are described in Table 3. In the case of membrane 3, the adjusted structure parameter S = 349 μm was used.

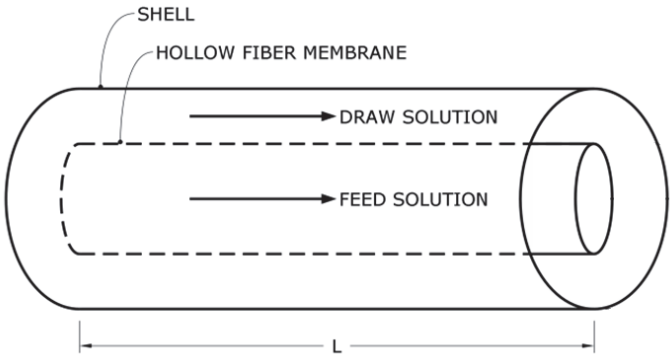

Figure 13. Single hollow fiber membrane module

Table 3. Conditions for simulation of PRO with commercial length membranes

Membrane length L	m	1
Radius of hollow fiber	mm	0.1
Radius of module casing	mm	0.15
Feed concentration $c_{F,b}$ (x = 0)	g/l	0
Draw concentration $c_{D,b}$ (x = 0)	g/l	30
Feed cross-flow velocity u_F (x = 0)	m/s	0.25
Draw cross-flow velocity u_D (x = 0)	m/s	0.25
Salt diffusion coefficient D	m^2/s	$1.5 \cdot 10^{-9}$
Temperature T	°C	10

Figure 14 shows the spatial variation in bulk concentrations c_b and in cross-flow velocity u which occurs in the axial direction of commercial length membranes 3 and 4. As expected water and salt permeate lead to ↑ $c_{F,b}$, ↓ $c_{D,b}$, ↓ u_F and ↑ u_D. This ultimately leads to a drop in the effective concentration difference Δc_m, and to diminishing water permeate flux J_w and gross PRO power density w_{gross}^{PRO}.

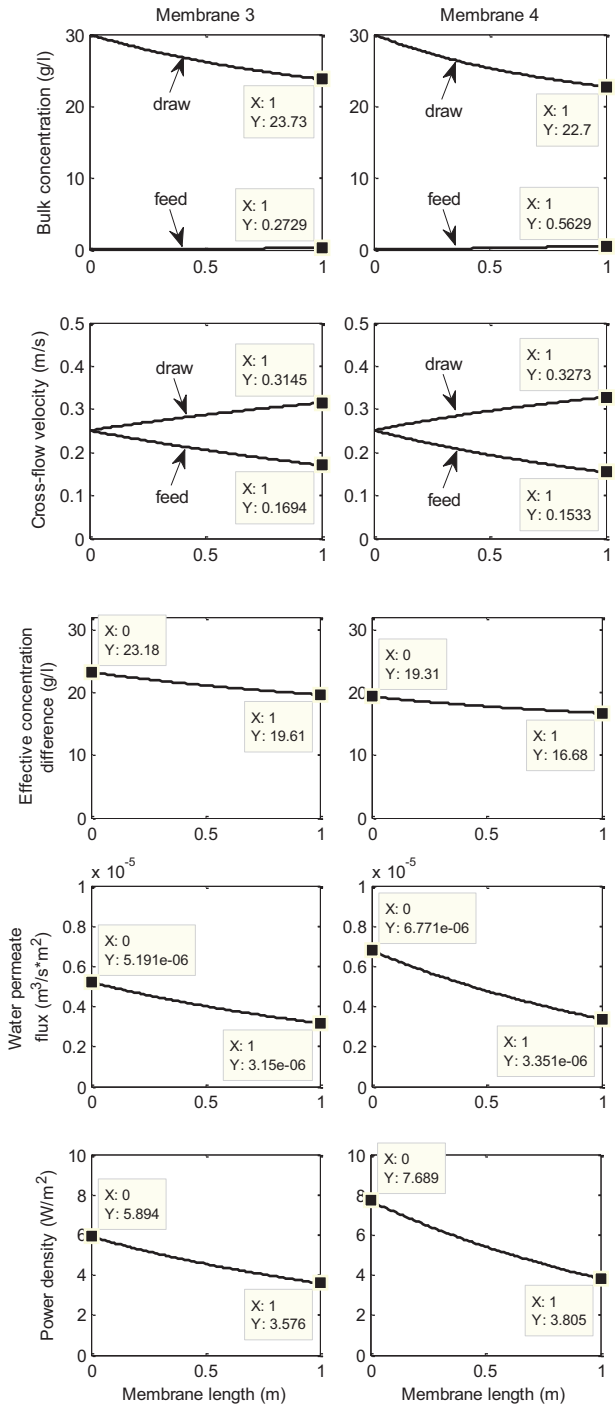

Figure 14. Spatial variation of bulk concentration c_b, cross-flow velocity u, effective concentration difference Δc_m, water permeate flux J_w and gross PRO power density w_{gross}^{PRO} along the length of commercial scale membranes 3 (with S = 349 μm) and 4, when hydraulic pressure difference $\overline{\Delta P}$ = 11.35 bar

For membrane 3 a 39% decrease in w_{gross}^{PRO} is observed (from 5.9 to 3.6 W/m^2), while for membrane 4 a 51% decrease is observed (from 7.7 to 3.8 W/m^2). These results are important because they illustrate that spatial variations are more significant in high flux membranes, such as membrane 4. Spatial variations therefore have the tendency to equalize the performances of various membranes. To further illustrate, consider the average gross PRO power density $\overline{w}_{gross}^{PRO}$ obtained along the length of the membranes, which are 4.6 W/m^2 for membrane 3 and 5.6 W/m^2 for membrane 4. These are much closer to one another than anticipated from the earlier simulation of small scale samples, which showed $\widehat{w}_{gross}^{PRO}$ = 5.9 W/m^2 and 7.7 W/m^2 for membranes 3 and 4 respectively. Again, this is because spatial variations are more pronounced in high flux membranes, leading to a proportionately greater performance drop than in low flux membranes. In order for improved membrane performance to carry over from the bench scale to the commercial scale, future consideration should therefore be given to adjusting membrane geometry and adjusting the feed and draw flow rates.

Polarization across the feed side boundary layer is usually minor compared to polarization across the support layer and across the draw side boundary layer. However, the $\downarrow u_F$ and $\uparrow c_{F,b}$ shown in Figure 14, indicates that feed side ECP will become progressively more important along the length of a commercial scale membrane. Polarization across the feed side boundary layer is usually neglected in the literature, however these results suggest that it may be important to consider, especially for

modeling commercial scale membranes. As mentioned previously, this is among the first models to consider polarization across the feed side boundary layer.

The results shown in Figure 14 are for the case where $\overline{\Delta P}$ = 11.35 bar, because this was previously identified in Figure 9 as the peak power point for a small scale membrane sample. Spatial variations however can lead to a new peak power point. Figure 15 shows gross PRO power density w_{gross}^{PRO} as a function of average hydraulic pressure difference $\overline{\Delta P}$ for both the inlet and outlet of commercial length membranes 3 and 4. As shown, the best $\overline{\Delta P}$ is not the same at the inlet and outlet. For example, in the case of membrane 4 the best $\overline{\Delta P}$ will be somewhere between 11.4 bar (peak power at the inlet) and 10.6 bar (peak power at the outlet).

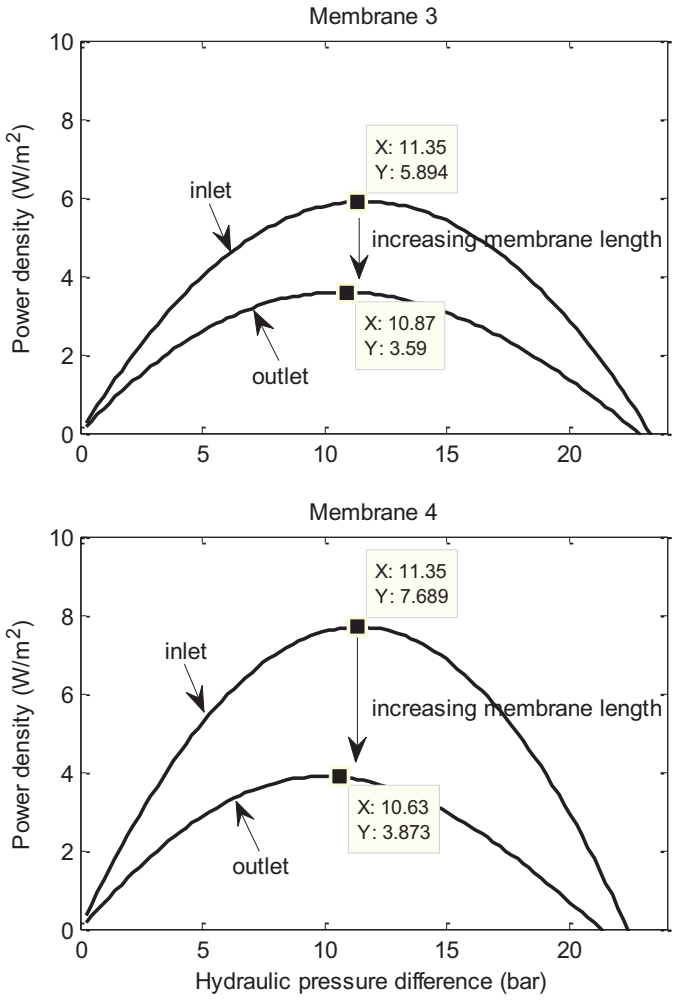

Figure 15. Power density w_{gross}^{PRO} as a function of hydraulic pressure difference $\overline{\Delta P}$ at the inlet and outlet of commercial length hollow fiber membrane 3 (with structure parameter adjusted to S = 349 μm) and membrane 4

2.7. Osmotic Power Plants

2.7.1. Efficiency of PRO Energy Conversion Process

Losses during PRO are illustrated in Figure 16. Concentration polarization and spatial variations modify water permeate flux J_w and hydraulic pressure difference ΔP such that

gross PRO power density w_{gross}^{PRO} will be less than the maximum PRO power density w_{max}. The power consumed by the parasitic pressure losses is then the difference between the gross PRO power density w_{gross}^{PRO} and the net PRO power density w_{net}^{PRO}. Balancing the competing requirements for reducing concentration polarization, spatial variations and pressure losses, is ultimately a matter of maximizing the net power density of the PRO process. The efficiency of the PRO process η_{PRO} can be obtained from:

$$\eta_{PRO} = \frac{W_{net}^{PRO}}{W_{max}} \cdot 100 \tag{45}$$

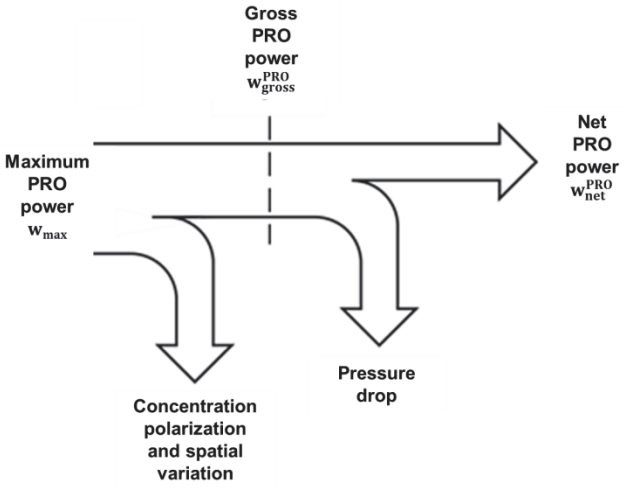

Figure 16. Power flow during PRO process

Net PRO power W_{net}^{PRO} can be evaluated by considering the difference between power available at the membrane outlet and inlet.

$$W_{net}^{PRO} = W_{out} - W_{in} \tag{46}$$

$$W_{net}^{PRO} = \left[\dot{V}_D(x = L) \cdot P_D(x = L) + \dot{V}_F(x = L) \cdot P_F(x = L)\right] - \left[\dot{V}_D(x = 0) \cdot P_D(x = 0) - \dot{V}_F(x = 0) \cdot P_F(x = 0)\right] \quad (47)$$

Net PRO power density can then be obtained by normalizing over the membrane area:

$$w_{net}^{PRO} = \frac{W_{net}^{PRO}}{a_m} \quad (48)$$

2.7.2. Efficiency of Osmotic Power Plant

Ultimately, the objective of PRO for power applications is to produce net electric power. This depends not only on the efficiency of the PRO process, but also on the efficiency of the whole osmotic power plant. The basic configuration of the osmotic power plant is provided in Figure 17. Feed solution is supplied by an electric pump and is filtered before being introduced to one side of the semi-permeable membrane unit. Similarly, draw solution is supplied by an electric pump and is filtered. Before being introduced to the membrane unit, it is pressurized through a pressure exchanger and electric boost pump. This establishes the desired hydraulic pressure difference across the membrane. At the membrane outlet, draw solution is recirculated through the pressure exchanger while permeate flow is depressurized across a turbine and generator.

This pressure exchanger and boost pump combination is currently among the best options for maintaining a pressurized draw solution. Pressure exchangers can reach 97% efficiencies making them more efficient than to any combination involving pumps,

motors, turbines or generators [71]. The boost pump makes up for the minor losses in the pressure exchanger.

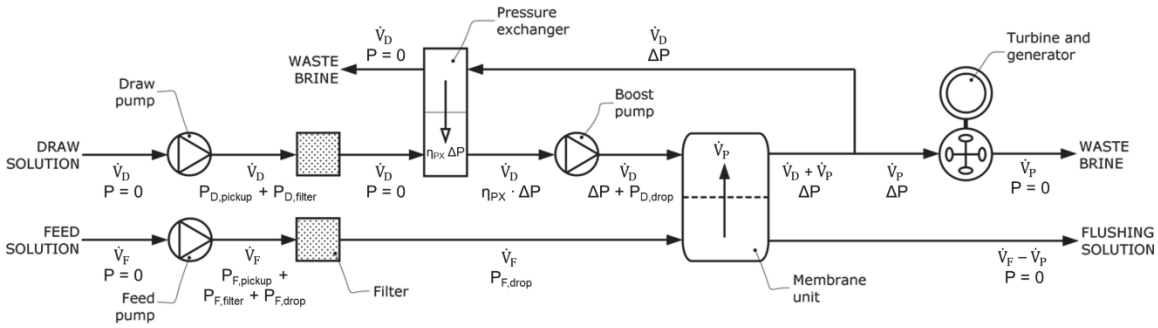

Figure 17. Schematic for an osmotic power plant showing flow rates and hydraulic pressures throughout the system

Gross power developed by the PRO process W_{gross}^{PRO} is the product of permeate flow rate $\dot{V}_P$ and its hydraulic pressure above ambient, which is equal to the draw side hydraulic pressure at the membrane outlet. This is the power available at the inlet to the hydro-turbine shown in Figure 17.

$$W_{gross}^{PRO} = \dot{V}_P \cdot \Delta P \tag{49}$$

This hydraulic power is converted to electric power by a turbine and generator. The gross electric power output W_{gross}^{e} is a function of the turbine and generator efficiencies $\eta_{turbine}$ and $\eta_{generator}$.

$$W_{gross}^{e} = W_{gross}^{PRO} \cdot \eta_{turbine} \cdot \eta_{generator} \tag{50}$$

The net electric power W^e_{net} available for the grid is then be gross electric power minus the power consumed by each of the electric pumps W^e_{pump}.

$$W^e_{net} = W^e_{gross} - \sum W^e_{pump} \tag{51}$$

Parasitic loads supplied by the pumps include the pressure drops along the length of the membrane, as well as pre-treatment filtration P_{filter}, pick-up head P_{pickup}, and losses in the electrical and mechanical equipment. Figure 17 shows how each of these loads might be distributed among the pumps.

The feed pump supplies the losses on the feed side of the membrane unit, the filtration losses, and the pick-up head. The electric power consumed by the feed pump $W^e_{F,pump}$ is therefore:

$$W^e_{F,pump} = \frac{\left(P_{F,drop} + P_{F,filter} + P_{F,pickup}\right) \cdot \dot{V}_F}{\eta_{pump} \cdot \eta_{motor}} \tag{52}$$

$\eta_{pump} \cdot \eta_{motor}$ is the combined pump and motor efficiency.

The draw pump supplies the draw side filtration losses and pick-up head. The electric power consumed by the draw pump $W^e_{D,pump}$ is:

$$W^e_{D,pump} = \frac{\left(P_{D,pickup} + P_{D,filter}\right) \cdot \dot{V}_D}{\eta_{pump} \cdot \eta_{motor}} \tag{53}$$

The boost pump is used to supply losses on the draw side of the membrane unit and in the pressure exchanger. The electric power that it consumes $W^e_{B,pump}$ is:

$$W^{e}_{B,pump} = \frac{\left(P_{D,drop} + \Delta P \cdot \left(1 - \eta_{px}\right)\right) \cdot \dot{V}_{D}}{\eta_{pump} \cdot \eta_{motor}} \tag{54}$$

η_{px} is the pressure exchanger efficiency.

The power flow in an osmotic power plant is summarized in Figure 18. The ratio of the net electric power output of the system to the maximum PRO power potential gives an evaluation of the overall efficiency of the osmotic power plant.

$$\eta_{plant} = \frac{W^{e}_{net}}{w_{max} \cdot a_{m}} \cdot 100 \tag{55}$$

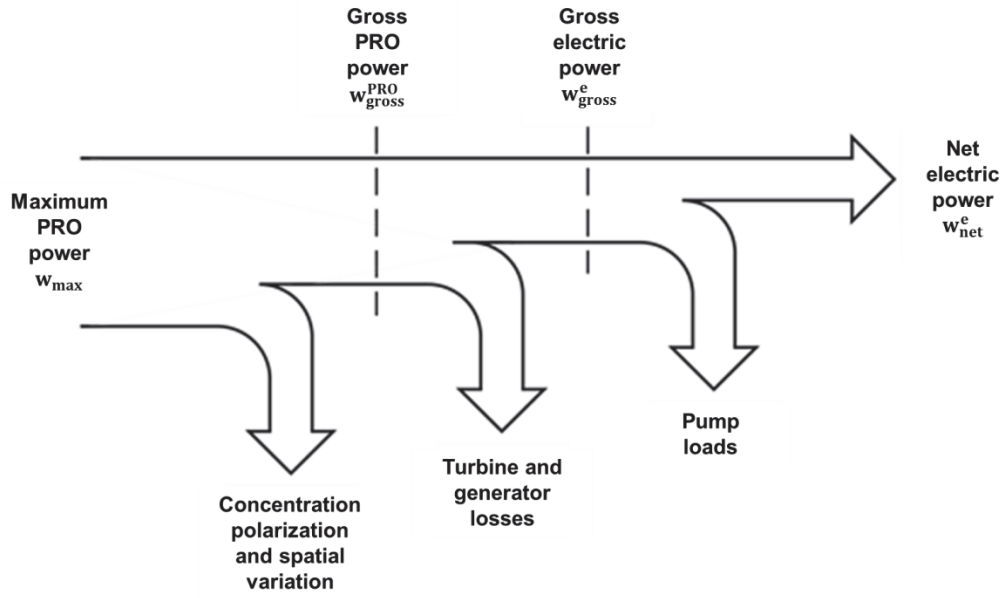

Figure 18. Power flow in osmotic power plant

A mathematical model has been developed for evaluating net electric power output of an osmotic power plant. The model is summarized by the flow chart in Figure 19 and has been developed in MATLAB. The program builds upon the previously described models,

with two feedback loops - one for solving the polarization system of equations, and a second for considering variations along the length of the membrane. The net performance of the plant can be evaluated when given membrane characteristics, site data, operating conditions and equipment specifications.

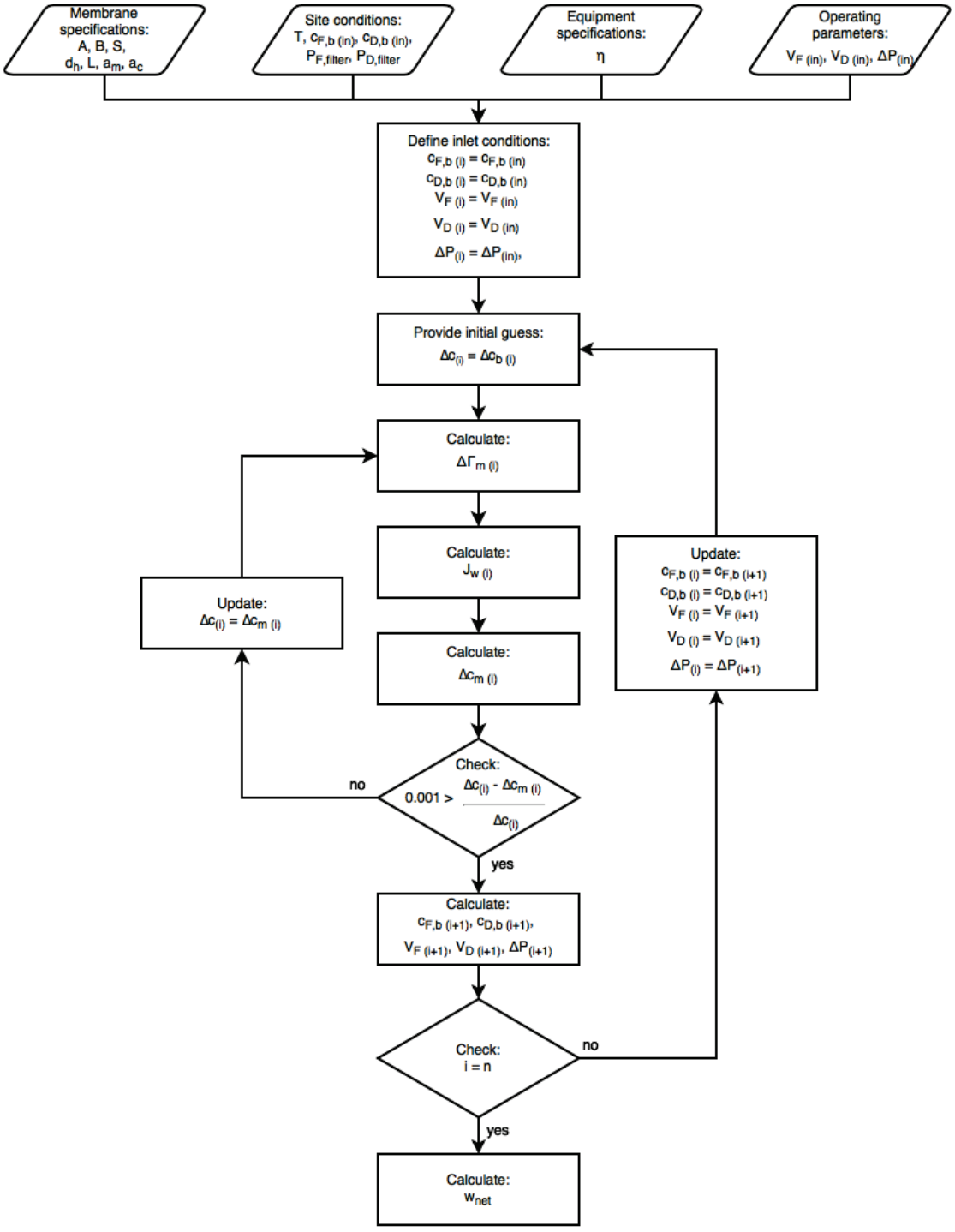

Figure 19. Model for osmotic power plant

2.7.3. Validation of the Mathematical Model

In order to validate the model, simulation results were compared against experimental data available in the literature. The results published by [36] are particularly valuable because they present experimental results for permeate flux, as well as a detailed description of the experimental setup and test conditions used. The experimental set-up is summarized in Table 4.

Table 4. Conditions for experimental tests conducted by [36]

Properties of membrane sample		
Water permeability A	$m^3/Pa \cdot s \cdot m^2$	$1.87 \cdot 10^{-12}$
Salt permeability B	$m^3/s \cdot m^2$	$1.11 \cdot 10^{-7}$
Structure parameter S	m	$6.78 \cdot 10^{-4}$
Geometry of membrane sample		
Surface area a_m	cm^2	18.75
Length L	mm	75
Width	mm	25
Channel height	mm	2.5
Hydraulic diameter d_h	mm	0.946
Operating conditions		
Temperature T	°C	24
Feed velocity u_F	m/s	0.133
Draw velocity u_D	m/s	0.133

A rectangular flat-sheet CTA membrane sample was tested by [36]. Six scenarios were considered during which $c_{F,b}$ was equal to 0, 2.5 and 5.0 g/l and $c_{D,b}$ was equal to 30 and 60 g/l. Water permeate flux $\overline{J_w}$ was measured at hydraulic pressure differences $\overline{\Delta P}$ of 0, 3.1, 6.5 and 9.7 bar, and gross PRO power density $\overline{w}_{gross}^{PRO}$ was calculated. The measured data points are marked on Figure 20 along with the simulated curves generated from the proposed mathematical model.

A good correlation between the experimental data points and the simulated curves is observed. This confirms that the proposed mathematical model accurately describes bench scale PRO dynamics. The simulated curves closely resemble those that were generated by [36], including a similar error between the simulated and experimental results of case (f). The advantage of the model proposed here is that by considering spatial variations and system losses, this model can be applied to much larger systems. There are however no experimental results available in the literature for commercial scale PRO systems and therefore validation of certain dynamics remains limited.

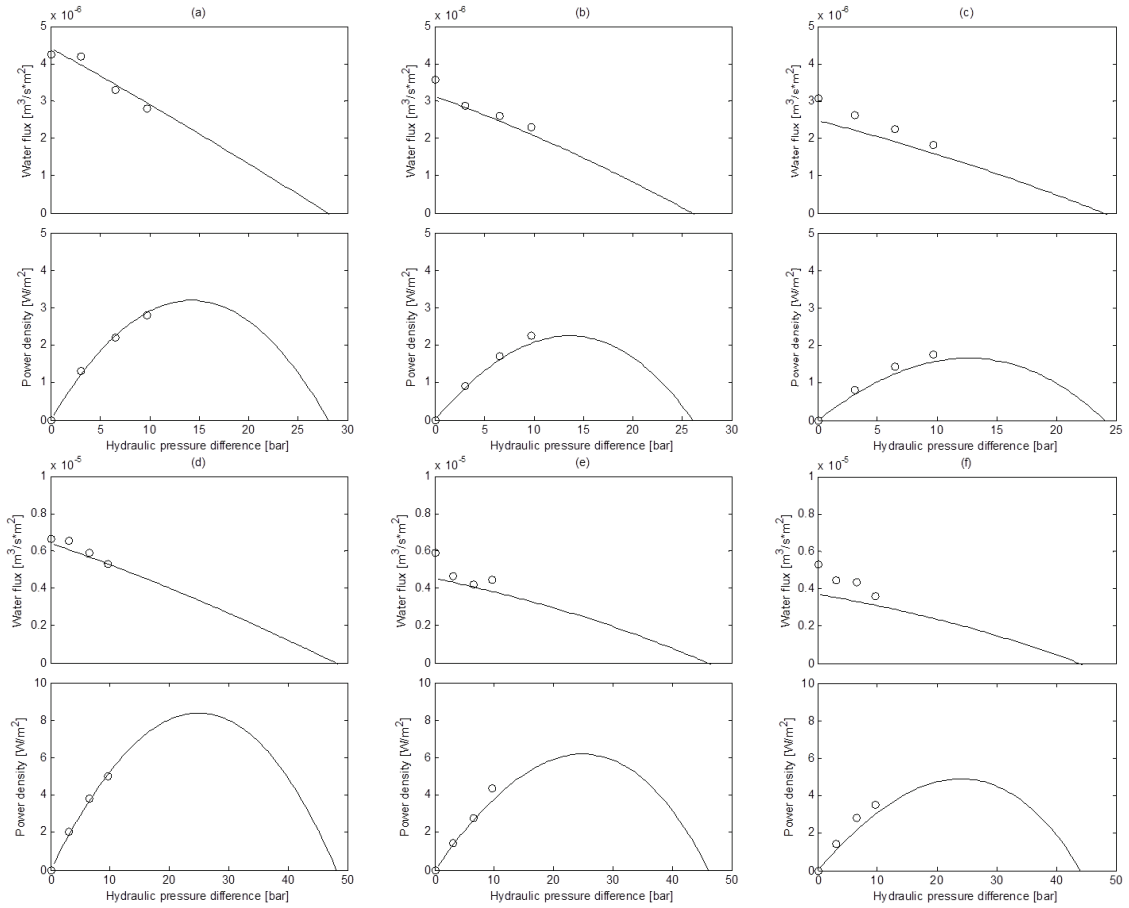

Figure 20. Simulated water permeate flux $\overline{J_w}$ and gross PRO power density $\overline{w}_{gross}^{PRO}$ as compared to experimental results published by [36] using the following feed and draw concentrations (g/l): (a) 0 and 35, (b) 2.5 and 35, (c) 5 and 35, (d) 0 and 60, (e) 2.5 and 60, (f) 5 and 60

2.7.4. Simulating Performance of an Osmotic Power Plant

Consider the performance of a commercial scale PRO power plant using the same membrane material tested by [36] (same A, B and S parameters) assembled into a hollow fiber configuration. Although this material is currently available on the market in only spiral configurations, the hollow fiber configuration is promising for PRO applications. Hollow fiber membranes are self-supporting and therefore do not need spacers, which

reduce performance in spiral elements. Also, higher packing densities can be achieved in hollow fiber elements, facilitating industrial scale-up. Recently developed hollow fiber membranes have shown excellent performance under laboratory conditions [43, 44]. Commercial scale hollow fiber membrane elements can be modelled by considering flow through a single hollow fiber channel and then scaling results linearly based on the number of fibers within the element [76]. Results can also be scaled linearly based the number of membrane elements that are placed in parallel within the system.

The dimensions of the proposed hollow fiber membrane element are summarized in Table 5, along with other simulation parameters.

The hydraulic diameter $d_{h,D}$ and cross sectional area $a_{c,D}$ of flow on the draw side of a single hollow fiber are important dimensions. They can be calculated from the given membrane geometry and by assuming a certain hollow fiber packing density. Packing density affects the space that is left around each hollow fiber. In this case it is assumed that hollow fibers are packed to a density of 0.5, or in other words that they occupy half of the element's cross section. It follows then that $d_{h,D} = 2 \cdot r_{out}$ and that $A_{c,D} = \pi \cdot r_{out}^2$, where r_{in} and r_{out} are the inner and outer radius of the hollow fiber respectively.

Constant equipment efficiencies are assumed based on data reported in [77, 78, 79]. In reality efficiencies will vary as functions of operating conditions, however this provides a useful first approximation.

Table 5. Conditions for simulation of osmotic power plant

Properties of membrane element		
Water permeability A	$m^3/Pa \cdot s \cdot m^2$	$1.87 \cdot 10^{-12}$
Salt permeability B	$m^3/s \cdot m^2$	$1.11 \cdot 10^{-7}$
Structure parameter S	m	$6.78 \cdot 10^{-4}$
Geometry of membrane element		
Total surface area a_m	m^2	222
Length L	m	1.52
Inner radius of hollow fiber r_{in}	mm	0.25
Outer radius of hollow fiber r_{out}	mm	0.35
Operating conditions		
Temperature T	°C	24
Feed concentration $c_{F,b}$ (z = 0)	g/l	0
Draw concentration $c_{D,b}$ (z = 0)	g/l	35
Equipment specifications		
Pump and motor efficiency $\eta_{pump} \cdot \eta_{motor}$	%	77
Pressure exchanger efficiency η_{px}	%	97
Turbine and generator efficiency $\eta_{turbine} \cdot \eta_{generator}$	%	85
Pickup and pre-treatment head loss $P_{pickup} + P_{filter}$	Pa	0

Using inlet velocities of u_F (x = 0) = u_D (x = 0) = 0.133 m/s [36], the performance of an osmotic power plant is simulated. The results are presented in Figure 21.

The ideal power curve (neglecting all non-ideal effects) is plotted as a function of inlet hydraulic pressure difference ΔP (x = 0) and reveals the maximum power w_{max} = 4.09 W/m^2 that can be obtained from PRO in these conditions.

In the next curve below, the effect of polarization is included, but not the effect of spatial variations. This is equivalent to gross PRO power density at the inlet of a commercial length membrane w_{gross}^{PRO} (x = 0). Polarization leads to a 28 % drop in power density.

The next curve below shows the effect of polarization as well as the effect of spatial variations caused by water and salt mass transfer. This is equivalent to the average power density observed over the full length of the membrane $\overline{w}_{gross}^{PRO}$. An additional 10 % drop in power density results from spatial variations.

Finally the net electric power density curve is plotted. When inlet hydraulic pressure difference of ΔP (x = 0) = 14.80 bar, the net electric power density w_{net}^{e} = 0.18 W/m^2. The overall power plant efficiency is therefore η_{plant} = 4.4 % (= w_{net}^{e} / w_{max} = 0,18 / 4,09).

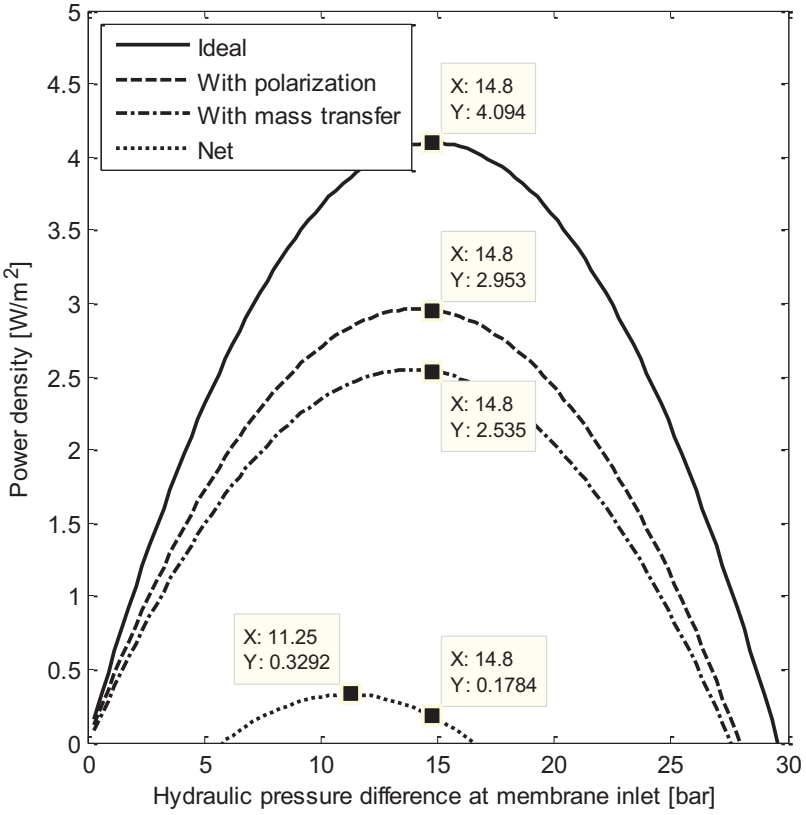

Figure 21. Performance of osmotic power plant operated with inlet velocities u_F (x = 0) = u_D (x = 0) = 0.133 m/s and given the other conditions from Table 5

For the membrane designer, the curve that considers polarization and spatial variations may be of the most interest, because this provides a measure of membrane performance. However, for power production applications it is ultimately the net electric power curve that is of most importance. For an electric utility company the question then becomes, what is the most net electric power that can be generated with the available technology, and what operating conditions are necessary to achieve this? Among the parameters that can be controlled by a system operator are: (1) the feed and draw flow rates $\dot{V}_F$ and $\dot{V}_D$

that are supplied to the system (within the limits of the available resources); and (2) the hydraulic pressure difference ΔP at which the system is operated [10].

From Figure 21 it is clear that the best operating ΔP is significantly lower than the theoretical $\Delta\Gamma_m / 2$. In this case, operating the system at ΔP (x = 0) = 11.25 bar gives net electric power $\widehat{w}_{net}^{e}$ = 0.33 W/m^2, while $\Delta P = \Delta\Gamma_m / 2$ = 14.80 bar gives only w_{net}^{e} = 0.18 W/m^2. This is because there is a diminishing rate of return on the power curve. At some point this rate falls below the rate of system losses as defined by equipment efficiencies. In other words, when equipment efficiencies are low, operation at high pressures becomes increasingly costly and the best ΔP is reduced.

The system operator is also able to control the supply flow rates (and hence velocities). Analysis of equations (20) shows that the polarization boundary layer δ is inversely proportional to flow velocity to the power of κ_1, i.e. $\delta \propto 1/u^{\kappa_1}$. In other words, concentration polarization can be reduced by increasing flow rates to the membrane. By the same token, analysis of equations (26)-(29) shows that spatial variations along the length of the membrane can be minimized by increasing flow rates. This is because, as flow rates increase, water and salt permeate becomes relatively small compared to the bulk flow and concentration. The trade-off to these improvements is that pressure drop along the length of the membrane is proportional to flow velocity. Equations (30) and (31) show that pressure losses along the membrane are proportional to flow velocity to the power of $(2 + \varphi_2)$, i.e. $P_{drop} \propto u^{2+\varphi_2}$.

These competing requirements for reducing non-ideal effects are illustrated by the simulation results shown in Figure 22. Inlet flow velocities are varied between 0 and 0.25 m/s, and the response of effective concentration difference Δc_m, pressure drop P_{drop} and net electric power density W_{net}^{e} is plotted. Simulation results are based on parameters from Table 5 and a hydraulic pressure difference ΔP (x = 0) = 11.25 bar (the best ΔP from Figure 21).

Figure 22 (a) shows Δc_m at both the membrane inlet and outlet. The inlet curve shows that polarization can be reduced up to a certain limit defined by internal polarization (in this case $\Delta c_m \rightarrow 30$ g/l). The outlet curve shows that at low flow rates spatial variations lead to a large drop between Δc_m (x = 0) and Δc_m (x = L). On the other hand, at high flow rates, Δc_m (x = L) $\rightarrow$ Δc_m (x = 0).

Figure 22 (b) shows the rapid increase in both feed side and draw side pressure drops P_{drop} as a function of increasing flow velocity u.

Figure 22 (c) shows the combined effect on net electric power density w_{net}^{e}. The best operating point is clearly observed. At this point the combined effects of polarization, spatial variation, pressure drop, and system losses are balanced and the peak net electric power is achieved. This adjustment in flow velocities gives improved net power by a factor of almost 4 when compared to power obtained with the default velocities $u_F = u_D =$ 0.133 m/s which were used by [36].

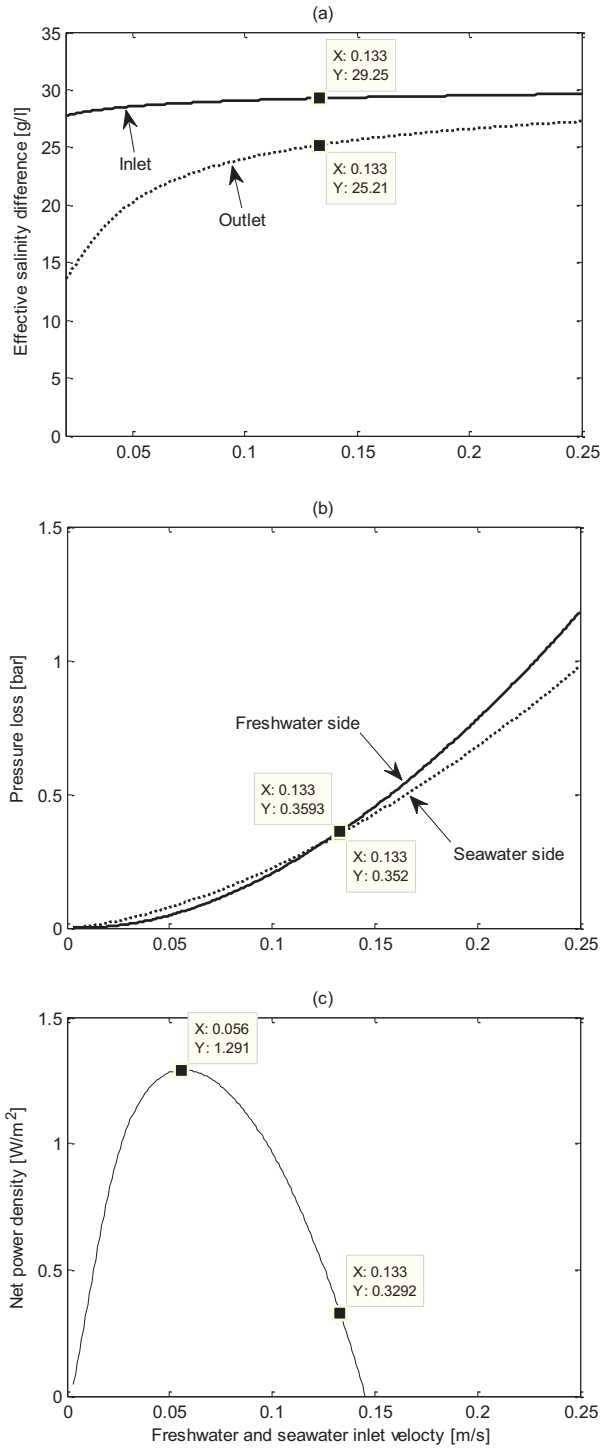

Figure 22. The impact of varying inlet velocities u_F (x = 0) = u_D (x = 0) on (a) effective concentration differences Δc_m (b) pressure losses P_{drop} and (c) net electric power density w_{net}^{e}, when ΔP (x = 0) = 11.25 bar and given the other conditions from Table 5

Net electric power density w_{net}^{e} can further be increased by considering feed and draw velocities u_F and u_D independently from one another, since they do not necessarily have the same effect. Also, for any given combination of flow velocities there exists a best hydraulic pressure difference ΔP. Therefore all three of these variables should be considered independently. The mathematical model is used here to sweep through a range of flow velocities and hydraulic pressure differences, in order to identify the best operating conditions. The simulation results are presented in Figure 23.

Figure 23 (a) shows w_{net}^{e} as a function of inlet velocities u_F (x = 0) and u_D (x = 0), when ΔP (x = 0) = 12.13 bar. The range of velocities considered is from 0 to 0.2 m/s because it is clear from the figure that beyond this there is a drop off in power density. The best inlet velocities are identified as u_F (x = 0) = 0.065 m/s and u_D (x = 0) = 0.050 m/s, yielding w_{net}^{e} = 1.33 W/m^2. Figure 23 (b) shows the best hydraulic pressure difference for these particular flow velocities is ΔP (x = 0) = 12.13 bar. By this approach, net electric power densities are achieved that are more than 7 times greater than those obtained under the default conditions used by [36].

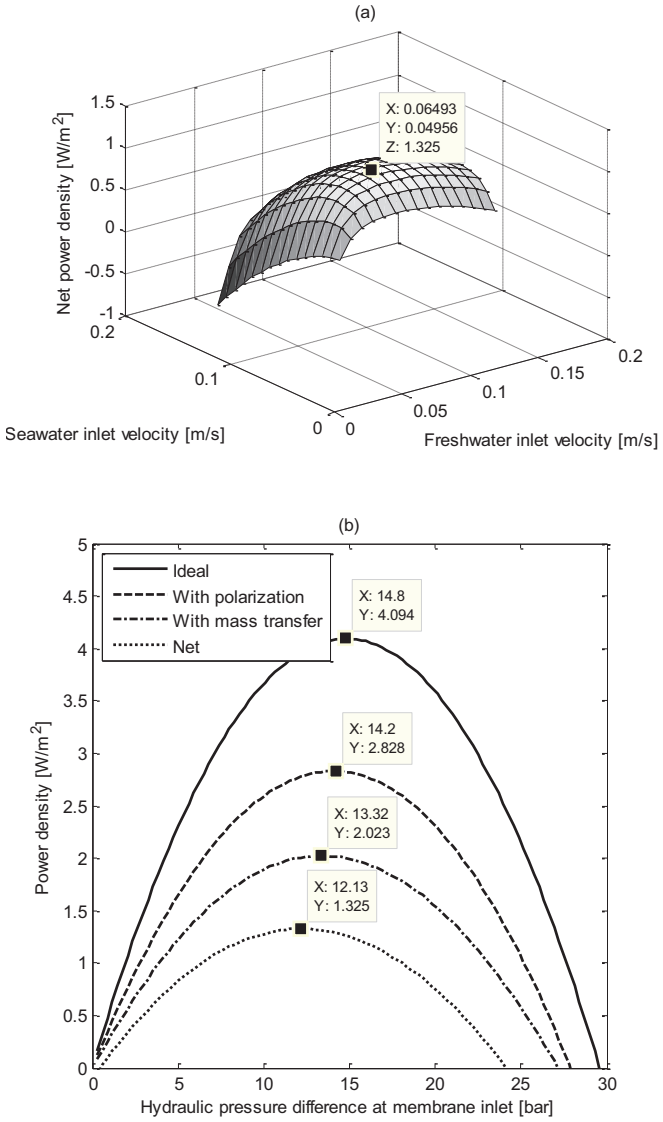

Figure 23. Best operating velocities u (x = 0) and hydraulic pressure difference ΔP (x = 0) for the osmotic power plant described in Table 5

These results represent a very important improvement in system performance. It is difficult however to generalize the findings because they are specific to the particular osmotic power plant studied. Best operating conditions will vary with membrane parameters, with element geometry, with site conditions, and with equipment

specifications. It is useful however to consider the following principles which should be used for achieving best operating parameters of osmotic power systems: (1) as the membrane parameters A↑ and B↓, the best operating velocity u↑; (2) as the membrane length L↓, the best u↑; (3) as the cross sectional profile area a_c↑, the best u↑; and (4) as the equipment efficiencies η↑, the best ΔP↑.

For the sake of comparison, consider a membrane with water permeability A = $10 \cdot 10^{-12}$ $m^3/Pa \cdot s \cdot m^2$, salt permeability B = $3 \cdot 10^{-8}$ $m^3/s \cdot m^2$ and structure parameter S = $4 \cdot 10^{-4}$ m. These parameters have been suggested as membrane design targets [42]. Figure 24 presents the simulation results for the target PRO membrane, holding all other dimensions and inputs as constant from Table 5. The best operating parameters are identified as u_F (x = 0) = 0.132 m/s, u_D (x = 0) = 0.106 m/s and ΔP (x = 0) =13.32 bar. The w_{net}^{e} achieved by such a system is 5.08 W/m^2.

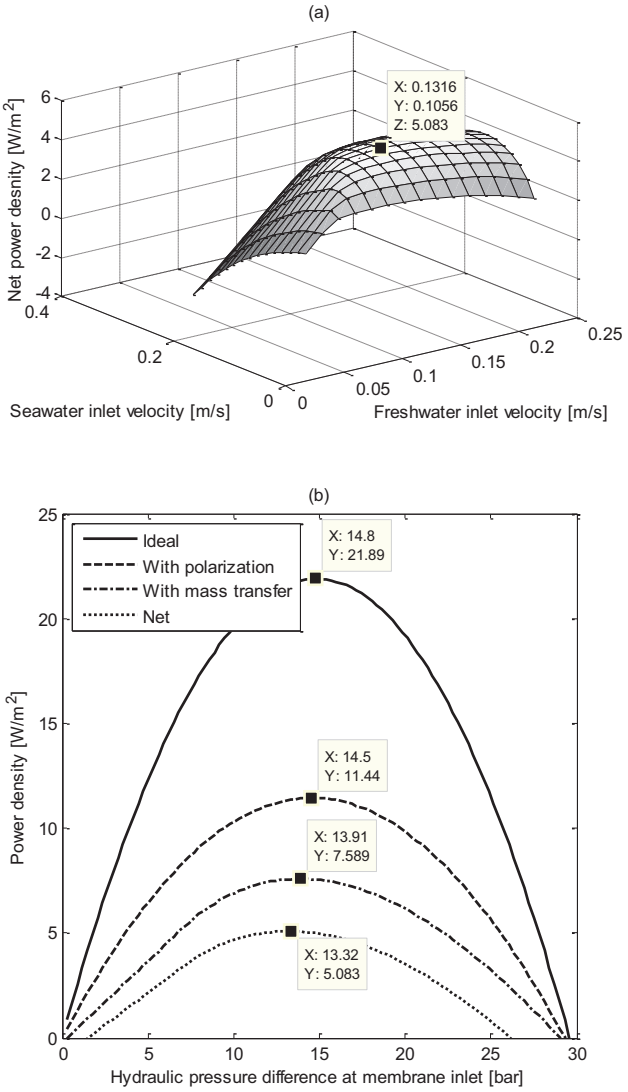

Figure 24. Best operating velocities u (x = 0) and hydraulic pressure difference ΔP (x = 0) for an osmotic power plant with membrane parameters $A = 10 \cdot 10^{-12}$ $m^3/Pa \cdot s \cdot m^2$, $B = 3 \cdot 10^{-8}$ $m^3/s \cdot m^2$ and $S = 4 \cdot 10^{-4}$ m and with other conditions from Table 5

It is interesting also to consider the relationship between feed flow rate $\dot{V}_F$, draw flow rate $\dot{V}_D$, and permeate flow rate $\dot{V}_P$. The ratios of $\dot{V}_P / \dot{V}_F = 0.8$ and $\dot{V}_D / \dot{V}_F = 1.6$ have been suggested by [42] as rules of thumb for flow rates during PRO. For the case illustrated in Figure 24, the best operating conditions give ratios of $\dot{V}_P / \dot{V}_F = 0.74$ and $\dot{V}_D / \dot{V}_F = 1.57$.

For the case illustrated in Figure 23, best operating conditions give ratios of $\dot{V}_P / \dot{V}_F$ = 0.44 and $\dot{V}_D / \dot{V}_F$ = 1.49. These are significantly lower than the suggested rules of thumb. Therefore, while the rules of thumb may be useful for estimating PRO power, improving power output requires that operating conditions be carefully analyzed and controlled.

2.8. Summary

A mathematical model is developed to simulate salinity gradient energy conversion by PRO. The effects of internal and external concentration polarization, spatial variation, pressure drop and power plant system losses are explained. The model is validated against experimental data from the literature.

This is among the first models to consider polarization across the feed side boundary layer. Although this effect is minor at the bench-scale, it becomes more important at the commercial scale where feed side flow rates reduce significantly along the length of the membrane. This is also among the first models to consider spatial variations along the length of commercial membranes. Only some few models have considered variations in flow rates and concentrations, and none (so far as the author is aware) have considered variations in hydraulic pressure.

Several general trends are identified. The drop in concentration difference along the length of the membrane is proportionately greater in high flux membranes and therefore tends to equalize membrane performances. Unless this is addressed it is possible that the potential of new and improved membranes will not be realized at the commercial scale.

Important improvements in net power can be achieved by carefully setting the input feed and draw flow rates, and the hydraulic pressure difference across the membrane. Identifying the best operating conditions is a matter of balancing the competing requirements for reducing different non-ideal effects. While the best flow rates are unique to each particular system, the results suggests that the rule of thumb ratios of $\dot{V}_P / \dot{V}_F = 0.8$ and $\dot{V}_D / \dot{V}_F = 1.6$ do not necessarily yield the most power. Also, due to system losses and equipment inefficiencies, the best hydraulic pressure difference is less than the theoretical $\Delta P < \Delta\Gamma_m / 2$.

Best operating conditions depend on membrane parameters, membrane geometry, equipment efficiencies and site conditions. The following general principles are identified: (1) as the membrane parameter A↑ and B↓, the best operating velocity u↑; (2) as the membrane length L↓, the best u↑; (3) as the channel profile area a_c↑, the best u↑; and (4) as the equipment efficiencies η↑, the best ΔP↑.

3. EXPERIMENTAL INVESTIGATION OF PRESSURE RETARDED OSMOSIS FOR RENEWABLE POWER APPLICATIONS

3.1. Introduction

The first laboratory tests of PRO were conducted by Loeb who achieved gross PRO power densities of 0.35 W/m^2 [16]. Since then many new membranes have been developed and tested and power densities of up to 11.0 W/m^2 have been reported [44]. A summary of PRO laboratory results was presented in Figure 1.

In evaluating and comparing power densities, it is important to recognize that operating conditions used during testing have a significant influence on results [45, 46]. Membranes are tested under a variety of operating conditions, however in general flow rates are set such that cross flow velocities approach 0.25 m/s [67]. The advantage of operating at relatively high flow rates such as these is that non-ideal effects, like external concentration polarization and spatial variations in concentration and flow, are minimized [80]. The disadvantage is that parasitic pressure losses will increase significantly. These losses however are rarely reported in the literature, and yet they can in fact outweigh the advantages of operating at high flow. Consequently, it may be unlikely that similar high flow rates will be used at the commercial scale, and that the reported power densities will be realized. Moreover, the relationship between membrane performance and operating conditions is non-linear, meaning that membranes which perform well at high flow rates may not necessarily be the same that perform well at low flow rates.

In this chapter, an experimental investigation of the PRO process is conducted. A commercial membrane is tested using standard methodology and shows power densities that are among the highest reported in the literature. Experimental results are used to validate the mathematical model over a range of operating conditions. The effect of operating conditions on membrane performance is also examined and an important distinction is made between gross power and net power. This provides important context for the power density results, which so far has been lacking from the literature.

3.2. Experimental Set-Up

An experimental investigation of the PRO process was conducted to further validate the mathematical model described in Chapter 2, and to further study the influence of operating conditions on PRO performance. The investigation was carried out from September 2014 to March 2015 in the Hydro-Québec Laboratoire des Technologies de l'Énergie (Shawinigan, QC) using the bench unit shown in Figure 25.

Solutions are supplied to the membrane cell from 15 l reservoirs via hydrostatic pumps (Cole Parmer, Vernon Hills, IL). Flow rates are set by automated control of pump speed. Hydraulic pressure inside the cell is regulated using a back pressure valve. A thermostatic bath is used to maintain constant solution temperatures. Digital flow meters (Bronkhorst, Ruurlo, Netherlands) located on the draw side inlet and on the feed side inlet and outlet are used to calculate water permeate. For verification, mass change over time is also recorded for the inlet and outlet reservoirs. Digital pressure sensors (Omega, Stamford, CT) are used to measure hydraulic pressure at both the feed and draw inlets and outlets.

Figure 25. PRO bench unit in the Hydro-Québec laboratory (Shawinigan, QC)

Chemical-grade sodium chloride (NaCl) (Fisher Scientific, Waltham, MA) is dissolved in demineralized water to form concentrated solution. Concentrations are measured using a conductivity meter (Hach, Loveland, CO).

Membranes are tested in a custom 4-port rectangular cell with length L = 250 mm and width w = 35 mm. The channel height on both sides of the membrane is h = 1.2 mm. Figure 26 shows the custom cell assembly.

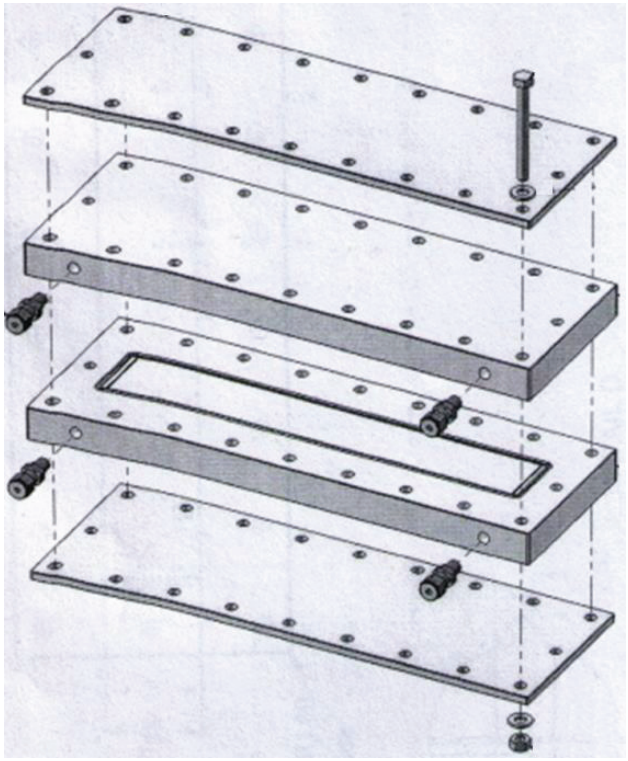

Figure 26. Custom cell for housing membrane samples, with length L = 250 mm, width w = 35 mm, and channel height on both sides of the membrane h = 1.2 mm

Commercial FO membrane samples are handled according to supplier instructions. They are prepared by soaking in demineralized water for 20 minutes. Once secured in the cell, the membrane is rinsed by circulating demineralized water on both sides of the membrane for 20 minutes. The membrane is then 'pressure loaded' for 60 minutes by applying 6.90 bar (100 psi) to the support side of the membrane (which corresponds to the draw side in PRO). Between trials the membrane is rinsed with demineralized water

and is not allowed to dry out. Diamond configuration mesh-type spacers (thickness 0.9 mm, filament spacing 3 mm) are placed on both sides of the membrane.

3.3. Membrane Characterization

In an effort to standardize membrane testing and performance evaluation, a methodology for membrane characterization was proposed by [67]. This methodology is used here to determine water permeability A, salt permeability B and structure parameter S of the membrane. The experimental conditions used during these tests are summarized in Table 6 and further explained in the subsections 3.3.1., 3.3.2. and 3.3.3..

In all cases, trials are conducted over 60 minute intervals, after allowing sufficient time for the system to reach steady-state (approximately 60 minutes). A minimum of 5 trials are conducted for each of the membrane parameter tests. Throughout all trials, solution temperatures are maintained at 20 ± 0.5 °C. Flow rates of 113 ml/min are supplied at the membrane inlet. These flow rates gave inlet flow velocities of only 0.05 m/s, as compared to the recommended velocities of 0.25 m/s. This is due to limits in the bench unit's pumping capacity. This is not expected to influence the results for A, but it may affect the results obtained for B and S, where higher external concentration polarization can obscure the results. In all tests, the membrane is oriented with the active layer facing towards the feed solution, and with the support layer facing towards the permeate or draw solution.

Table 6. Conditions for membrane characterization tests

	Water permeability A	Salt permeability B	Structure parameter S
Description	RO test	RO test	FO test
Temperature	20 °C	20 °C	20 °C
Feed concentration $c_{F,b}$ (x = 0)	0 g/l	2 g/l	0 g/l
Feed flow rate $\dot{V}_F$ (x = 0)	113 ml/min	113 ml/min	113 ml/min
Feed velocity u_F (x = 0)	0.05 m/s	0.05 m/s	0.05 m/s
Draw concentration $c_{D,b}$ (x = 0)	No draw solution is supplied, i.e. only permeate is collected on the side of the membrane opposite the feed solution		58.44 g/l
Draw flow rate $\dot{V}_D$ (x = 0)	n/a	n/a	113 ml/min
Draw velocity u_D (x = 0)	n/a	n/a	0.05 m/s
Hydraulic pressure difference ΔP	6.90 bar (applied to feed side)	6.90 bar (applied to feed side)	0 bar
Trial length	60 min	60 min	60 min
Membrane orientation	Active layer facing feed	Active layer facing feed	Active layer facing feed

3.3.1. Water Permeability of the Membrane

To determine the membrane's water permeability A, a reverse osmosis (RO) test is conducted. Demineralized water is supplied as the feed solution. Hydraulic pressure difference $\Delta P = 6.90$ bar is applied to the feed side. Permeate flow rate $\dot{V}_P$ is recorded and normalized over the membrane's surface area a_m to calculate water permeate flux J_w, as shown in equation (56). The membrane's water permeability A is calculated by dividing J_w by ΔP, as shown in equation (57):

$$J_w = \frac{\dot{V}_P}{a_m} \tag{56}$$

$$A = \frac{J_w}{\Delta P} \tag{57}$$

In the RO water permeability test there is no spatial variation in hydraulic pressure difference ΔP because the compressed channel receives very little flow (only the permeate). This, and the fact that there is no polarization, leads to constant water permeate flux J_w along the membrane.

3.3.2. Salt Permeability of the Membrane

A RO test is conducted to determine the membrane's salt permeability B. Feed solution with concentration $c_F = 2$ g/l is supplied and a hydraulic pressure difference $\Delta P = 6.90$ bar is applied to the feed side. Permeate flow rate $\dot{V}_P$ is recorded using a digital flow meter and the permeate concentration c_P is measured using a conductivity meter. The membrane's salt permeability B is calculated from equation (58):

$$B = J_w \cdot \left(\frac{1-R}{R}\right) \exp\left(-\frac{J_w}{k_F}\right) \tag{58}$$

R is the salt rejection ratio:

$$R = 1 - \frac{c_P}{c_F} \tag{59}$$

3.3.3. Structure Parameter of the Membrane

To determine the membrane's structure parameter S, a forward osmosis (FO) test is conducted. Feed solution is supplied with c_F = 0 g/l (deionized water), and draw solution is supplied with c_D = 58.44 g/l (1M NaCl). The hydraulic pressure on both sides of the membrane is maintained at < 0.07 bar (1 psi), such that the hydraulic pressure difference across the membrane $\Delta P = 0$. Permeate flow rate $\dot{V}_P$ is recorded and the outlet concentrations of the feed and draw solutions c_F (x = L) and c_D (x = L) are measured using a conductivity meter. The structure parameter S is calculated from equation (60):

$$S = \frac{D}{J_w} \cdot \ln\left(\frac{B + A \cdot \Gamma_{D,b}}{B + J_w + A \cdot \Gamma_{F,m}}\right) \tag{60}$$

Where $\Gamma_{D,b}$ is the osmotic pressure of the bulk draw solution and $\Gamma_{F,m}$ is the osmotic pressure of the feed solution at the membrane surface. Because the feed concentration at the membrane surface $c_{F,m}$ cannot be directly measured in order to calculate $\Gamma_{F,m}$, it is assumed that $c_{F,m} = c_{F,b}$. The logarithmic average value between c (x = 0) and c (x = L) is used to account for spatial variations in the feed and draw concentrations.

Experimental results for the A, B, and S parameters are shown in Figure 27. Data points for each of the trials are marked with a red dot. The MATLAB statistical package is used to generate the associated boxplot, with which the outliers are identified (marked with a red cross). The boxplot shows the median (middle red line), 25 percentile (bottom of blue box), 75 percentile (top of blue box) and the maximum and minimum values (extended black lines). The mean water permeability is $A = 11.7 \cdot 10^{-12}$ $m^3/s \cdot m^2 \cdot Pa$ (4.21 LMH/bar). The mean salt rejection is R = 90.3 % and the mean salt permeability is $B = 0.398 \cdot 10^{-6}$ $m^3/s \cdot m^2$ (1.43 LMH). The mean structure parameter is $S = 267 \cdot 10^{-6}$ m. The significance of these values is explained in more detail in Section 3.4.

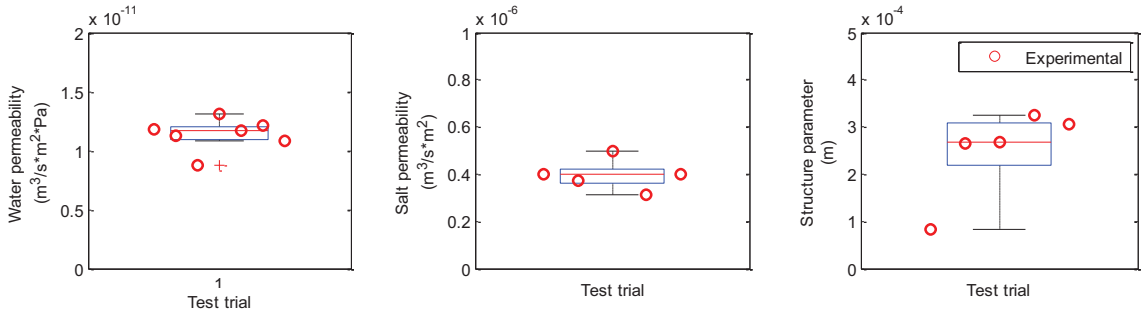

Figure 27. Characteristic membrane parameters A, B, and S determined under test conditions from Table 6; box plot analysis shows the median (middle red line), 25 percentile (bottom of blue box), 75 percentile (top of blue box), range of data (extended black lines), and outliers (red cross)

3.4. Gross PRO Power Density

To evaluate membrane performance PRO tests are conducted by supplying draw solution with concentration $c_{D,b}$ = 30 g/l at hydraulic pressure differences of $\overline{\Delta P}$ = 0, 2, 4, and 6 bar. Feed solution is supplied with concentration $c_{F,b}$ = 0 g/l. Water permeate flow rate $\dot{V}_P$

is recorded, and gross PRO power density $\overline{w}_{gross}^{PRO}$ is calculated from the product of $\overline{J_w}$ and $\overline{\Delta P}$. The test conditions are summarized in Table 7.

Table 7. Conditions for testing gross PRO power density

Description	PRO test
Temperature	20 °C
Feed concentration $c_{F,b}$ (x = 0)	0 g/l
Feed flow rate $\dot{V}_F$ (x = 0)	113 ml/min
Feed velocity u_F (x = 0)	0.05 m/s
Draw concentration $c_{D,b}$ (x = 0)	30 g/l
Draw flow rate $\dot{V}_D$ (x = 0)	113 ml/min
Draw velocity u_D (x = 0)	0.05 m/s
Hydraulic pressure difference $\overline{\Delta P}$	0, 2, 4, 6 bar
Trial length	60 min
Membrane orientation	Active layer facing draw

Experimental results for gross membrane performance are compared against simulation results generated from the mathematical model previously described in Figure 12.

For the mass transfer coefficient in equation (22), values for turbulent flow in a spacer-filled channel are used, namely $\kappa_1 = 0.065 \cdot F$, $\kappa_2 = 0.875$, and $\kappa_3 = 0.25$. F is the spacer correction factor suggested by [61] and [63]. In this case, the constant F = 6 is found to

provide satisfactory results [61]. Turbulent flow is assumed based on reports that such flow can be observed at very low Reynolds numbers (Re < 50) in spacer-filled channels [65, 66].

The hydraulic diameter of a spacer-filled channel can be calculated as described in [60], and in this case $d_h = 2 \cdot h$, given the high porosity of the spacers and given that the channel width is much greater than the channel height.

Figure 28 shows the experimental results for water permeate flux $\overline{J_w}$ and gross PRO power density $\overline{w}_{gross}^{PRO}$ obtained at the hydraulic pressure differences $\overline{\Delta P}$ = 0, 2, 4, and 6 bar. The simulation curve generated from the mathematical model is also provided, and shows good correlation with the experimental data. The coefficient of determination R^2 is also calculated between the simulated curve and the mean of the trials at each $\overline{\Delta P}$.

Water permeate flux $\overline{J_w} = 8 \cdot 10^{-6}$ $m^3/s \cdot m^2$ and gross PRO power density $\overline{w}_{gross}^{PRO} = 5$ W/m^2 were observed experimentally at hydraulic pressure difference $\overline{\Delta P}$ = 6 bar. From the simulation curve it is expected that peak gross PRO power density $\hat{w}_{gross}^{PRO} = 6.6$ W/m^2 can be achieved at hydraulic pressure difference $\overline{\Delta P}$ = 9.9 bar.

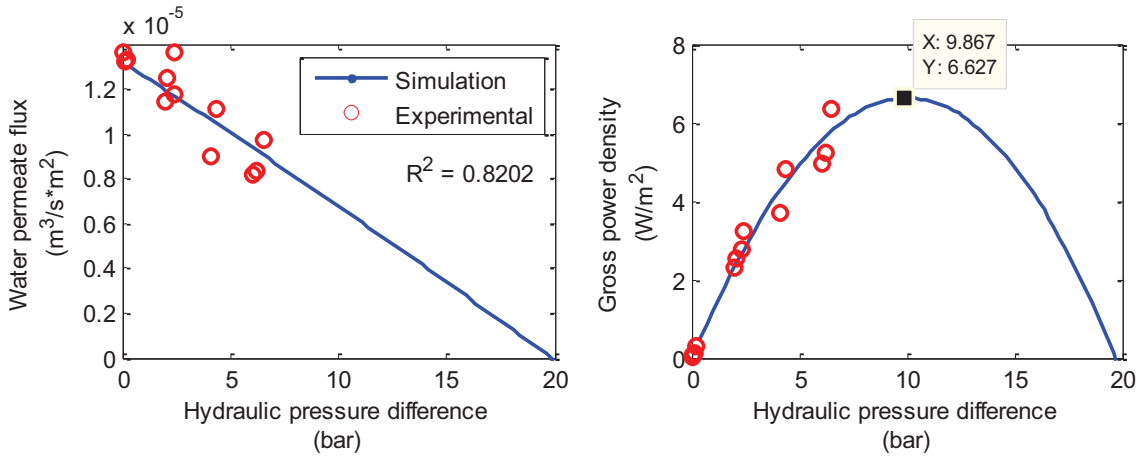

Figure 28. PRO performance under test conditions from Table 7, where experimental results (red points) and simulation results (blue lines) are shown for water permeate flux $\overline{J_w}$ and gross PRO power density $\overline{w}_{gross}^{PRO}$ as functions of hydraulic pressure difference $\overline{\Delta P}$

This evaluation of gross PRO performance is conservative, because it is done with flows that are significantly lower than those used elsewhere in the literature (i.e. u = 0.25 m/s) [67]. As such, concentration polarization and spatial variations will be much more pronounced. The experimental set-up limited the ability to test at high flow, however the mathematical model is used to simulate membrane performance at higher flow rates. Using the suggested flow velocities u_F (x = 0) = u_D (x = 0) = 0.25 m/s, it is possible to achieve gross PRO power density of up to $\overline{w}_{gross}^{PRO}$ = 7.1 W/m^2, when hydraulic pressure difference $\overline{\Delta P}$ = 10.4 bar.

Table 8 shows that the commercial FO membrane tested in this study compares very favorably with other membranes that have been reported in the literature. Gross PRO power density from the FO membrane far exceeds that obtained in the first ever PRO tests [16] and that obtained from another commercially available membrane [36]. It also

surpasses the design objectives suggested in [42]. While certain newly developed membranes show better performance [38, 44], those results are from hand-cast laboratory samples that are not yet commercially available.

Table 8. Comparison of characteristic parameters and performance of various semi-permeable membranes

Membrane	Water permeability A ($\times 10^{-12}$ $m^3/s \cdot m^2 \cdot Pa$)	Salt permeability B ($\times 10^{-6}$ $m^3/s \cdot m^2$)	Structure parameter S ($\times 10^{-6}$ m)	Gross PRO power $\overline{w}_{gross}^{PRO}$ (W/m^2)
Present study, commercial FO	11.70	0.398	267	7.1[a]
Du Pont Permasep, commercial hollow fiber [16]	n/a	n/a	n/a	0.35
HTI-CTA, commercial asymmetric [36]	1.87	0.111	678	2.73
MP, laboratory asymmetric [38]	12.08	0.211	340	9.21
PRO-TFC, laboratory TFC [44]	9.22	0.039	460	11.0
Design targets [42]	10.0	0.030	400	> 5

[a] T = 20 °C, $c_{F,b}(x = 0) = 0$, $c_{D,b}(x = 0) = 30$ g/l, $u_F(x = 0) = u_D(x = 0) = 0.25$ m/s, $\overline{\Delta P} = 10.4$ bar

This study's membrane shows water permeability A that is above the design target and close to those of the high-performance lab membranes. As might be expected however,

this comes with the trade-off of a high salt permeability B. The membrane also shows a structure parameter S that is among the lowest in the literature.

3.5. Net PRO Power Density

Net PRO power density is evaluated for several combinations of feed and draw flow rates between 11.3 ml/min and 113 ml/min. These correspond to flow velocities between 0.005 m/s and 0.05 m/s, and to Reynold's numbers between 10 and 100. Feed solution is supplied with concentration $c_{F,b}$ = 0 g/l and draw solution is supplied with concentration $c_{D,b}$ = 30 g/l. Flow rates and hydraulic pressures at both inlets and outlets are recorded and used to calculate net PRO power density w_{net}^{PRO} using equations (47) and (48). Tests are conducted for hydraulic pressure differences $\overline{\Delta P}$ = 0, 2, 4, and 6 bar. At least 3 trials are conducted at each of the average hydraulic pressures. **Erreur ! Source du renvoi introuvable.** summarizes the conditions for testing net PRO power density.

Table 9. Conditions for testing net PRO power density

Description	PRO test
Temperature	20 °C
Feed concentration $c_{F,b}$ (x = 0)	0 g/l
Feed flow rate $\dot{V}_F$ (x = 0)	11.3, 22.6, 56.5, 113 ml/min
Feed velocity u_F (x = 0)	0.005, 0.01, 0.025, 0.05 m/s
Draw concentration $c_{D,b}$ (x = 0)	30 g/l
Draw flow rate $\dot{V}_D$ (x = 0)	11.3, 22.6, 56.5, 113 ml/min
Draw velocity u_D (x = 0)	0.005, 0.01, 0.025, 0.05 m/s
Hydraulic pressure difference $\overline{\Delta P}$	0, 2, 4, 6 bar
Trial length	60 min
Membrane orientation	Active layer facing draw

Experimental results are again compared against simulation results from the mathematical model previously described in Figure 12. For the friction factor in equation (31), the values suggested by [60] for turbulent flow in a spacer-filled channel are used, $\varphi_1 = 0.3164$ and $\varphi_2 = -0.25$. The R^2 value is calculated between the simulated curve and the mean of the trials at each $\overline{\Delta P}$.

The results in Figure 29 show that membrane performance is significantly influenced by operating conditions. Gross PRO power density $\overline{w}_{gross}^{PRO}$ increases from 1.3 to 6.6 W/m^2 as feed and draw inlet flow rates $\dot{V}_F$ (x = 0) = $\dot{V}_D$ (x = 0) are increased from 11.3 to 113

ml/min. This improvement in gross PRO power density is achieved as the effects of concentration polarization and spatial variations are minimized by the elevated flow rates.

On the other hand, parasitic pressure losses are also proportional to flow rates, as described in equation (30). Figure 29 shows the increase in feed side pressure drop $P_{F,dro}$ (x = L) from 0.3 to 3.5 bar (at the peak power point) as the feed and draw inlet flow rates $\dot{V}_F$ (x = 0) = $\dot{V}_D$ (x = 0) are increased from 11.3 to 113 ml/min. When we consider the power that is required to supply these parasitic loads, we find that the apparent increase in gross PRO power density $\overline{w}_{gross}^{PRO}$ is of little consequence because the overall net PRO power density w_{net}^{PRO} is reduced. Between 11.3 ml/min and 22.6 ml/min there is a modest increase in net PRO power density, from 1.2 to 1.5 W/m^2. However beyond this the increase in parasitic pressure loads become dominant and cancels out any improvement in gross PRO power density. In fact, beyond 22.6 ml/min the net PRO power density actually becomes negative.

Such parasitic pressure losses and the trade-offs associated with operating at high flow rates are rarely considered or reported in the literature. As demonstrated however, they can quickly offset any improvement in gross PRO power density. These results suggest that testing under high flow rates may not be most appropriate for evaluating membrane performance for power production applications, because such conditions are not likely to be used in an industrial power plant. In fact additional pressure losses (such as during pre-filtration) will further reduce net PRO power density and further shift the best operating flow rates to lower values.

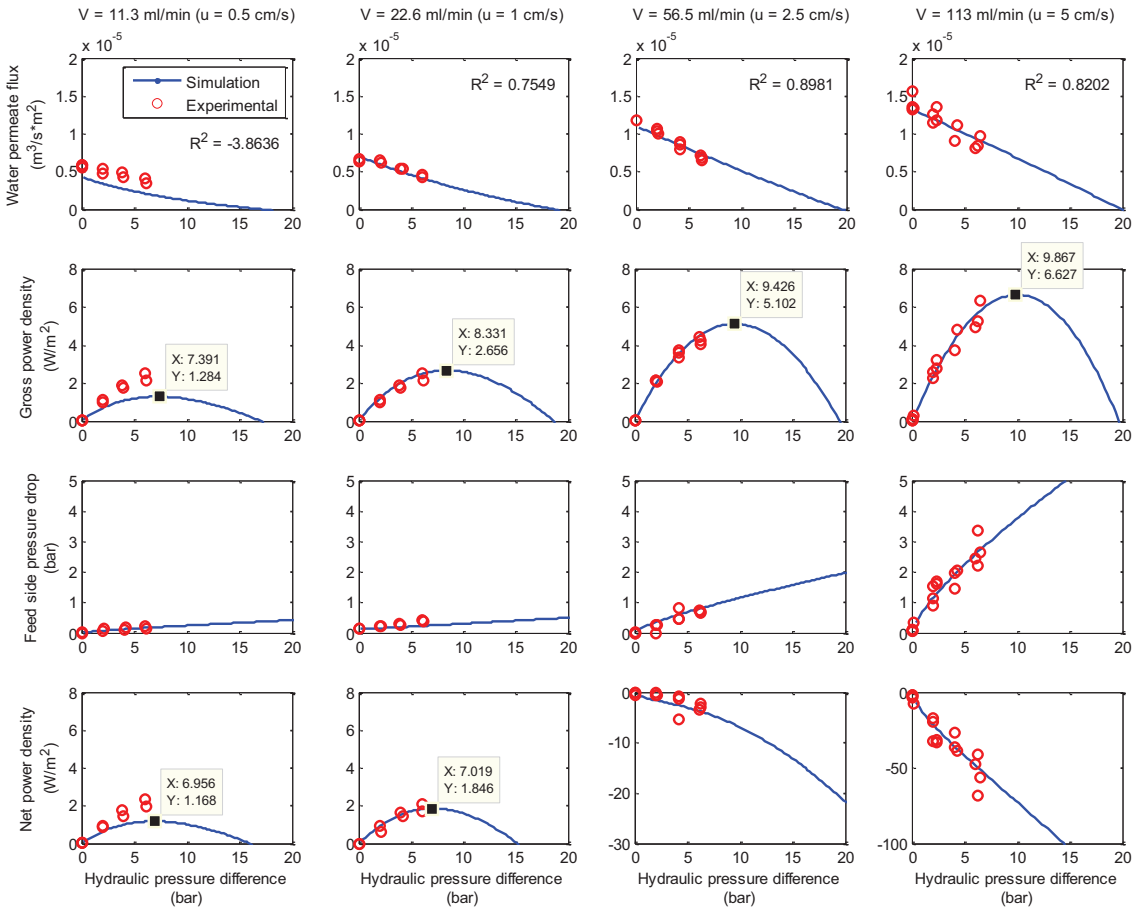

Figure 29. PRO performance under test conditions from Table 9, where experimental results (red points) and simulation results (blue lines) are shown for water permeate flux $\overline{J_w}$, gross PRO power density $\overline{w}_{gross}^{PRO}$, feed side pressure drop $P_{F,drop}$ (x = L), and net PRO power density w_{net}^{PRO}, as functions of hydraulic pressure difference $\overline{\Delta P}$

In Figure 29 only the feed side pressure drop is shown because in this scenario only the pressure drop on this side of the membrane has a significant effect on net power density. This is due to membrane distortion.

Semi-permeable membranes bend under the application of hydraulic pressure, leading to distortion of the membrane and flow channels [81]. In the case of PRO, hydraulic

pressure is applied to the draw side of the membrane. This leads to compression of the feed channel and expansion of the draw channel. Such distortion can have a significant influence on the hydrodynamics of the PRO process. For example, it has been shown that membrane distortion can lead to changes in the characteristic membrane parameters A and B [81]. Also, as the feed channel is compressed the flow velocity in that channel will increase. This will reduce the feed side polarization. Conversely, as the draw side channel expands the draw velocity will decrease and the draw side polarization will become more pronounced.

Pressure losses are particularly affected by membrane distortion because of their strong relationship to channel height. For example, analysis of equations (30) and (31) shows that for rectangular channels when $d_h = 2 \cdot h$, pressure drop is inversely proportional to the cube of the channel height, $P_{drop} \propto 1 / h^3$. A compression of the feed channel will therefore lead to a very large increase in feed side pressure losses. Inversely, expansion of the draw channel will tend to minimize draw side pressure losses.

While certain mathematical models have been proposed to describe membrane distortion under varying operating conditions [81], it is not in the scope of this study to model this dynamic. However, membrane distortion has a significant impact on channel geometry, including hydraulic diameter, which is a very important parameter in many of the equations described previously. Therefore in order to account for it, an empirical relationship based on the experimental data is used to describe membrane displacement as a function of applied hydraulic pressure.

Rearranging equation (30), and using hydraulic diameter $d_h = 2 \cdot h$, the effective height of the flow channel h* can be written as a function of the pressure drop observed along the full membrane length P_{drop} (x = L).

$$h^* = \left(\frac{f \cdot \rho \cdot L \cdot \dot{V}^2}{4 \cdot w^2 \cdot P_{drop}(x = L)} \right)^{1/3} \tag{61}$$

Data for the pressure drop along the whole membrane length P_{drop} (x = L) was collected during the PRO tests from Table 9. This is used in equation (61) to calculate the effective channel height h*. Results are then plotted as a function of applied hydraulic pressure difference ΔP as shown in Figure 30. The proposed empirical relationship has a root mean squared $R^2 = 0.91$:

$$h_F^* = 5.99 \cdot 10^{-5} \cdot \Delta P^{-0.229} \tag{62}$$

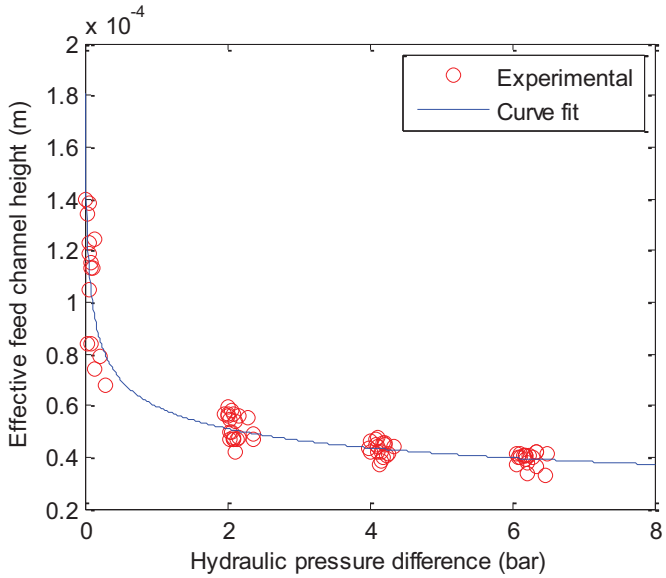

Figure 30. Effective height of the feed side channel h_F* under membrane distortion caused by applied hydraulic pressure difference ΔP

The result suggest that the feed channel is compressed by up to 97% (= h_F* / h_F = 0.00004 / 0.0012) when hydraulic pressure difference ΔP = 6 bar. The data also suggests that once the membrane is pressure loaded during installation it does not return to its original position. For example, Figure 30 shows that even at ΔP = 0 bar the feed channel remains compressed by up to 90% (= h_F* / h_F = 0.00012 / 0.0012).

Compression of the feed channel is accompanied by an exact and opposite expansion of the draw channel, such that the modified draw channel height h_D* = h_D + h_F – h_F*.

In an effort to maximize net PRO power density it is important to observe that while the more significant pressure drop occurs on the feed side (due to compression of that channel by membrane distortion), the more significant external polarization occurs on the draw side. In light of this, it may be possible to simultaneously reduce each of these undesirable effects by increasing draw side flow rates and reducing feed side flow rates.

This is done for 3 cases and the results are shown in Figure 31, where $\dot{V}_F$ (x = 0) = 11.3 and $\dot{V}_D$ (x = 0) = 56.5 ml/min in Figure 31 (a), where $\dot{V}_F$ (x = 0) = 22.6 and $\dot{V}_D$ (x = 0) = 56.5 ml/min in Figure 31 (b), and where $\dot{V}_F$ (x = 0) = 56.5 and $\dot{V}_D$ (x = 0) = 113 ml/min in Figure 31 (c). From among these combinations the highest net PRO power density w_{net}^{PRO} = 4.5 W/m^2 is achieved in case (a). Under these conditions, the pressure drop along the length of the membrane is reduced to almost zero, leading to only a slight difference between w_{net}^{PRO} = 4.5 W/m^2 and the gross PRO power density $\overline{w}_{gross}^{PRO}$ = 4.6 W/m^2.

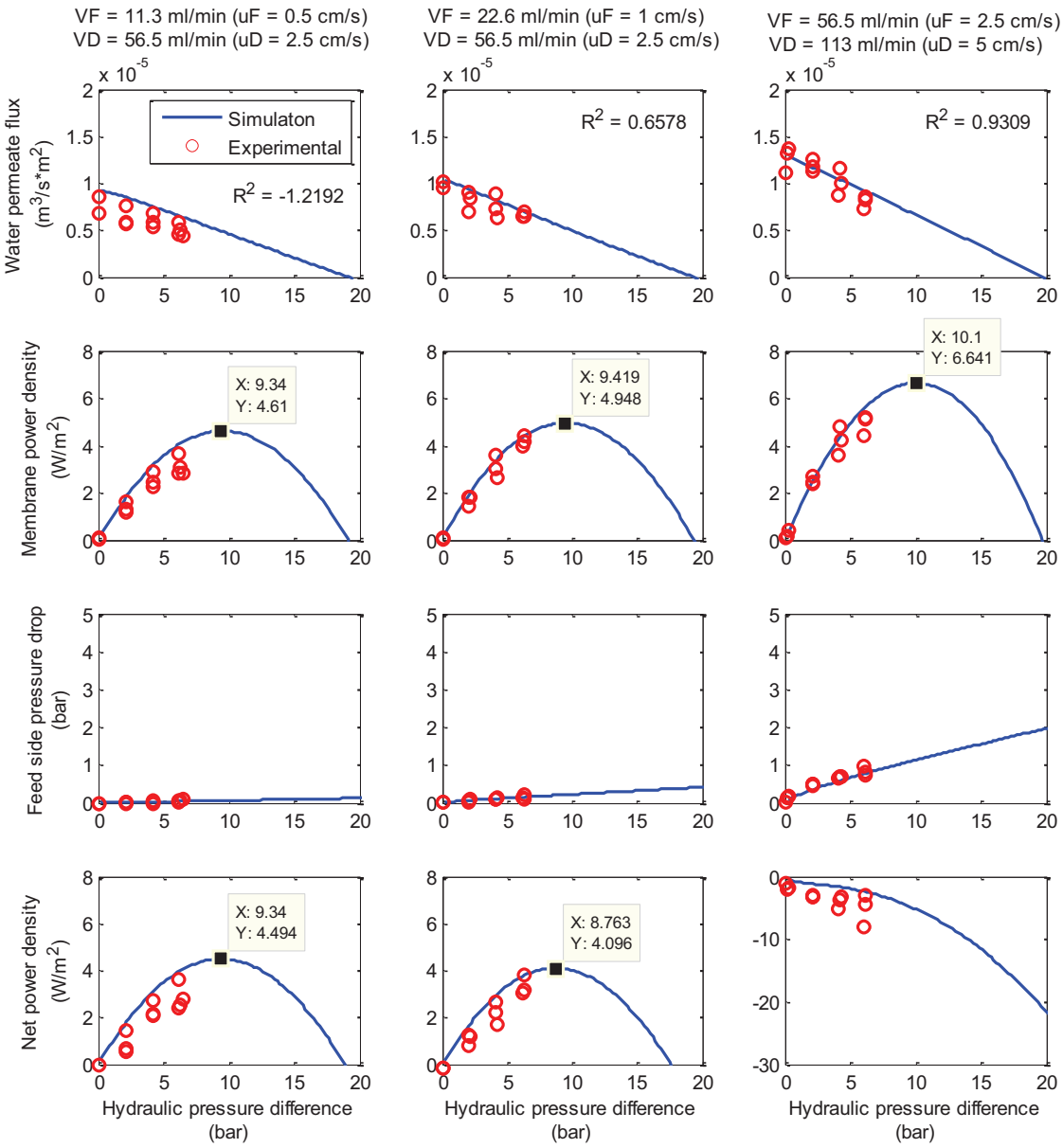

Figure 31. PRO performance under test conditions from Table 9; where experimental results (red points) and simulation results (blue lines) are shown for water permeate flux $\overline{J_w}$, gross PRO power density $\overline{w}_{gross}^{PRO}$, feed side pressure drop $P_{F,drop}$ (x = L) and net PRO power density w_{net}^{PRO}, as functions of hydraulic pressure difference $\overline{\Delta P}$

These results are significant for several reasons. The results show that the gross PRO power density $\overline{w}_{gross}^{PRO}$ = 7.1 W/m^2 observed under the standard test conditions [67], will

not be obtained at the commercial scale because parasitic pressure losses make such high flow conditions inappropriate for power production applications. Using flow rates that balance the trade-off between non-ideal effects can provide a more realistic assessment of membranes and their potential for power production. The results also indicate that even when parasitic loads are considered, this particular membrane can achieve net power density w_{net}^{PRO} = 4.5 W/m^2 which approaches the target of 5 W/m^2.

3.6. Summary

The performance of a commercial membrane is evaluated experimentally. The membrane shows good performance, with gross PRO power density of 7.1 W/m^2 obtained under standard test conditions. This is well above the proposed target of 5 W/m^2, suggesting that PRO membrane technology is approaching commercial viability.

A distinction is made between gross PRO power density, as it is usually reported in the literature, and net PRO power density, which considers parasitic pressure losses and their associated loads. This is among the first investigations of net power density and pressure drop along the length of a membrane in PRO. This analysis provides an insightful perspective on membrane performance. The results clearly demonstrate the trade-off between concentration polarization, spatial variations and pressure losses. While the first two effects can be reduced with high flow, the latter effect is proportional to flow. It is found that in this case (and likely in many others) the high flow rates generally used for PRO testing (flow velocities ~ 0.25 m/s) favor gross PRO power density, but result in negative net PRO density. These test conditions are therefore inappropriate for power

production applications and as such it is unlikely that the power densities seen in the literature will translate to the commercial scale. For future experiments, test conditions that maximize net PRO power density, as opposed to gross PRO power density, should be considered.

In this study inlet feed flow rates of 11.3 ml/min (velocity of 0.005 m/s) and inlet draw flow rates of 56.5 ml/min (velocity of 0.025 m/s) are experimentally shown to strike the right balance between the non-ideal effects and to yield the highest net power density of 4.5 W/m^2. This shows that even after pressure losses are accounted for, membrane performance can approach the 5 W/m^2 target. When other pressure losses and system inefficiencies at the power plant scale are considered, it is expected that power output will be reduced and that best operating flow rates will shift lower so as to minimize these non-ideal effects.

Net PRO power performance is as much an evaluation of the membrane, as it is of the spacer and membrane cell geometry. As such, this analysis can be very useful in optimizing the design of membrane modules, including their configurations, dimensions and materials. It is expected that such analysis can lead to significant improvements in PRO performance

Simulation results from the mathematical model showed good correlation with the experimental data (with the exception of very low flow rates, $Re < 20$). This is among the first models in the literature to be validated across a range of flow rates. The most sensitive and challenging parameters to model include the mass transfer coefficient, the

friction factor and the membrane distortion. Better understanding of these parameters can improve the predictive power of the model and allow it to be applied more generally.

4. ANALOG ELECTRIC CIRCUIT MODEL FOR PRESSURE RETARDED OSMOSIS

4.1. Introduction

Analog electric circuits are useful analysis tools that have found applications in many fields including for hydraulic systems [82]. The comparison is generally made between the flow of water driven by a pressure head in a hydraulic system and the flow of electric charge driven by a potential difference in an electric system. When appropriately applied, this analogy can simplify analysis by allowing circuit software to solve complex systems.

In this chapter an analog electric circuit model is developed to represent the PRO process and power plant. A few publications have considered the application of analog circuits to membrane-based processes but none to PRO [83, 84]. The analog circuit is then used to develop osmotic power system control strategies and to analyze their performance. This is the first such investigation.

4.2. Water and Salt Flux across a Semi-Permeable Membrane

Consider equation (2) which describes water permeate flux J_w across a semi-permeable membrane as a function of the pressure gradient $\Delta\Gamma_m - \Delta P$ and as a function of the membrane's water permeability A. This equation has the same form as Ohm's law and a useful analogy can be made. In PRO, the flow of water across a membrane driven by a pressure gradient can be analogous to the flow of electric charge through a resistance driven by a potential difference. The analogy is illustrated in Figure 32 (a), where ρ_A is

the membrane's resistivity to water, which is the inverse of the membrane's water permeability A:

$$\rho_A = \frac{1}{A} = \frac{\Delta\Gamma_m - \Delta P}{J_w} \tag{63}$$

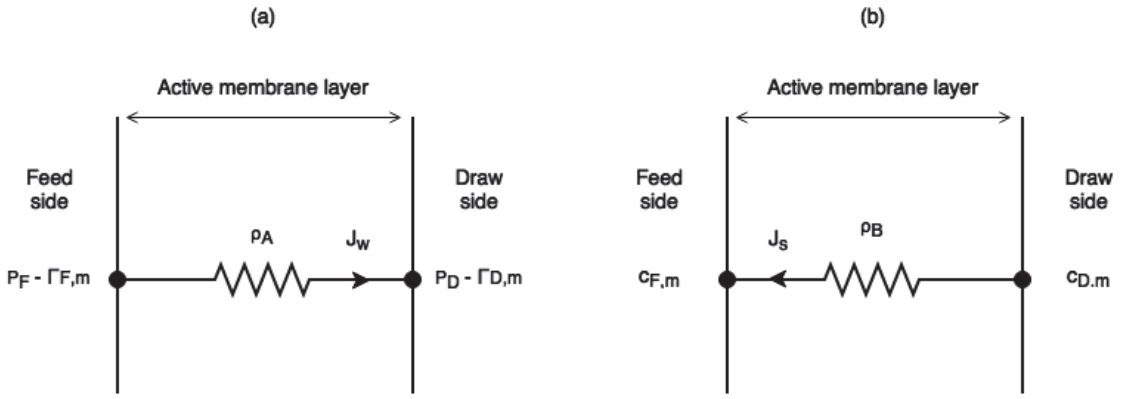

Figure 32. (a) Analog circuit for water permeate across a semi-permeable membrane as driven by pressure retarded osmosis, and (b) analog circuit for salt permeate (reverse salt leakage) across a semi-permeable membrane as driven by diffusion

The osmotic pressures in Figure 32 (a) are shown as negative values. This is because osmotic pressure is technically defined as the pressure required to stop osmosis. Therefore the osmotic pressure difference will be given as the balance between the negative feed side and negative draw side osmotic pressures $\Delta\Gamma_m = -\Gamma_{F,m} - -\Gamma_{D,m} = \Gamma_{D,m} - \Gamma_{F,m}$. The hydraulic pressure difference across the membrane will be the balance of the draw side and feed side hydraulic pressures $\Delta P = P_D - P_F$. The osmotic pressure drives the water permeate flux, while the hydraulic pressure opposes (i.e. retards) the flux.

A similar analogy can be made for reverse salt flux across a semi-permeable membrane. Consider equation (3) which describes reverse salt flux J_s as a function of the

concentration difference across the membrane $\Delta c_m = c_{D,m} - c_{F,m}$ and as a function of the membrane's permeability to salt B. Figure 32 (b) shows the analog circuit for the process, where the flow of salt is analogous to the flow of electric charge, and where the driving concentration difference is analogous to a potential difference. ρ_B is the membrane's resistivity to salt and is the inverse of the membrane's salt permeability B:

$$\rho_B = \frac{1}{B} = \frac{\Delta c_m}{J_s} \tag{64}$$

Salt flux is in the opposite direction to water flux, and hence is referred to as reverse salt leakage due to its undesirability. Figure 32 (a) and (b) are separate circuits each representing their own unique analogy. In the first, water flux is driven by the pressure gradient in a process known as pressure retarded osmosis. In the other, salt flux is driven by the concentration gradient in a process known as diffusion.

4.3. Concentration Polarization

Concentration polarization refers to the non-linear concentration gradient that develops across the profile of a semi-permeable membrane during PRO. This gradient is the result of accumulating salt within the membrane's support layer and boundary layers. It can be described by the solution-diffusion model:

$$J_s = D \cdot \frac{dc}{dy} - J_w \cdot c \tag{65}$$

This equation can be solved analytically, and the solution was previously presented in equation (14). It can also be solved by considering an electric circuit analogy of the phenomenon. To develop the analogy, consider each part of equation (65) individually: the diffusion component $D \cdot dc / dy$ and the convection component $J_w \cdot c$. Let the diffusion component equal $J_{s,d}$ and the convection component equal $J_{s,v}$. Writing these in discrete form gives:

$$J_{s,d} = D \cdot \frac{c_{(j+1)} - c_{(j)}}{\Delta y} \tag{66}$$

$$J_{s,v} = J_w \cdot c_o \tag{67}$$

The equation for the diffusion component has the same form as Ohm's law. Therefore the diffusion of salt $J_{s,d}$ across a finite section of the membrane profile Δy driven by a concentration difference $c_{(j+1)} - c_{(j)}$ can be analogous to current driven across a resistance by a potential difference. The salt resistivity of the profile section ρ_y is:

$$\rho_y = \frac{\Delta y}{D} = \frac{c_{(j+1)} - c_{(j)}}{J_{s,d}} \tag{68}$$

Given the thickness of the support layer λ (or its effective thickness S) and the thickness of the feed and draw boundary layers δ_F and δ_D, the salt resistivity for each of the polarization layers is:

Across the support layer:

$$\rho_S = \frac{\lambda}{D_S} = \frac{S}{D_F} \tag{69}$$

Across the feed side boundary layer: $$\rho_{\delta_F} = \frac{\delta_F}{D_F} = k_F \quad (70)$$

Across the draw side boundary layer: $$\rho_{\delta_D} = \frac{\delta_D}{D_D} = k_D \quad (71)$$

The equation for convection describes the movement of salt that is carried by the water permeate J_w, which has a concentration c_o that is the average over the discretized profile section. This can be analogous to a controlled current source.

When both convection and diffusion are combined using Kirchoff's current law, the resulting analog circuit is given in Figure 33.

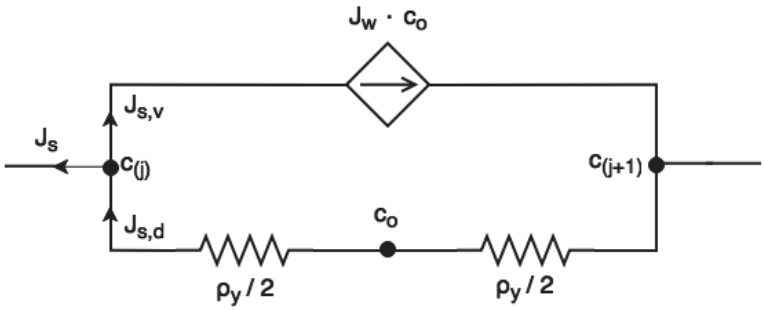

Figure 33. Analog circuit for salt flux across the polarization layer of a membrane profile, shown as the equilibrium between pressure driven convection and concentration driven diffusion

This 2-node block represents convection and diffusion of salt over a finite section of the membrane profile. The complete profile is modeled by dividing each polarization layer into sub sections and connecting several of these 2-node blocks in series, with one block for each section. As the number of blocks is increased and approaches infinity, the size of the discretized space is reduced and the accuracy of the model approaches the actual

behavior. The salt resistivity of each subsection will be ρ_y / m, where m is the number of sub sections. This approach is illustrated in Figure 34.

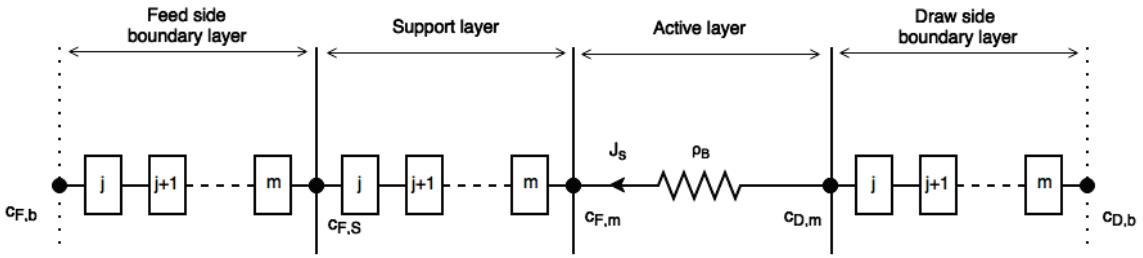

Figure 34. Analog circuit for concentration polarization across the whole membrane profile, where each polarization layer is divided in to m number of blocks, and each block is from Figure 33

So far as the author is aware, this is the first analog electric circuit model for describing concentration polarization during PRO. A few publications have developed similar models but for other applications [83, 84].

This analog circuit represents the solution-diffusion equation and can be easily solved using standard circuit analysis software. To illustrate, the circuit is built in Simulink and the software's circuit solver is used to find water and salt flux under the conditions summarized in Table 10. For simplicity, constant feed and draw side polarization layers $\delta_F = \delta_D = 30 \cdot 10^{-6}$ m are assumed [76], as well as constant salt diffusion coefficient D = $1.5 \cdot 10^{-9}$ m^2/s [36].

Table 10. Conditions used during simulation of analog circuit for concentration polarization across the membrane profile

Operating conditions			
Temperature T	20 °C		
Feed concentration $c_{F,b}$	0 g/l		
Draw concentration $c_{D,b}$	30 g/l		
Hydraulic parameters		**Circuit parameters**	
Water permeability A	$10 \cdot 10^{-12}$ $m^3/Pa \cdot s \cdot m^2$	Water resistivity ρ_A	$10 \cdot 10^{10}$ $Pa \cdot s/m$
Salt permeability B	$3 \cdot 10^{-8}$ $m^3/s \cdot m^2$	Salt resistivity ρ_B	$3.33 \cdot 10^7$ s/m
Structure parameter S	$4 \cdot 10^{-4}$ m	Support layer salt resistivity ρ_S	$2.67 \cdot 10^5$ s/m
Boundary layer thickness δ	$30 \cdot 10^{-6}$ m	Boundary layer resistivity ρ_δ	$2 \cdot 10^4$ s/m
Diffusion coefficient D	$1.5 \cdot 10^{-9}$ m^2/s		

The simulation results from the analog circuit are presented together with results from the validated mathematical model. Two cases are shown for the analog circuit, where the

polarization layers are divided into a number of sections m = 2, and m = 5 respectively. The latter case shows very good correlation with the validated mathematical model.

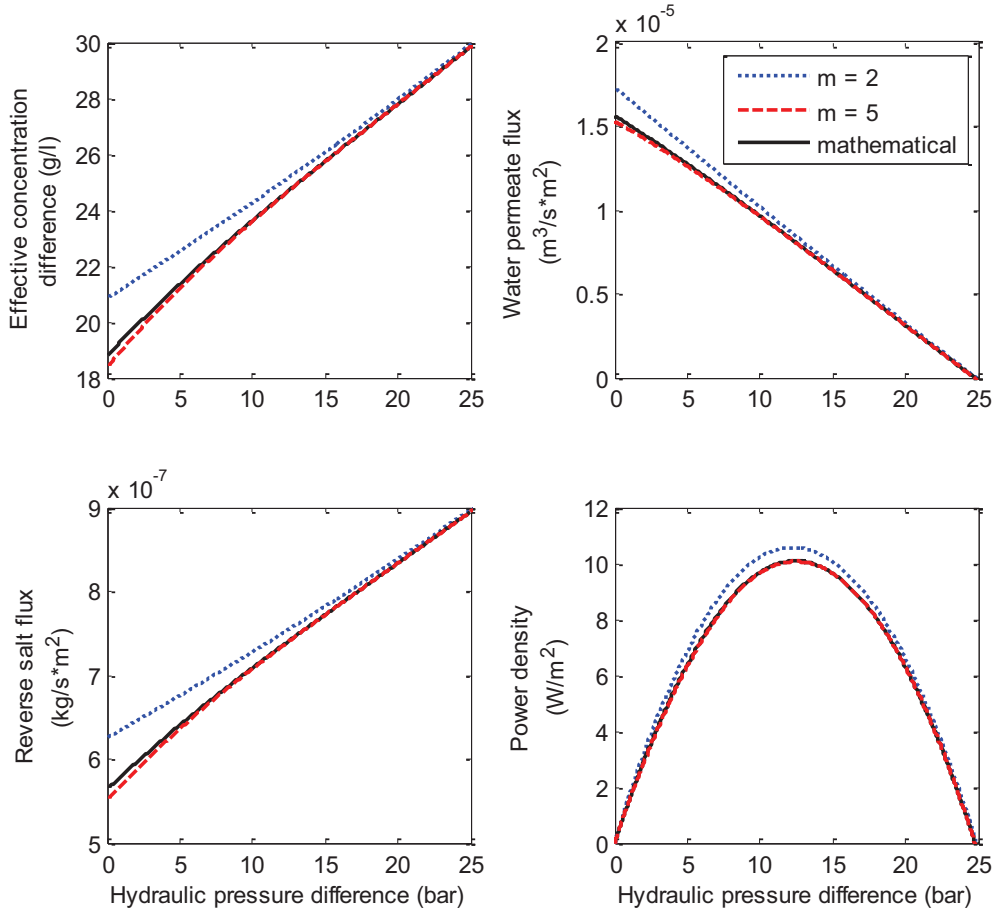

Figure 35. Effective concentration difference Δc_m, reverse salt flux J_s, water permeate flux J_w, and gross PRO power density w_{gross}^{PRO} as a function of hydraulic pressure difference ΔP for the mathematical model and the analog circuit model under the conditions from Table 10

This representation of the solution-diffusion equation refers to concentration polarization at steady state. A more complete expression should consider the transient behavior of water and salt flux across the membrane profile. The main dynamic component of such a

system is the potential for a volume of water to store salt as dissolved solute. This is analogous to the potential for a capacitor to store electric charge. Therefore, a more complete expression for the salt flux J_s is [85]:

$$J_s = D \cdot \frac{dc}{dy} + C \cdot \frac{dc}{dt} - J_w \cdot c \tag{72}$$

C is the salt capacitance of the water volume. C is also equal to the thickness of the profile section, which in discretized form is $C = \Delta y$. The improved analog circuit is presented in Figure 36.

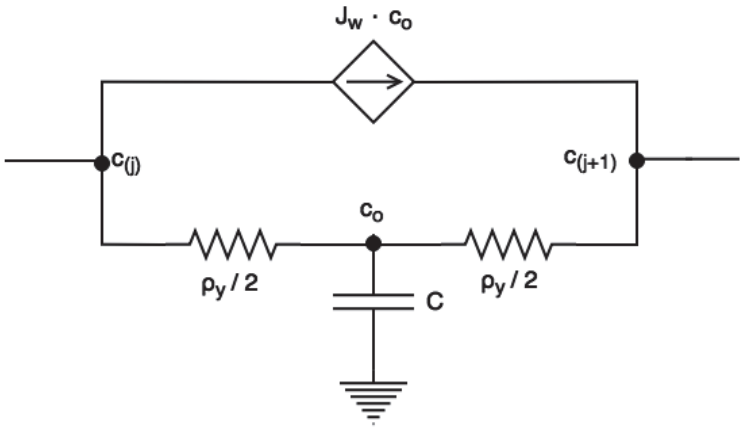

Figure 36. Analog circuit for salt flux across the polarization layer of a membrane profile when the salt storage capacity of water is considered

Given this capacitance, the step response of the system to a change in the applied hydraulic pressure difference is illustrated in Figure 37. At time t = 25 s the hydraulic pressure difference is increased from $\Delta P = 0$ (which is the condition for forward osmosis) to $\Delta P = 12.7$ bar (which is the peak power point). The resulting change in effective concentration difference, reverse salt flux $J_{s,}$, water permeate flux J_w, and gross PRO

power density w_{gross}^{PRO} are plotted in solid black. The same conditions from Table 10 are used and the polarization layers are subdivided into m = 5 sub sections. The steady-state conditions match those obtained from the validated mathematical model, which are marked in dashed red. The time constant is $4 \cdot \tau = 26$ sec.

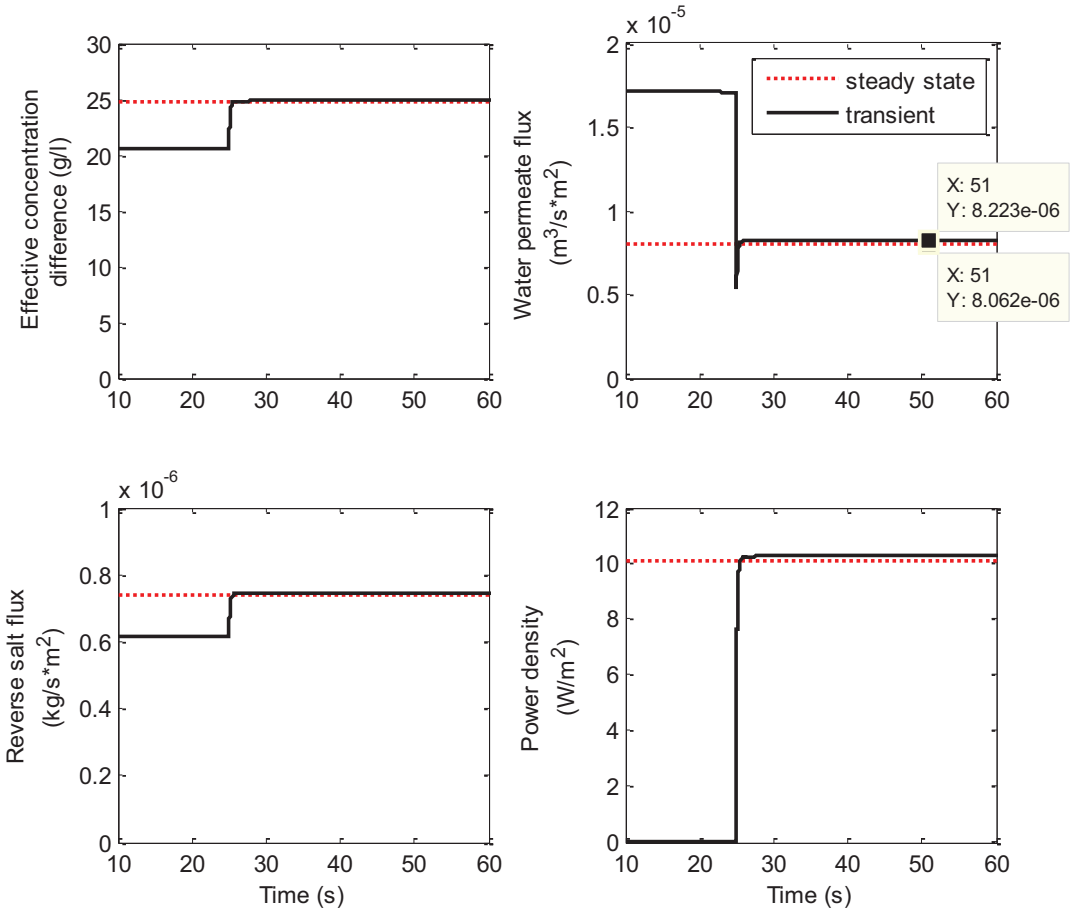

Figure 37. Dynamic response of effective concentration difference Δc_m, water permeate flux J_w, reverse salt flux J_s, and gross PRO power density w_{gross}^{PRO} to a step change in hydraulic pressure difference from $\Delta P = 0$ bar to $\Delta P = 12.5$ bar at time t = 25 s

4.4. Spatial Variations

Water and salt permeate across the membrane lead to variations in flow rates and concentrations along the length of the membrane. These will lead to spatial variations in the concentration polarization profile. To consider this, the analog circuit for polarization should be solved for finite pieces of the membrane length. This can be done by placing several branches of the water flux and salt flux circuits in parallel, with resistances adjusted to represent the equivalent area accounted for by each branch. By so doing, flow rates and concentrations are updated along the membrane length.

It is also important to consider variations in hydraulic pressure that are the result of pressure drops along the membrane length due to friction. The pressure drop along the length of a membrane was previously described in equation (30).

$$P_{drop} = \frac{f \cdot \rho \cdot u^2 \cdot L}{2 \cdot d_h} \tag{73}$$

f is the friction factor and is again given here:

$$f = \varphi_1 \cdot Re^{\varphi_2} \tag{74}$$

Consider pressure analogous to voltage and flow rate analogous to current. The term u^2 in equation (73) suggests that pressure drop (voltage) is non-linearly proportional to flow rate (current), and hence does not follow Ohm's law. However, when equation (74) is expanded and combined with equation (73), Ohm's law is satisfied under the condition that $\varphi_2 = -1$. For simplicity, it is assumed here that $\varphi_2 = -1$, however in reality φ_2 will

vary as a function of flow regime and membrane configuration. For more realistic modeling, $\varphi_2 \neq -1$ can be used if cross flow resistance is modelled with a current controlled variable resistor. Using the assumption that $\varphi_2 = -1$, the expression for cross-flow resistance R_{drop} becomes:

$$R_{drop} = \frac{\varphi_1 \cdot \mu \cdot L}{2 \cdot a_c \cdot {d_h}^2} \tag{75}$$

μ is the flow viscosity and a_c is the cross-sectional area of the flow channel.

A complete analog circuit model for PRO across a semi-permeable membrane is presented in Figure 38. The model consists of two distinct circuits that communicate. In Figure 38 (a) water volumetric flow rate $\dot{V}$ is analogous to current, and pressures (both hydraulic and osmotic) are analogous to voltage. The basic building block for the circuit is from Figure 32 (a). The membrane length is divided in to n number of pieces. The water permeate $J_w \cdot a_m / n$ across each membrane piece i is driven by the balance of the osmotic pressure difference $\Delta\Gamma_m$ and the hydraulic pressure difference $\Delta P = P_D - P_F$. Osmotic pressure difference is controlled by the effective concentration difference Δc_m which is measured across the active membrane layer in Figure 38 (b). Hydraulic pressure difference changes along the length of the membrane because of pressure drop across the resistance R_{drop} / n.

In Figure 38 (b) salt mass flow rate $\dot{m}$ is analogous to current, and concentration is analogous to voltage. The basic building block for this circuit is from Figure 34 and Figure 36. The salt permeate $J_s \cdot a_m / n$ across each membrane piece i is driven by the

balance of salt diffusion and salt convection. Diffusion is driven by the bulk concentration difference $\Delta c_b = c_{D,b} - c_{F,b}$ and at each branch the bulk feed and bulk draw concentrations $c_{F,b}$ and $c_{D,b}$ are controlled by dividing incoming salt mass flow rate $\dot{m}$ and water volumetric flow rate $\dot{V}$. Convection is driven by water permeate J_w, which is measured across the corresponding branch in Figure 38 (a). The membrane's polarization profile is divided into m sections. The measured value for water permeate is input to each section j. The salt resistance for each polarization section is $(\rho_y / m) \cdot (n / a_m)$. The salt capacitance of each polarization section is $(C / m) \cdot (a_m / n)$.

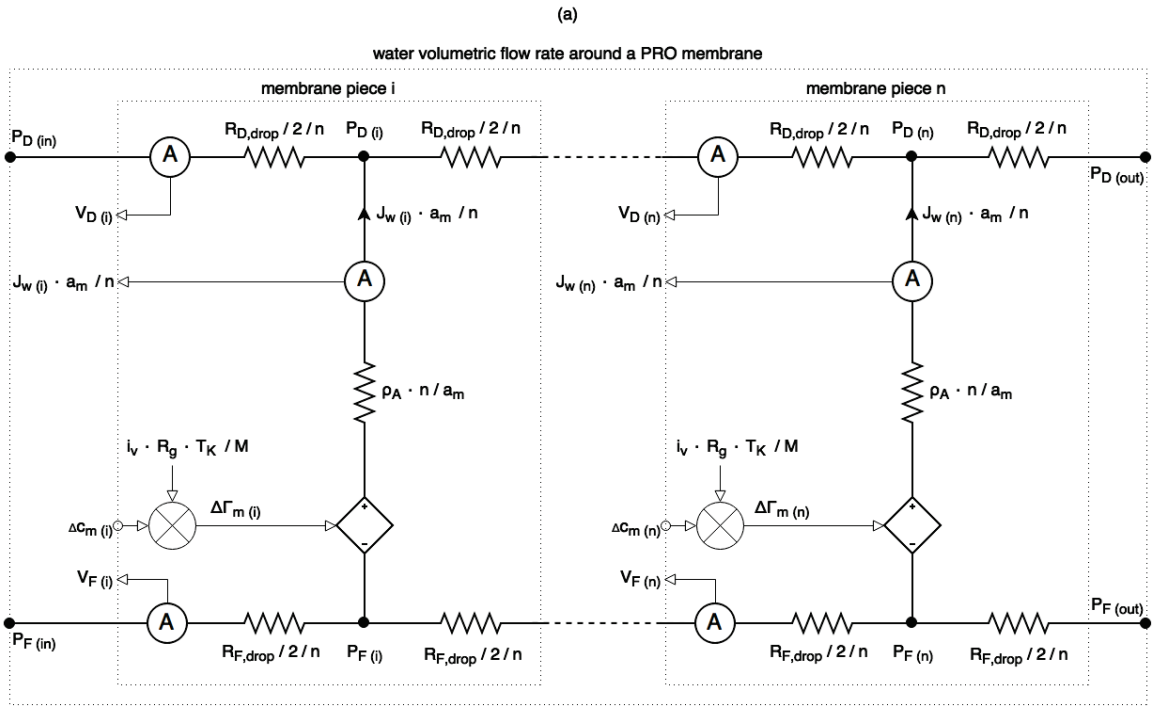

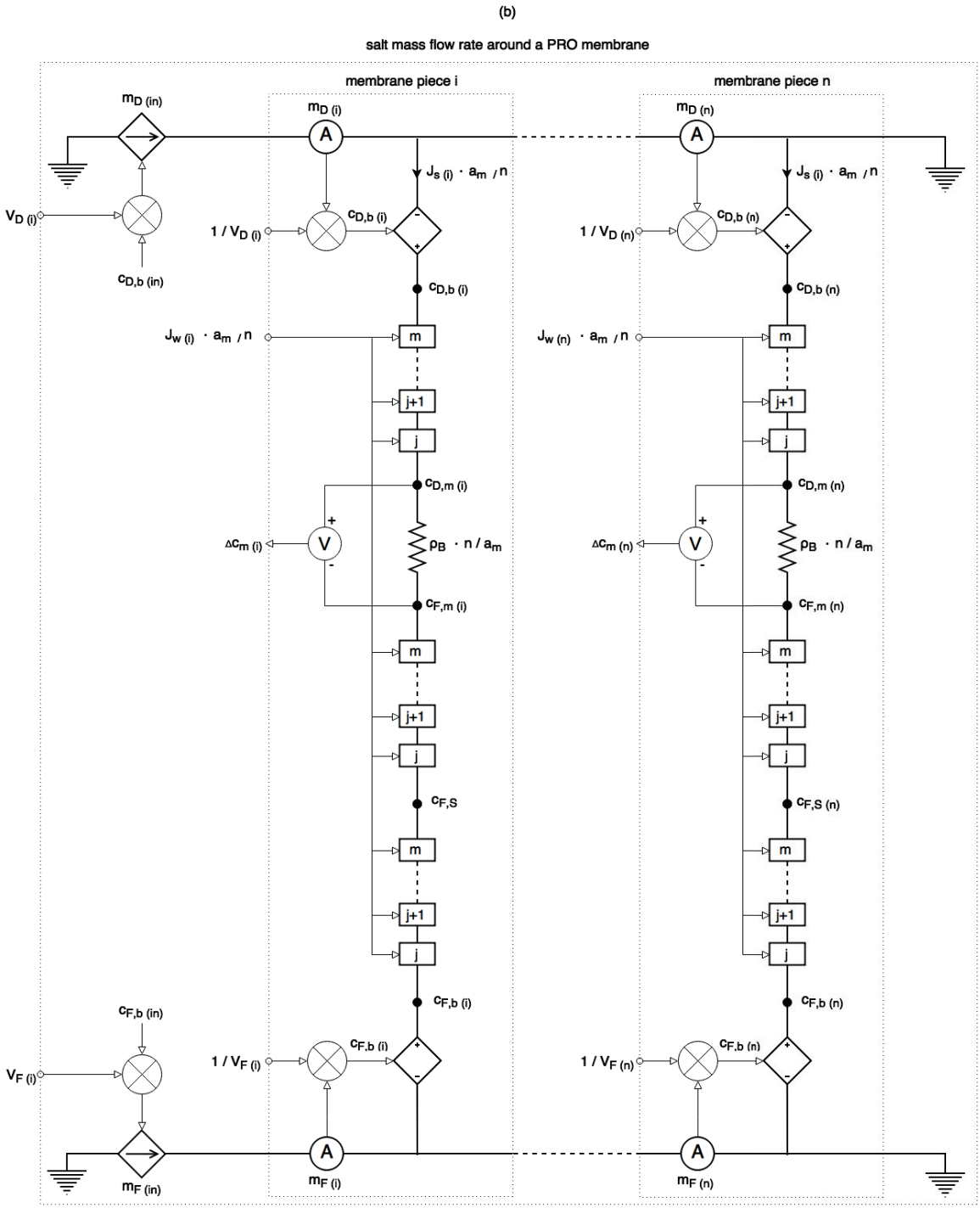

Figure 38. Complete analog circuit for PRO process across a semi-permeable membrane representing (a) water volumetric flow rate and (b) salt mass flow rate with consideration for concentration polarization, spatial variations along the length of the membrane, and pressure drop

This analog circuit is built in Simulink and the software is used to simulate water and salt flux along the length of the membrane under conditions from Table 11. The membrane length is divided into n = 5 number of pieces. The polarization layers are divided into m = 5 number of sections. The membrane is a commercial scale module with total surface area a_m = 200 m^2. Constant values for the channel geometry, friction factor and viscosity are assumed, such that the cross-flow resistance R_{drop} is the same over both sides of the membrane. The hydraulic pressure difference is maintained at $\Delta P_{(in)}$ = 9.8 bar and the flow rates are set at $\dot{V}_{F\,(in)}$ = 0.0018 m^3/s and $\dot{V}_{D\,(in)}$ = 0.0028 m^3/s.

Table 11. Conditions used during simulation of complete analog circuit for PRO across a semi-permeable membrane

Operating conditions			
Temperature T	20 °C		
Feed concentration $c_{F,b\,(in)}$	0 g/l		
Draw concentration $c_{D,b\,(in)}$	30 g/l		
Hydraulic parameters		**Circuit parameters**	
Water permeability A	$10 \cdot 10^{-12}$ $m^3/Pa{\cdot}s{\cdot}m^2$	Water resistivity ρ_A	$10 \cdot 10^{10}$ $Pa{\cdot}s/m$
Salt permeability B	$3 \cdot 10^{-8}$ $m^3/s{\cdot}m^2$	Salt resistivity ρ_B	$3.33 \cdot 10^7$ s/m

Structure parameter S	$4 \cdot 10^{-4}$ m	Support layer salt resistivity ρ_S	$2.67 \cdot 10^{5}$ s/m
Boundary layer thickness δ	$30 \cdot 10^{-6}$ m	Boundary layer resistivity ρ_δ	$2 \cdot 10^{4}$ s/m
Diffusion coefficient D	$1.5 \cdot 10^{-9}$ m^2/s	Cross flow resistance R_{drop}	$7.19 \cdot 10^{3}$ $Pa \cdot s/m^3$
Membrane surface area a_m	200 m^2	Capacitance of support layer C_S	$4 \cdot 10^{-4}$ m
Flow channel cross sectional area a_c	0.033 m^2	Capacitance of boundary layer C_δ	$30 \cdot 10^{-6}$ m
Membrane length L	1.5 m		
Hydraulic diameter of flow channel d_h	0.001 m		
Flow viscosity μ	0.001 Pa·s		
Friction factor constant φ_1	0.3164		
Friction factor constant φ_2	– 1		

The simulation results for the analogous circuit are given in Figure 39, together with the simulation results from the validated mathematical model. The analog circuit agrees well

with the mathematical model. The correlation improves as the length of the membrane is divided into a larger number of pieces.

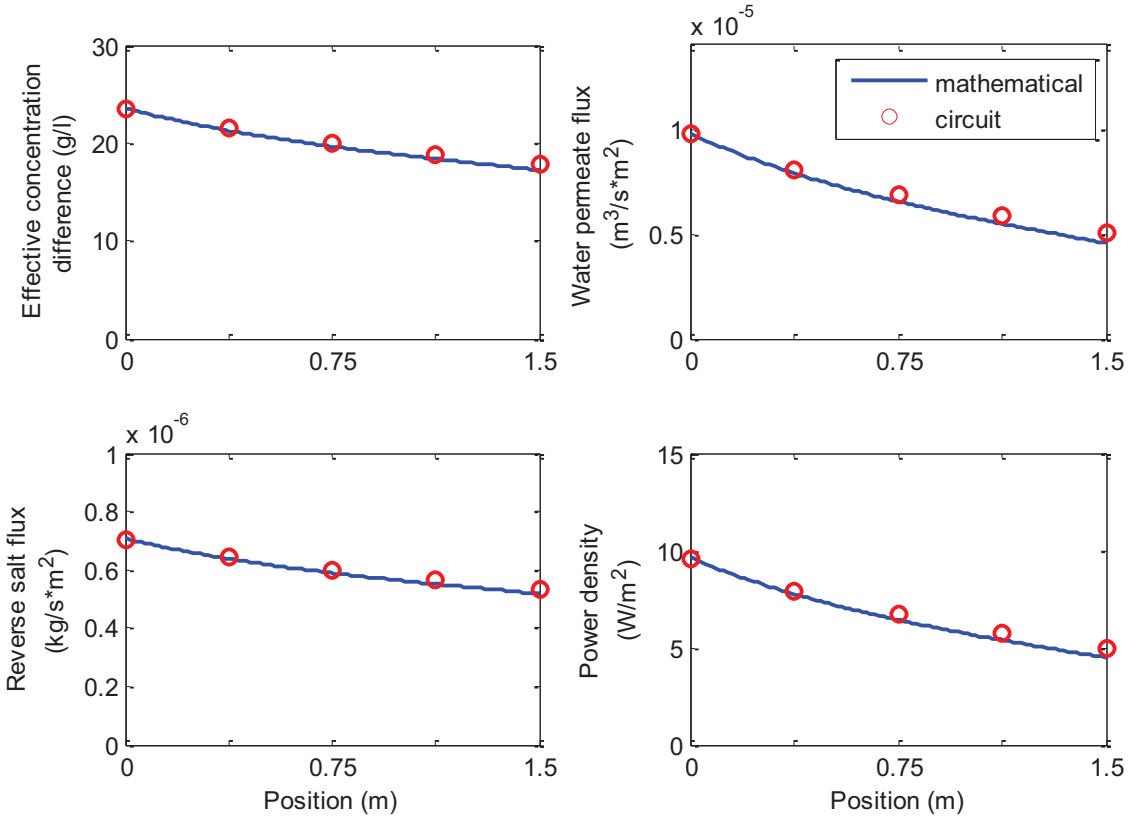

Figure 39. Effective concentration difference Δc_m, water permeate flux J_w, reverse salt flux J_s, and gross PRO power density w_{gross}^{PRO} as a function of position along the length of the membrane from the complete analogous circuit and the validated mathematical model under the conditions from Table 11

4.5. Osmotic Power System

The complete analog circuit presented in the previous section represents a semi-permeable membrane including all of its resistances to water and salt mass transfer. In order to operate, this semi-permeable membrane must be supplied with feed and draw

solutions, the draw side must be pressurized, and a load must be connected to extract power. The simplified osmotic power plant illustrated in Figure 40 can be used to do each of these. The system consists of a feed pump, a draw pump, a resistive load, and a flush valve. The complete analog circuit can be connected to the power plant, or if desired some other 4-port equivalent circuit can be used.

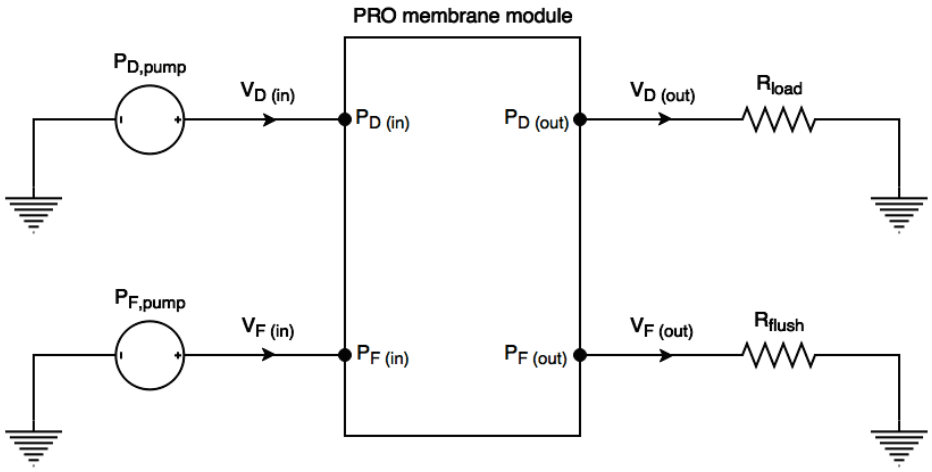

Figure 40. Analog circuit for a simplified osmotic power plant

This osmotic power plant includes several simplifications as compared to the more detailed schematic from Figure 17. For example, the pressure exchanger and filters are omitted. This simplified system however provides a satisfactory first approximation of the fundamental dynamics of an osmotic power plant. The analogous circuit of this simplified osmotic power plant can be used to analyze the system's dynamic response to variations in load and source. It can also be used to develop preliminary control strategies, and maximum power tracking strategies. Each of these applications is considered here.

4.6. Control of Operating Conditions

Efficiency of the PRO process and of the whole power plant is influenced by operating conditions, including feed and draw flow rates and hydraulic pressure difference. These are conditions that can be controlled. Generally operation objectives are expressed by the following three ratios:

$$\alpha = \frac{\dot{V}_P}{\dot{V}_{F(in)}} \tag{76}$$

$$\beta = \frac{\dot{V}_{D(in)}}{\dot{V}_{F(in)}} \tag{77}$$

$$\gamma = \frac{\Delta P}{\Delta \Gamma_m} \tag{78}$$

α is the ratio of permeate flow rate to the inlet feed flow rate. β is the ratio of draw flow rate to inlet feed flow rate. γ is the ratio of hydraulic pressure difference to osmotic pressure difference across the membrane. By observation the following limits can be imposed:

$$0 < \alpha \leq 1$$

$$\beta > 0$$

$$0 < \gamma < 1$$

Different combinations of these operation objectives can be achieved by coordinated control of these three parameters: (1) pressure across the feed pump $P_{F,pump}$, (2) pressure

across the draw pump $P_{D,pump}$, and (3) one of either load resistance R_{load}, or flush valve resistance R_{flush}. Using a flush valve allows operation objectives to be achieved independently of load and therefore provides greater flexibility. On the other hand, the pressure drop across the flush valve is in fact a parasitic load and reduces overall efficiency of the plant. Both load control and flush valve control are considered here.

The control signal for each of these three parameters can be obtained in terms of either water permeate flow rate $\dot{V}_P$ or in terms of osmotic pressure difference $\Delta\Gamma_m$. Writing the transfer functions in terms of water permeate flow rate is convenient for real time system operation because water permeate can easily be measured at the membrane outlet. Writing the transfer functions in terms of osmotic pressure can be convenient for simple approximations where some value of osmotic pressure is assumed based on bulk concentration difference for example.

The necessary control transfer functions can be determined by considering an equivalent 4-port voltage source or current source, as shown in Figure 41. Cross-flow resistance along the length of the membrane R_{drop} is divided into two parts, one on each side of the source. This assumes that pressure drop is distributed linearly along the length of the membrane. In reality the pressure drop is non-linear, however this simplification provides a satisfactory approximation.

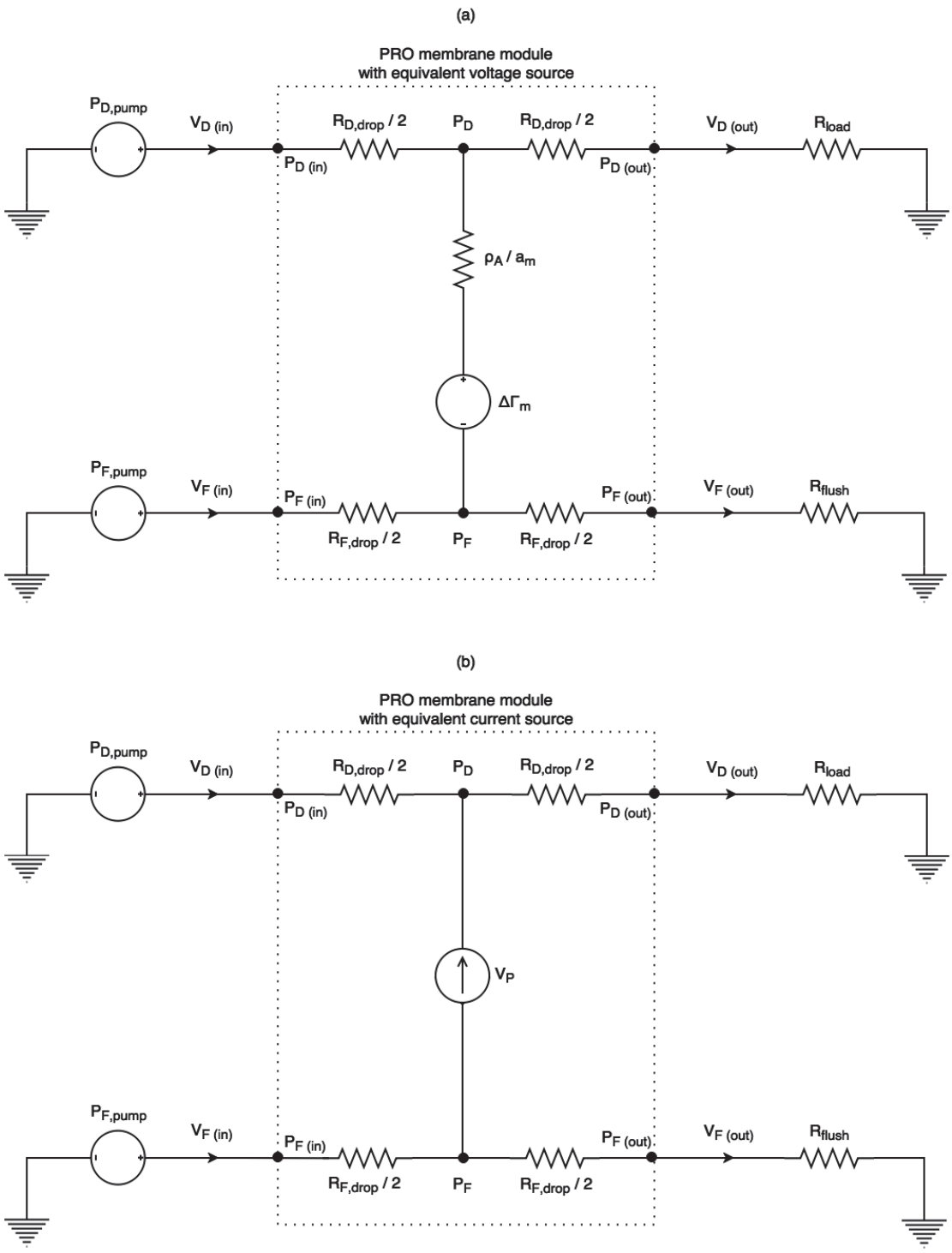

Figure 41. 4-port equivalent (a) voltage source and (b) current source connected to simplified osmotic power plant

Consider the expressions for feed and draw flow rates at both the membrane inlets and outlets:

$$\dot{V}_{F_{(in)}} = \frac{P_{F,pump} - P_F}{R_{F,drop}/2} \tag{79}$$

$$\dot{V}_{F_{(out)}} = \frac{P_F}{R_{F,drop}/2 + R_{flush}} \tag{80}$$

$$\dot{V}_{D_{(in)}} = \frac{P_{D,pump} - P_D}{R_{D,drop}/2} \tag{81}$$

$$\dot{V}_{D_{(out)}} = \frac{P_D}{R_{D,drop}/2 + R_{load}} \tag{82}$$

These feed and draw flow rates can also be written in terms of water permeate flow rate:

$$\dot{V}_{F_{(in)}} = \frac{1}{\alpha} \cdot \dot{V}_P \tag{83}$$

$$\dot{V}_{F_{(out)}} = \left(\frac{1}{\alpha} - 1\right) \cdot \dot{V}_P \tag{84}$$

$$\dot{V}_{D_{(in)}} = \frac{\beta}{\alpha} \cdot \dot{V}_P \tag{85}$$

$$\dot{V}_{D_{(out)}} = \left(\frac{\beta}{\alpha} + 1\right) \cdot \dot{V}_P \tag{86}$$

Combining equations (79) - (82) with equations (83) - (86), and solving gives the transfer functions. Equation (87) can be used to express the transfer functions in terms of either water permeate flow rate or osmotic pressure difference. Transfer functions are expressed here in terms of water permeate flow rate.

$$\frac{\dot{\dot{V}}_P}{\Delta\Gamma_m} = \frac{1-\gamma}{\rho_A/a_m} \tag{87}$$

During load control, the flush valve is removed and hence its resistance is shorted $R_{flush} = 0$. The transfer functions for load control are:

$$\frac{P_{F,pump}}{\dot{V}_P} = \left(\frac{2}{\alpha} - 1\right) \cdot \frac{R_{F,drop}}{2} \tag{88}$$

$$\frac{P_{D,pump}}{\dot{V}_P} = \frac{\beta}{\alpha} \cdot \frac{R_{D,drop}}{2} + \left(\frac{1}{\alpha} - 1\right) \cdot \frac{R_{F,drop}}{2} + \frac{\gamma}{(1-\gamma)} \cdot \frac{\rho_A}{a_m} \tag{89}$$

$$R_{load} = \frac{\frac{1}{\alpha} - 1}{\frac{\beta}{\alpha} + 1} \cdot \frac{R_{F,drop}}{2} + \frac{\gamma}{\left(\frac{\beta}{\alpha} + 1\right) \cdot (1-\gamma)} \cdot \frac{\rho_A}{a_m} - \frac{R_{D,drop}}{2} \tag{90}$$

During flush valve control, the load resistance R_{load} is not controlled. The transfer functions for flush valve control are given by:

$$\frac{P_{F,pump}}{\dot{V}_P} = \frac{1}{\alpha} \cdot \frac{R_{F,drop}}{2} + \left(\frac{\beta}{\alpha} + 1\right) \cdot \left(R_{load} + \frac{R_{D,drop}}{2}\right) - \frac{\gamma}{1-\gamma} \cdot \frac{\rho_A}{a_m} \tag{91}$$

$$\frac{P_{D,pump}}{\dot{V}_P} = \left(2 \cdot \frac{\beta}{\alpha} + 1\right) \cdot \frac{R_{D,drop}}{2} + \left(\frac{\beta}{\alpha} + 1\right) \cdot R_{load} \tag{92}$$

$$R_{flush} = \frac{\frac{\beta}{\alpha} + 1}{\frac{1}{\alpha} - 1} \cdot \left(R_{load} + \frac{R_{D,drop}}{2}\right) - \frac{\gamma}{\left(\frac{1}{\alpha} - 1\right) \cdot (1-\gamma)} \cdot \frac{\rho_A}{a_m} - \frac{R_{F,drop}}{2} \tag{93}$$

Analysis of these functions reveals that the load resistance and flush valve resistance are constant and independent of the equivalent source. On the other hand, the feed pump pressure $P_{F,pump}$ and draw pump $P_{D,pump}$ pressure are source dependent. Figure 42

illustrates how water permeate flow rate can be measured at the membrane outlet and used together with the transfer functions to control the feed and draw pump pressures.

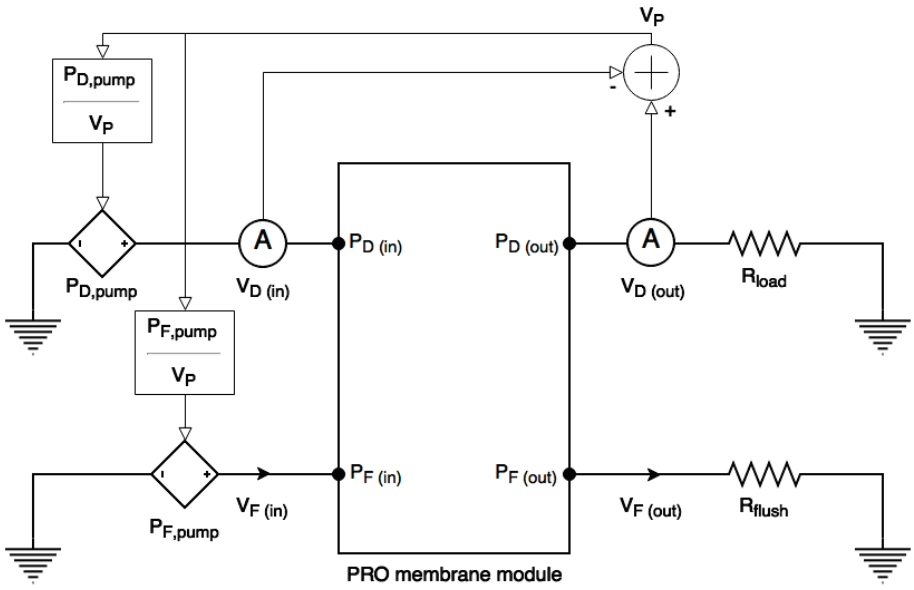

Figure 42. Osmotic power plant with controlled feed and draw pumps

Because these transfer functions are based on an equivalent source that is only an approximation of the actual membrane-based PRO process, there can be some discrepancy between the target operating conditions and the actual operating conditions. The effectiveness of the proposed control strategies can be evaluated by considering the ability of the system to track the target operating ratios. Two scenarios are considered, using the same parameters listed previously in Table 11. In each case, the membrane length is divided into n = 5 number of pieces, and the polarization layers are divided into m = 5 number of sections.

In the first scenario, there is a change in the source's draw concentration from $c_{D,b} = 30$ g/l to $c_{D,b} = 35$ g/l. Figure 43 shows the response of the system as both load control and flush valve control are used respectively to maintain the target operating ratios of $\alpha = 0.8$, $\beta = 1.6$ and $\gamma = 0.5$. During load control, the load resistance from equation (90) is $R_{load} = 1.67 \cdot 10^8$ Pa·s/m^3. During flush valve control, the flush valve resistance from equation (93) is $R_{flush} = 1.67 \cdot 10^8$ Pa·s/m^3 for the case where $R_{load} = 1.81 \cdot 10^8$ Pa·s/m^3.

In the second scenario, there is a change in the load from $R_{load} = 1.81 \cdot 10^8$ Pa·s/m^3 to $R_{load} = 3.61 \cdot 10^8$ Pa·s/m^3. Only flush valve control can be used in this case with variable loads. Target operating ratios are again $\alpha = 0.8$, $\beta = 1.6$ and $\gamma = 0.5$. Figure 44 shows the response of the system.

Both of the proposed control strategies show acceptable performance. Load control tracks the desired operating conditions with only a minor difference between the actual and target for α and β. It also allows the system to respond quickly to the step change in source concentration. Flush valve control shows even more impressive tracking of the operating conditions and allows the system to respond quickly to both source changes and load changes.

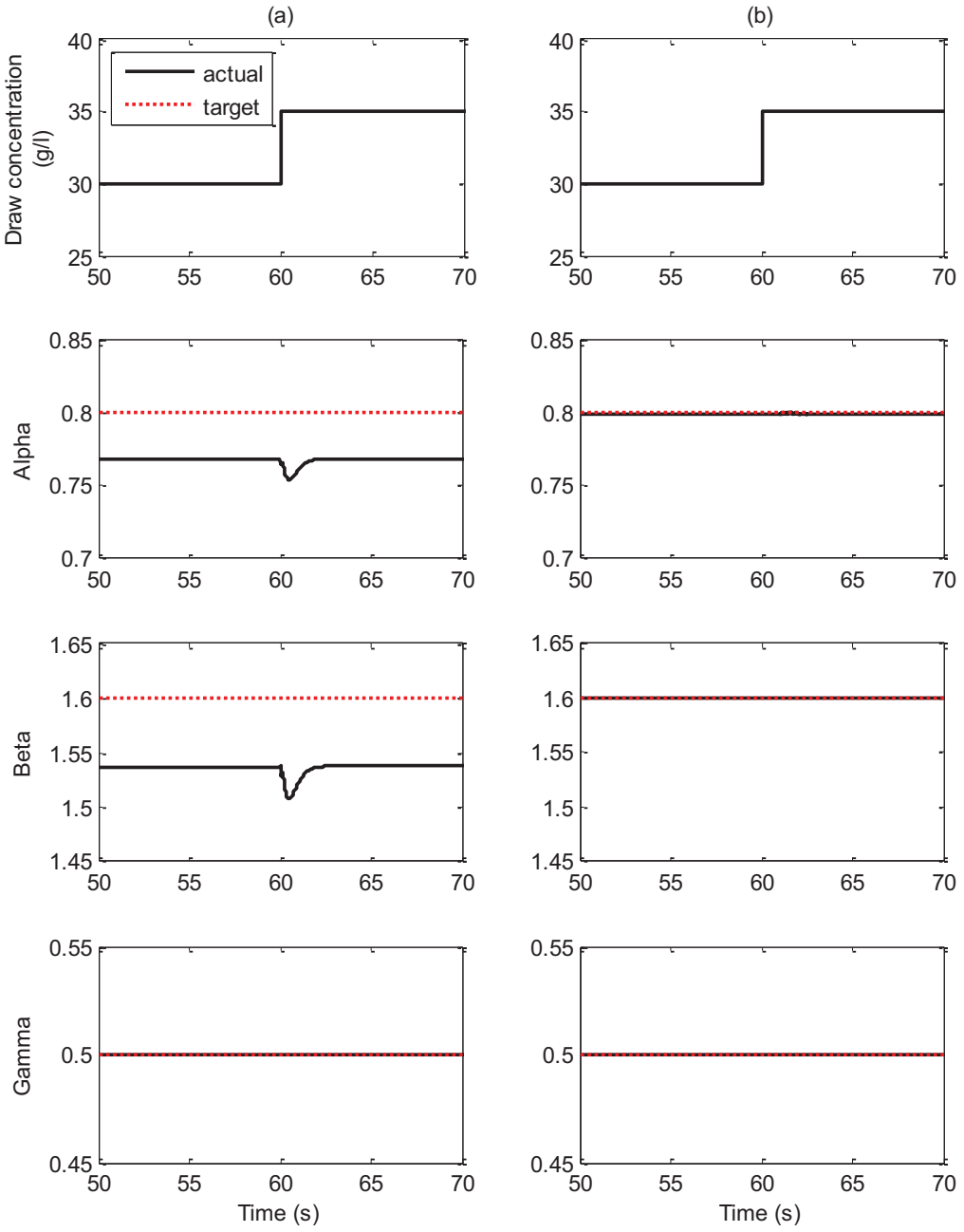

Figure 43. Real time operating ratios in response to an instantaneous change in draw concentration, when (a) the load control strategy is used and (b) the flush valve control strategy is used

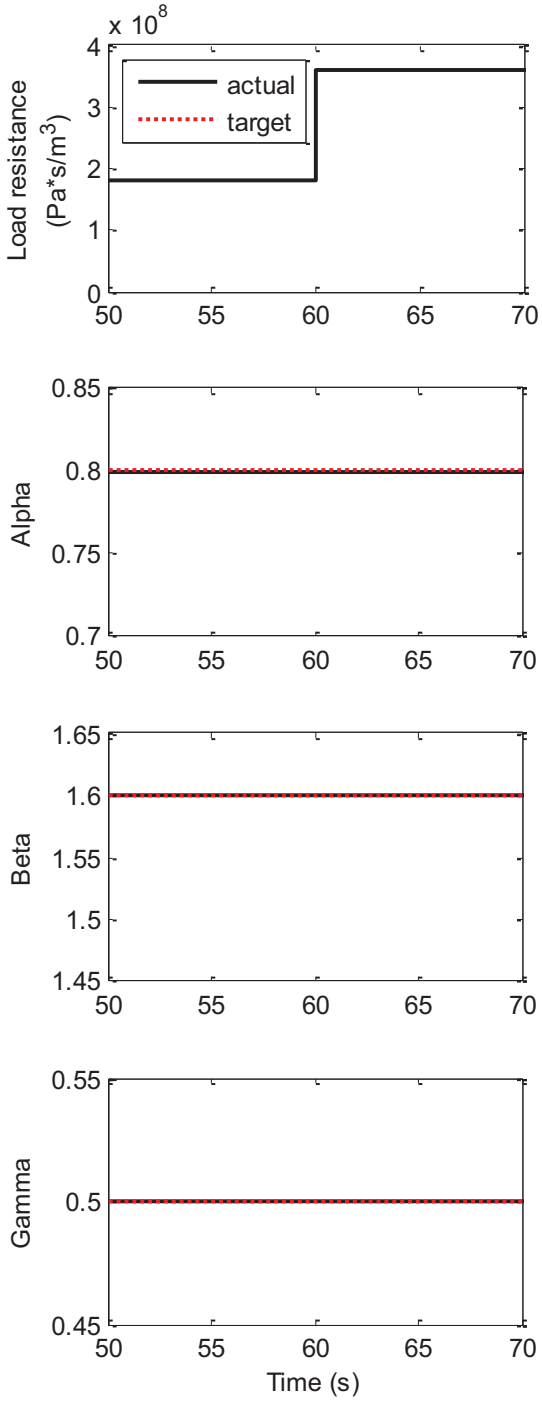

Figure 44. Real time operating ratios in response to an instantaneous change in load, when the flush valve control strategy is used

The primary limitation of these control strategies is that they are based on the simplified equivalent source block shown from Figure 41. In cases where the cross flow resistance becomes large, the non-linear variation in hydraulic pressure along the length of the membrane will become more pronounced and will further diverge more from the linear pressure drop that is assumed in the equivalent source block.

The practicality of these control strategies is also limited. They require data for the membrane resistance ρ_A / a_m and for the feed and draw side cross-flow resistances $R_{F,drop}$ and $R_{D,drop}$. This data may not be available and can vary under different conditions. Also, the ability of the strategies to track γ can be difficult to assess in practice because the effective osmotic pressure difference across the membrane $\Delta\Gamma_m$ cannot be measured directly.

4.7. Maximum Power Point Tracking

The proposed control strategies automatically maintain system operation at the desired conditions, even under variations in source and load. However they require that the operating targets be manually selected. As demonstrated in Chapters 2 and 3, the efficiencies for the PRO process and for the osmotic power plant are strongly influenced by the operating conditions. Certain rules of thumb have been suggested in the literature, such as $\alpha = 0.8$, $\beta = 1.6$ and $\gamma = 0.5$ [42], however these do not necessarily produce maximum power. A strategy for automatic tracking of the operating conditions that yield maximum power is proposed. Consider net power as the balance between power at the load and power at the membrane inlet:

$$W_{net} = W_{out} - W_{in} \tag{94}$$

$$W_{net} = \dot{V}_{D_{(out)}}{}^{2} \cdot R_{load} - \dot{V}_{F_{(in)}} \cdot P_{F,pump} - \dot{V}_{D_{(in)}} \cdot P_{D,pump} \tag{95}$$

Using the transfer functions, net power can be written as a function of operating conditions α, β, and γ. In the case where load control is used, net power can be expressed as:

$$\frac{W_{net}}{\dot{V}_P{}^{2}} = \frac{\rho_A}{a_m} \cdot \frac{\gamma}{1-\gamma} \tag{96}$$

$$-\frac{R_{F,drop}}{2} \cdot \left(1 - \frac{2}{\alpha} + \frac{2}{\alpha^2}\right)$$

$$-\frac{R_{D,drop}}{2} \cdot \left(\frac{2 \cdot \beta}{\alpha} + 1\right)$$

In the case where flush valve control is used, net power is given by:

$$\frac{W_{net}}{\dot{V}_P{}^{2}} = \frac{\rho_A}{a_m} \cdot \frac{\gamma}{1-\gamma} \cdot \frac{1}{\alpha} \tag{97}$$

$$+R_{load} \cdot \left(1 + \frac{\beta}{\alpha}\right) \cdot \left(1 - \frac{1}{\alpha}\right)$$

$$-\frac{R_{F,drop}}{2} \cdot \frac{1}{\alpha^2}$$

$$-\frac{R_{D,drop}}{2} \cdot \frac{1}{\alpha} \cdot \left(1 + \beta + \frac{\beta}{\alpha} + \frac{2 \cdot \beta^2}{\alpha}\right)$$

If the cross flow resistances are neglected $R_{drop} = 0$, then a simplified expression for net power in terms of osmotic pressure difference can be obtained, where equation (98) is for load control, and equation (99) is for flush valve control:

$$\frac{W_{net}}{\Delta\Gamma_m{}^2} = \frac{1}{\rho_A/a_m} \cdot \gamma \cdot (1-\gamma) \tag{98}$$

$$\frac{W_{net}}{\Delta\Gamma_m{}^2} = \frac{1}{\rho_A/a_m} \cdot \gamma \cdot (1-\gamma) \cdot \left[\frac{1}{\alpha} - \frac{R_{load}}{\rho_A/a_m} \cdot \frac{1-\gamma}{\gamma} \cdot \left(1+\frac{\beta}{\alpha}\right) \cdot \left(\frac{1}{\alpha}-1\right)\right] \tag{99}$$

Analysis of equation (98) shows that maximum power for load control is obtained when $\gamma = 0.5$, giving:

$$\frac{W_{max}}{a_m} = 0.25 \cdot A \cdot \Delta\Gamma_m{}^2 \tag{100}$$

This is the same expression for theoretical maximum PRO power that was derived previously in equation (11).

Comparison of equations (98) and (99) confirm that net power will be lower for flush valve control than for load control.

Using equation (96) for load control and equation (97) for flush valve control, it is possible to sweep through a range of combinations for α, β and γ in order to identify the maximum power point for a given water permeate flow rate. These operating conditions can be used as inputs to the previously defined transfer functions for pump and resistance controls. The maximum power point tracking strategy is illustrated in Figure 45.

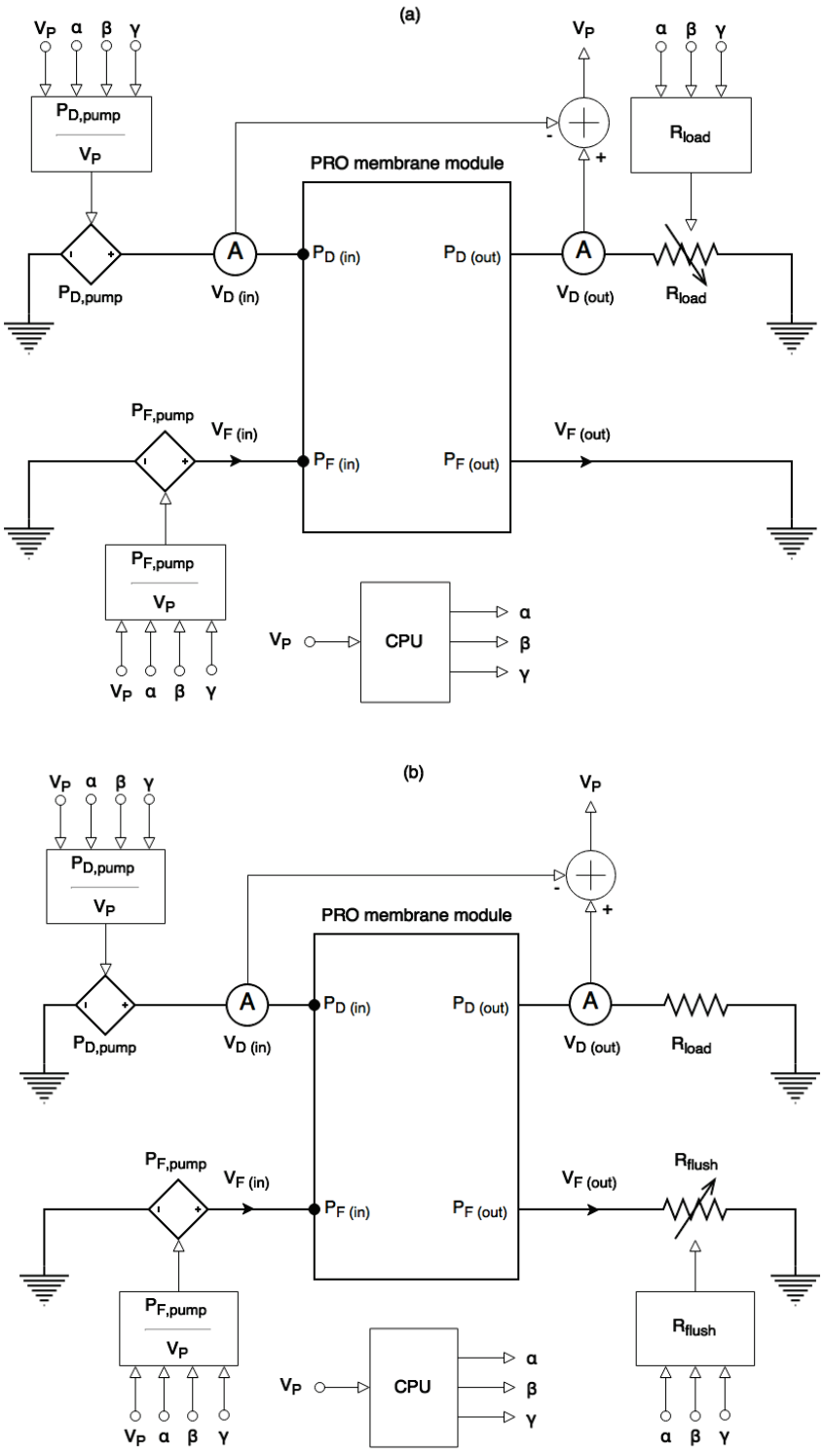

Figure 45. Osmotic power plant with operating conditions controlled at the maximum power point for (a) load control and (b) flush valve control

4.8. Summary

An analog electric circuit is developed for the PRO process, including consideration for concentration polarization, spatial variations along the length of the membrane and pressure drop along the membrane. The salt storage capacity of water is also included to model the dynamic behavior of salt flux. The analog circuit is validated against the previously validated mathematical model.

Using a simplified osmotic power plant and equivalent PRO source, strategies are developed for the control of operating conditions. Transfer functions are defined for load control and for flush valve control. These strategies successfully track the desired operating conditions, even under variations in the load and source. The same transfer functions are used to define an expression for power as a function of operating conditions. Using this expression, a mathematical model can be used to determine operating conditions that yield maximum power and this can be used together with the control strategies for maximum power point tracking.

5. OSMOTIC POWER FOR REMOTE COMMUNITIES IN QUEBEC

5.1. Introduction

Although most of Quebec is supplied by a well-developed hydro-electric network, there are 30 remote communities that rely on locally supplied micro-grids. There are 22 micro-grids in all throughout the province (19 diesel-powered, 2 hydro-powered and 1 powered by fuel oil). While the main grid supplies electricity at prices between 0.05-0.10 $/kWh, in certain micro-grids rates reach over 1.00 $/kWh [29]. Also, the diesel-generated electricity has a much larger carbon footprint and local emissions reduce air quality.

For these reasons there is interest in developing cleaner and less expensive renewable energy systems for these remote communities. Plans have been announced to develop wind-diesel hybrid systems in several locations but these have yet to materialize [29]. Other studies have suggested the potential for hydrokinetic power [86]. Salinity gradient power offers another option with several advantages. One of the main advantages is its reliability. While variations in wind speed and to a lesser degree river speed are rapid and unpredictable, variations in concentration and temperature are minor and very gradual, generally occurring over the space of several days. Also based on preliminary estimates the land use footprint of PRO is comparable to solar, 6 times less than wind and 8 times less than hydroelectricity (with reservoirs) [28].

In this chapter, the osmotic power potential is evaluated for 10 sites located within close proximity to micro-grids. The potential for this power source to supply community loads

is evaluated. Also, the design process and specifications for an osmotic power plant prototype are given. This prototype may become the first of its kind in Quebec and North America.

5.2. Micro-Grids in Quebec

Quebec's 22 remote micro-grids are shown on the map in Figure 46. They are located mainly along the northern coastline of the province, in the Nunavik region. Others are found on the Îles-de-la-Madeleine and Île-d'Anticosti in the Gulf of Saint-Lawrence and in the Basse-Côte-Nord region. Grids in the Shefferville and Haute-Mauricie regions are unique in that they are land-locked. For the most part these regions are only accessible by airplane and therefore fuel supplies must be flown in.

Table 12 provides an overview of energy use for each of the micro-grids, showing the annual use, peak demand and average price of electricity [29, 30]. The 3 dominant grids are Lac-Robertson and Schefferville which are hydro-powered and Cap-aux-Meules which is powered by fuel oil. Among the diesel-powered grids, the largest loads are Kuujjuaq (annual load of 18.4 GWh and peak demand of 3.45 MW) and La Romaine (annual load of 13.1 GWh and peak demand of 3.23 MW). Akulivik, Aupaluk and Ivujivik have the highest electricity prices of 1.10, 1.19 and 1.32 $/kWh respectively. Equivalent CO_2 emissions for the diesel and fuel oil grids are also shown. Since an osmotic power plant produces no greenhouse gas emissions, using it to replace diesel-power would reduce the equivalent CO_2 emissions.

Figure 46. Remote micro-grids throughout Quebec

Table 12. Overview of remote micro-grids in Quebec [a]

	Electricity use (GWh/yr)[b]	Peak demand (MW)	Unit price ($/kWh)	Emissions (CO_2 tonne/yr)
Akulivik	3.3	0.65	1.10	1956
Aupaluk	1.6	0.33	1.19	842
Cap-aux-Meules	186.7	41.80	0.34	126290
Clova	0.8	0.23	0.62	583
L'Île-d'Entrée	1.0	0.26	0.34	748
Inukjuaq	9.2	1.60	0.78	5890
Ivujivik	2.1	0.39	1.32	1229
Kangiqsualujjuaq	4.4	0.90	0.79	2907
Kangiqsujuaq	4.0	0.74	0.85	2579
Kangirsuk	3.4	0.68	0.79	2300
Kuujjuaq	18.4	3.45	0.86	12047
Kuujjuarapik	11.0	2.01	0.70	7412
Lac-Robertson	69.1	17.59	0.41	-
Opitciwan	11.1	3.01	0.49	8126
Port-Menier	4.2	1.12	0.74	3169
Puvirnituq	10.2	1.85	0.66	6154
Quaqtaq	2.4	0.51	0.95	1480
La Romaine	13.1	3.23	0.42	9375
Salluit	7.3	1.36	0.65	4569
Schefferville	43.4	10.40	0.35	-
Tasiujaq	2.3	0.48	0.91	1561
Umiujaq	2.7	0.53	0.96	1565

a. Source: [29, 30]

b. In most cases, electricity is not used for space or water heating

5.3. Freshwater and Seawater Resources in Remote Regions of Quebec

Most of the communities in question are located in the Nunavik and Basse-Côte-Nord regions. These are regions that have significant freshwater and seawater resources. Seawater resources include the Hudson Bay (average temperature T = 0 °C and concentration c = 30 g/l), the Ungava Bay (average T = 1 °C and c = 32 g/l) and the Gulf of Saint-Lawrence (average T = 0 °C and c = 32 g/l) [87, 88, 89]. In each case a moderate seasonal variation in temperatures and concentrations can be observed. Consider for example the Ungava Bay at a depth of 50 m, near the community of Kuujjuaq. As shown in Figure 47, temperature varies ± 0.5 °C with a peak in the fall, and concentration varies ± 1 g/l with a peak in the spring.

Figure 47 also shows the impressive seasonal variation in flow rates of the Koksoak River, also near the community of Kuujjuaq. This variation is a function of the freeze/thaw cycle and is characteristic of northern rivers throughout Quebec. In addition to these seasonal changes, daily variations in flow rates can be observed at up to 50 km inland of the Ungava Bay due to very strong tides. These tides cause additional variations in river concentration. For the sake of the present study tidal variations are ignored. In reality however, the influence of tides will reduce the concentration gradient at the estuary and may require moving water over large distances, which increases capital expenses and pumping losses.

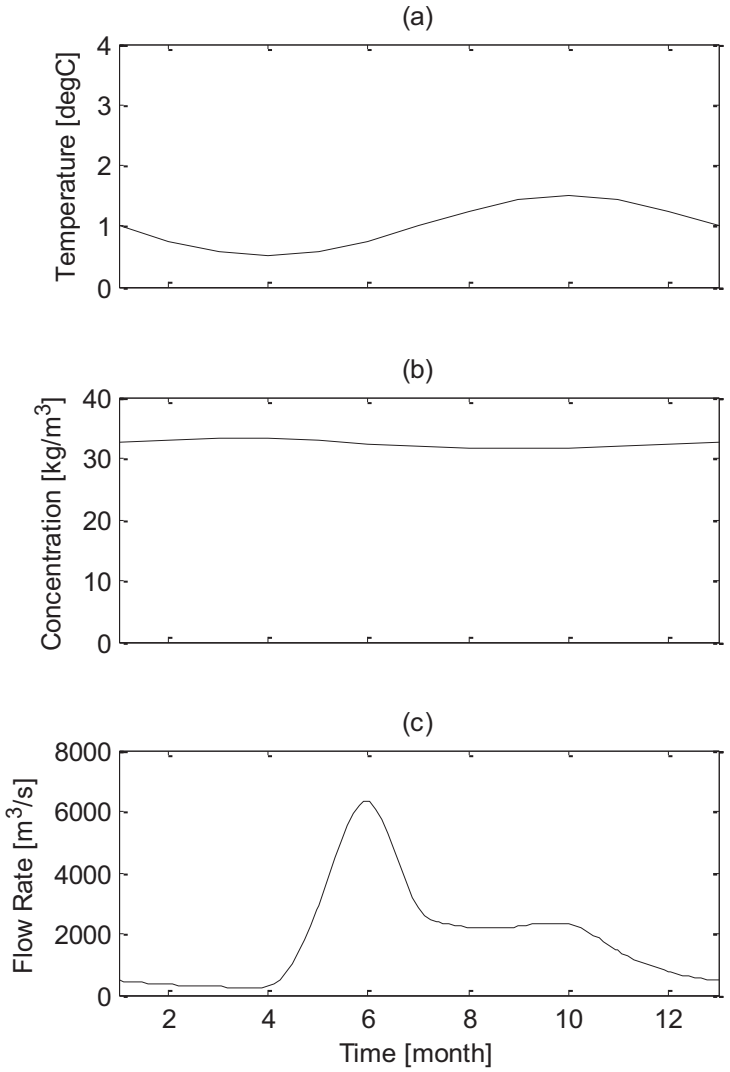

Figure 47. Variation in (a) temperature of the Ungava Bay, (b) concentration of the Ungava Bay and (c) flow of the Koksoaq river throughout the year

Historical flow rate data for Quebec rivers is available from [90] and [91]. The average monthly flow rates for the last 5 years available in the database were used to evaluate the power potential of each river. The period over which data was used for each river is specified together with the energy potential results, in Section 5.4.

5.4. Power Potential of Selected Rivers

The PRO power potential of a given site is evaluated by using the osmotic power plant model described previously in Figure 19. The membrane parameters and equipment specifications that are used are summarized in Table 13. These are optimistic values, using the target membrane parameters, neglecting filtration and pick-up head, and using relatively high equipment efficiencies. For simplicity, the rule of thumb ratios are used to set operating conditions $\dot{V}_P / \dot{V}_F = 0.8$, $\dot{V}_D / \dot{V}_F = 1.6$, and $\Delta P = \Delta\Gamma / 2$ [42].

Table 13. Osmotic power plant parameters used for evaluating potential power

Parameter	Value
Water permeability ($m^3/Pa \cdot s \cdot m^2$)	$10 \cdot 10^{-12}$
Salt permeability ($m^3/s \cdot m^2$)	$3 \cdot 10^{-8}$
Structure parameter (m)	$400 \cdot 10^{-6}$
Pressure exchanger efficiency (%)	97
Pump and motor efficiency (%)	77
Turbine and generator efficiency (%)	85
Pressure drop across filter	0
Pick-up head	0

The performance of the system will of course vary from site to site and throughout the year as site conditions change, but when Δc_b = 30 g/l and T = 0 °C, simulation results

show that the net electric power density is w_{net}^{e} = 1.53 W/m^2 and the power efficiency of the osmotic plant ia η_{plant} = 15 %. Another useful representation of system performance is obtained by normalizing power over the feed flow rate. Generally, when a river is flowing into the ocean, the limiting resource is the volume of freshwater relative to the enormous volume of seawater. Considering energy per unit freshwater gives a measure of how well this finite resource is used. The net energy harnessed in this scenario is $W_{net}^{e}/\dot{V}_F(x = 0)$ = 0.18 kWh/m^3. This is equivalent to 27 % of the total free energy released under these conditions.

The power potential of 10 rivers that are near to remote micro-grids is evaluated. These are the same 10 rivers labelled on the map in Figure 46. They are located in the Nunavik region with the exception of the Oloman River which is located in the Basse-Côte-Nord region. The simulation results for the 10 selected rivers are given in Figure 48. Net electric power is plotted as a function of the temporal variations in concentration, temperature and flow rate. The rivers are ranked in order of their peak power potential, which is labelled along with the minimum power potential. The large variation in power is striking and is due primarily to the freeze/thaw seasonal cycle of flow rates. To a much lesser extent some variation in power density is caused by changes in concentration and temperature.

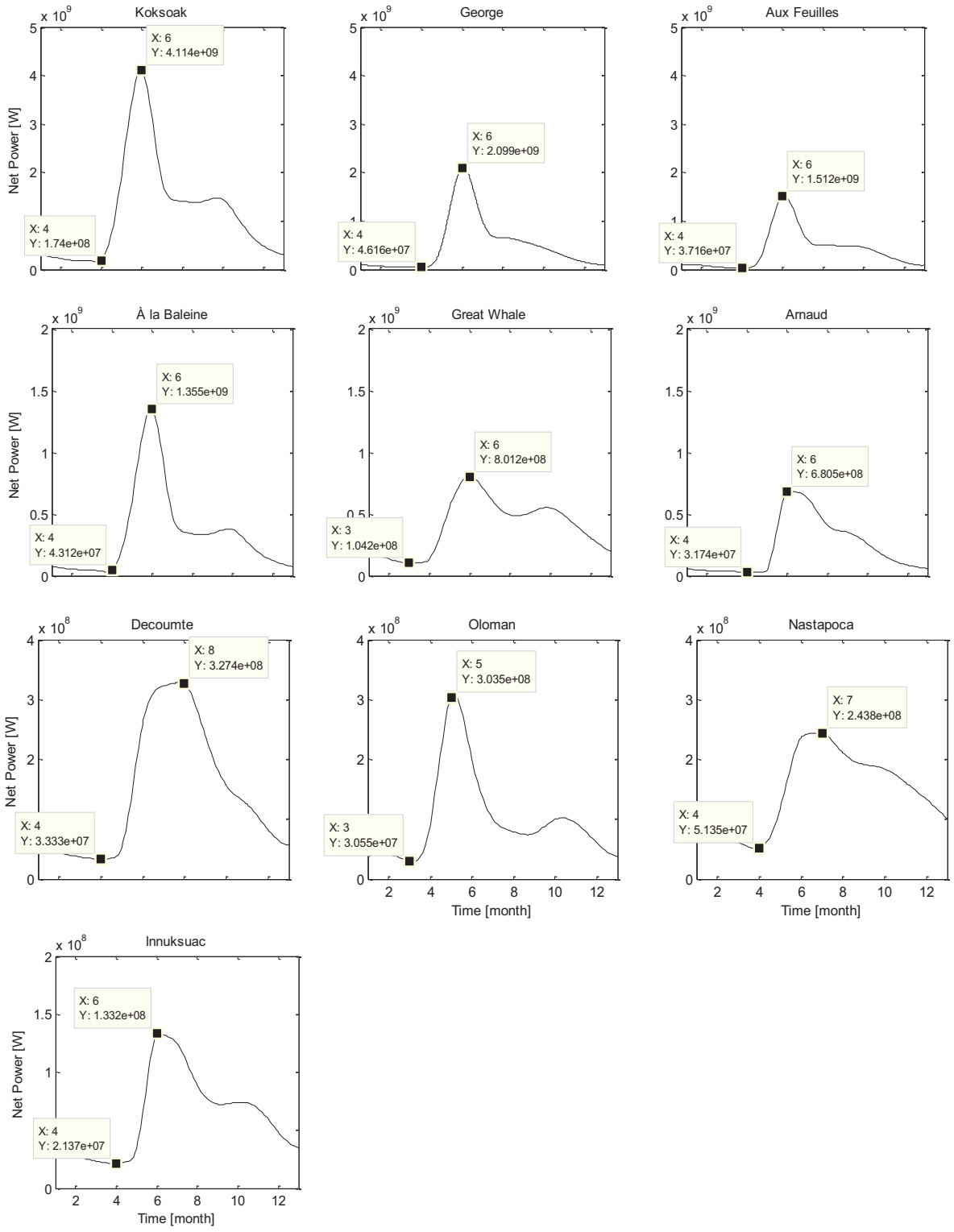

Figure 48. Net electric power W^{e}_{net} potential of selected rivers

The river with the greatest net electric power potential is the Koksoak, with a maximum of 4.114 GW and a minimum of 174 MW. The river with the lowest power potential is the Innuksuac, with a maximum of 133 MW and a minimum of 21 MW. The combined average power potential of the 10 rivers is equal to 3.5 GW.

Integrating below the power curves gives the total annual energy potential of each river. These annual energy results are listed in Table 14 for each river with their nearby community. Note that both the Koksoak and À la Baleine rivers are near to the same community of Kuujjuaq. Table 14 also specifies the period over which the average monthly river flow rates were obtained (5 most recent years available in the database).

These results show the enormous osmotic power potential of the sites. They also suggest a possible challenge with very large variations in power potential caused by river flow rates. Dealing with these variations is an important question whether PRO power is considered as a hybrid option (used only to supply base load) or as a stand-alone option (used to supply base load and peak demand). To evaluate the significance of this possible challenge, a ratio of the micro-grid's peak power demand versus the source's minimum monthly power potential is taken. This is equivalent to the percentage of the river's minimum monthly flow that would be required to supply peak loads.

Table 14. Osmotic energy potential versus community energy demand

River (Nearby community)	Net PRO energy potential (TWh/year) (period)	Peak load / Min. monthly power potential (%)	Peak load / Power potential under drought conditions (%) (year)
À la Baleine (Kuujjuaq)	2.991 (2009-2013)	7.2	31.7 (1967)
Arnaud (Kangirsuk)	2.039 (1979-1983)	2.2	3.1 (1970)
Aux Feuilles (Tasiujaq)	3.484 (1984-1988)	1.0	3.2 (1966)
Decoumte (Puvirnituq)	0.970 (1975-1979)	4.8	5.7 (1978)
George (Kansiqsualu-jjuaq)	4.399 (1975-1979)	1.7	2.8 (1975)
Grande Baleine (Kuujjuara-parik)	3.565 (1965-1969)	1.6	2.1 (1969)
Innuksuac (Inukjuak)	0.551 (1980-1984)	7.1	10.9 (1978)
Koksoak (Kuujjuaq)	10.545 (2007-2011)	1.8	2.2 (1989)
Nastapoca (Umiujaq)	1.293 (1989-1993)	0.8	1.1 (1975)
Oloman (La Romaine)	0.889 (1984-1988)	10.3	26.2 (1987)

The small percentages of flow required to meet peak load are well below the recommended ecological flow of 25% of lowest multiannual monthly flow [31]. This

suggests that osmotic power for such applications would have only minimal environmental impact and that such small diversions would be less likely to significantly change river and estuary ecosystems.

Using such a small portion of the river flow would also act as a buffer against large seasonal variations in river flow. These variations would not be felt by the osmotic power plant because the diverted portion of river flow would constantly be available. Osmotic power could therefore serve as a reliable and predictable power source for these remote micro-grids

To further illustrate, Table 14 also compares peak power demand against the power potential of the lowest monthly flow rate on record. Even under these extreme drought conditions, in most cases less than 25% of river flow would suffice to satisfy peak power demand. The only exceptions are for the Oloman River which is just slightly above 25 % (at 26.2 %) and for the À la Baleine River (31.7 %), however in the latter case the Koksoaq River which is also near the community of Kuujjuaq could be used, consuming only 2.2% of the drought flow rate. In other words, even under the most extreme drought conditions on record, the critical ecological flow of the rivers could be respected, while meeting peak power demand.

Another important consideration with respect to river flow is that climate change may lead to significant changes in future river dynamics. Although a detailed study of predicted river flows based on climate change models is required, it is interesting to note that for each river the average annual flow rate over the 5 most recent years available in

the database is between 0 and 10% greater than the average annual flow rate over the entire data record. This is no guarantee however that climate change will not result in more severe future impacts.

The results suggest that communities would require only a small percentage of the river's minimum monthly flow (most of them less than 5%) in order to satisfy peak demand. This means that osmotic power has the potential to serve as either a hybrid source or as a stand-alone source. In the first case it could serve as a steady source of power for base load. The designed power plant could operate at full load to thereby reduce the cost of energy. Alternatively, as a stand-alone source, it could serve as a controllable source of power for supplying peak demand. In this case modular membrane units could be brought online to increase power output when desired.

Standard hydraulic turbines can be used as the prime-mover of the PRO power system. Based on the expected hydraulic pressure and flow rates required for meeting power demand in these remote communities it is anticipated that the Francis turbine will generally be most appropriate however for communities with very low peak power demand (less than 0.6 MW) the Pelton turbine may be more suitable [92]. Most of the communities are currently fed by diesel engines which drive synchronous machines therefore it is likely that permanent magnet synchronous generators will be preferred for the osmotic power system. These offer the benefits of high power density, high efficiency and high performance [93].

5.5. Osmotic Power Plant Prototype for Quebec

In order to pursue the development of this technology in Quebec, and to evaluate its potential for powering remote communities, a partnership between Hydro-Québec, H_2O Innovation and Concordia University was formed. The goal of the research and development group is to design and build an osmotic power plant prototype (OSMOP prototype) in Quebec. This may become the first such prototype in North America. Until now there are very few osmotic power prototypes throughout the world.

In 2009 the Norwegian power company Statkraft placed the first osmotic power plant prototype into operation [19]. The plant is located in Tofte, Norway and has a 10 kW design capacity based on its targeted membrane performance of 5 W/m^2. Until now it has been operated between 2 and 4 kW. The first generation membranes used in the system showed performances of 0.2 W/m^2, while latest generation membranes showed much better performances of 1 W/m^2. Additional tests on new membranes showed promising results of up to 3 W/m^2 [94].

Until recently Statkraft was developing plans for the construction of a 2 MW power plant, with operation scheduled for 2016. Necessary licenses were obtained for a site at Sunndalsora, Norway and preliminary design was completed in 2013 [95]. However, in December 2013 Statkraft announced the suspension of all research and development activities related to PRO power [96]. This decision was based on current prices of oil and electricity in Europe and on the time that is still required for PRO technology to become commercially feasible, which was judged too long for the company's interest.

Other research institutes and companies however have continued to pursue the technology's development and potential commercialization, for example the Mega-Ton Water System project sponsored by the Japanese government. This osmotic power prototype is integrated with a desalination plant, making use of the concentrated waste brine to produce electricity and thereby reduce the net power consumption of the desalination plant [97].

5.5.1. Design Procedure

Owing to the limited range of experience related to osmotic power development at the prototype or commercial scale, a methodology for the design and construction of osmotic power plants has yet to be proposed in the literature. A procedure for the preliminary design of osmotic power plants is suggested. This procedure is based on experience gained during the design of the OSMOP prototype and is described in Figure 49.

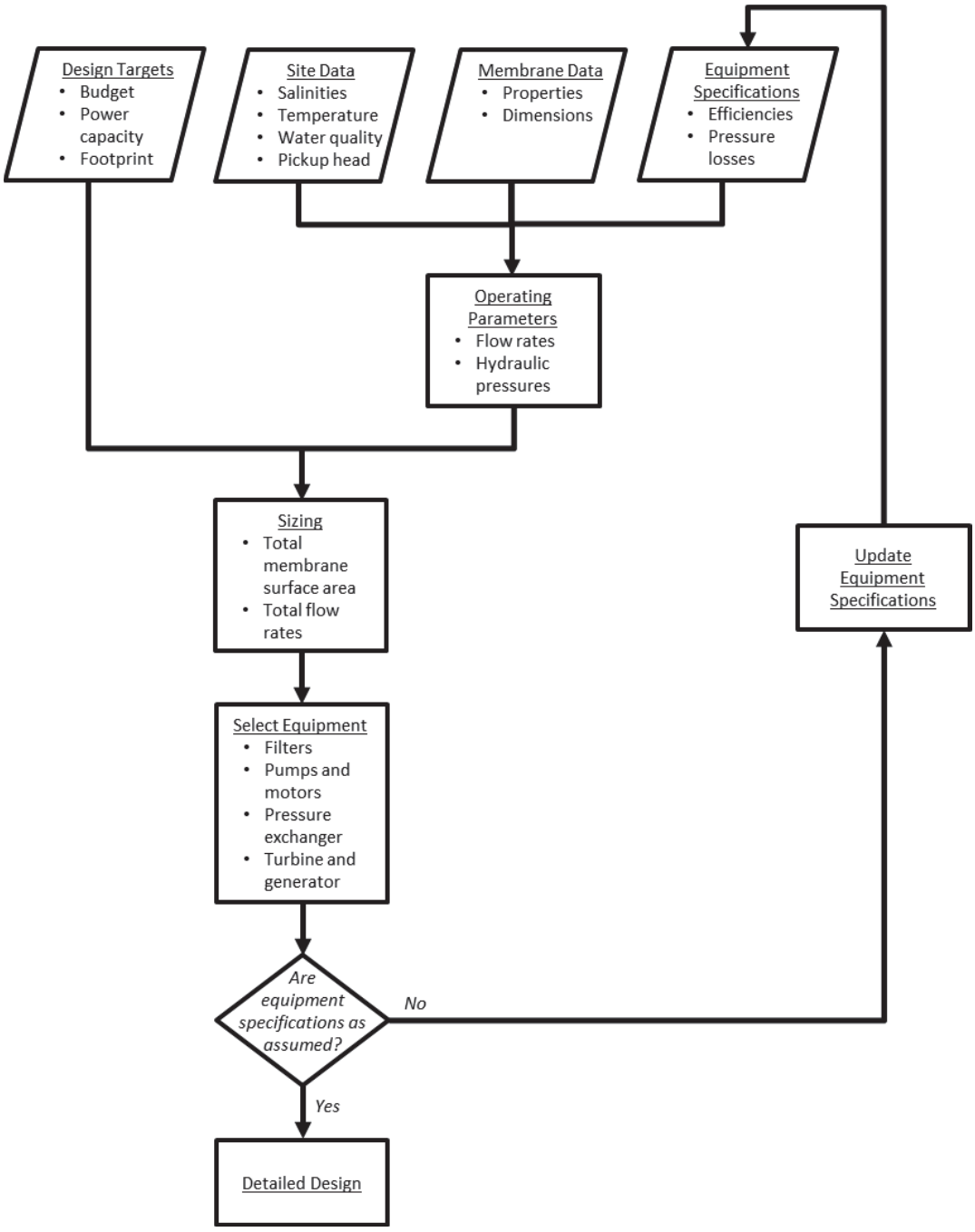

Figure 49. Procedure for the preliminary design of an osmotic power plant

This procedure requires input for the design targets, site conditions, and membrane specifications and an initial guess for equipment specifications. Design targets provide

the objectives and limits within which the system is developed. They can include power capacity or cost, for example. Given these limits the system can be designed to achieve minimum energy price or maximum efficiency. In the case of the OSMOP prototype the design targets include:

- The size of the prototype should be limited to a shipping container so as to allow it to be moved and installed at different sites
- The initial site should have access to existing infrastructure (roads, electricity, freshwater and seawater pumping capacity)
- The prototype should produce net power

Significant increases in power can be achieved by adjusting operating conditions. Identifying the best operating conditions however depends on equipment efficiencies and pressure losses throughout the system. Therefore an initial guess is made for equipment specifications and then updated in an iterative process as the design proceeds.

If several sites and membranes are being considered then the procedure is repeated for each of the scenarios.

5.5.2. Prototype Description

The basic configuration of the OSMOP power plant is provided in Figure 50**Erreur ! Source du renvoi introuvable.**. This is the same layout used in the Statkraft prototype [40, 41, 42]. Variations of this design have also been proposed elsewhere in the literature [98, 99]. In this prototype freshwater is supplied by an electric pump and is filtered across

carbon and cartridge filters before being introduced to one side of the membrane unit. Similarly, seawater is supplied by an electric pump and is filtered across sand and cartridge filters. Before being introduced to the membrane unit, it is pressurized through a pressure exchanger and electric boost pump. This establishes the desired hydraulic pressure difference across the membrane. At the membrane outlet, seawater flow is recirculated through the pressure exchanger while permeate flow is depressurized across a turbine and generator.

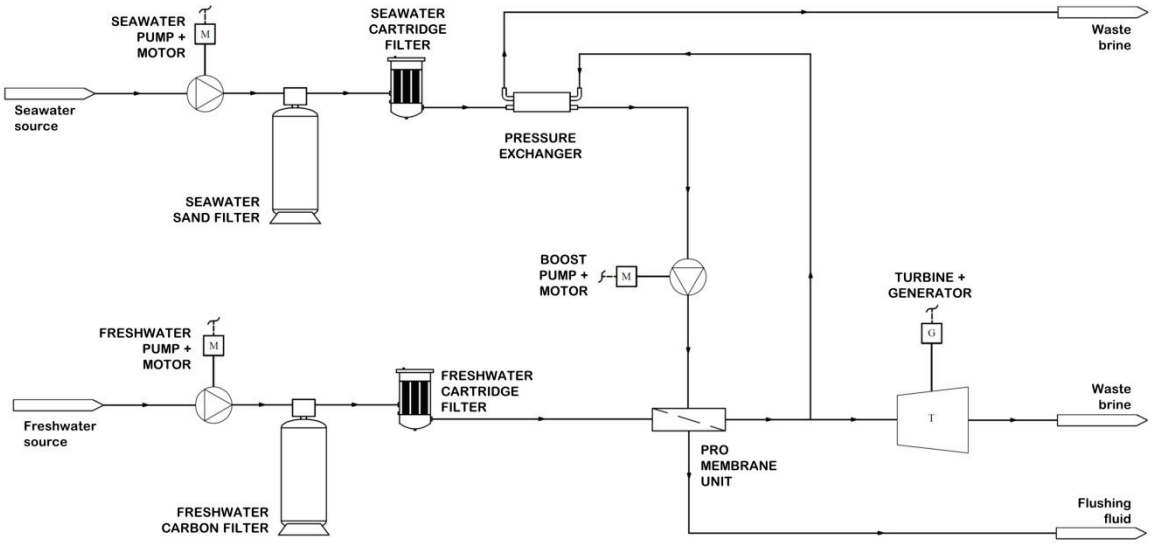

Figure 50. Schematic for osmotic power plant prototype

The PRO membrane is at the heart of the power plant. The commercial FO membrane that was tested in Chapter 2 is selected because of its promising performance in the laboratory. The membrane's characteristic properties are summarized in Table 15, along with the targets for PRO membrane research and development [42]. The commercial membrane has high water permeability which is desirable, but this is accompanied by

high salt permeability. The commercial membrane also has a very minimal structure parameter. It is important to minimize this in order to reduce concentration polarization.

Table 15. Membrane properties and dimensions

	Commercial membrane	Target membrane [42]
Water permeability ($m^3/Pa \cdot s \cdot m^2$)	$11.7 \cdot 10^{-12}$	$10.0 \cdot 10^{-12}$
Salt permeability ($m^3/s \cdot m^2$)	$0.40 \cdot 10^{-6}$	$0.03 \cdot 10^{-6}$
Structure parameter (m)	$267 \cdot 10^{-6}$	$400 \cdot 10^{-6}$
Membrane surface area (m^2)	888	
Length (m)	1.5	
Inner radius of hollow fiber (mm)	0.25	
Outer radius of hollow fiber (mm)	0.35	
Packing density (%)	50	

The primary mechanical and electrical components of the system include the pumps, motors, pressure exchanger, turbine, generator and filters. Efficiencies and pressure losses will vary as a function of operating conditions however their specifications under average conditions are summarized in Table 16.

Table 16. Equipment specifications

Component	Value
Pump and motor combined efficiency (%)	77
Pressure exchanger efficiency (%)	95
Turbine and generator combined efficiency (%)	85
Pressure drop on feed side filters (bar)	0.35
Pressure drop on draw side filters (bar)	0.35

5.5.3. Prototype Operation and Performance

The performance of an osmotic power plant is strongly influenced by the conditions under which it is operated [45, 46]. By adjusting operating flow rates and hydraulic pressures the non-ideal effects and pump loads can be minimized. Using the mathematical model from Figure 19, the best operating conditions for the prototype are determined and the results are summarized in Figure 51. These results assume that the prototype is installed in a northern region of Quebec, for example, in an environment similar to Kuujjuarapik where c_F = 0.1 g/l, c_D = 30 g/l, and T = 0 °C.

Figure 51 shows that peak net electric power output is achieved when the system is supplied with feed flow rate $\dot{V}_F$ = 0.0042 m^3/s and draw flow rate $\dot{V}_D$ = 0.0042 m^3/s, and with hydraulic pressure difference ΔP = 7.9 bar. The resulting net electric power density is w_{net}^{e} = 0.85 W/m^2.

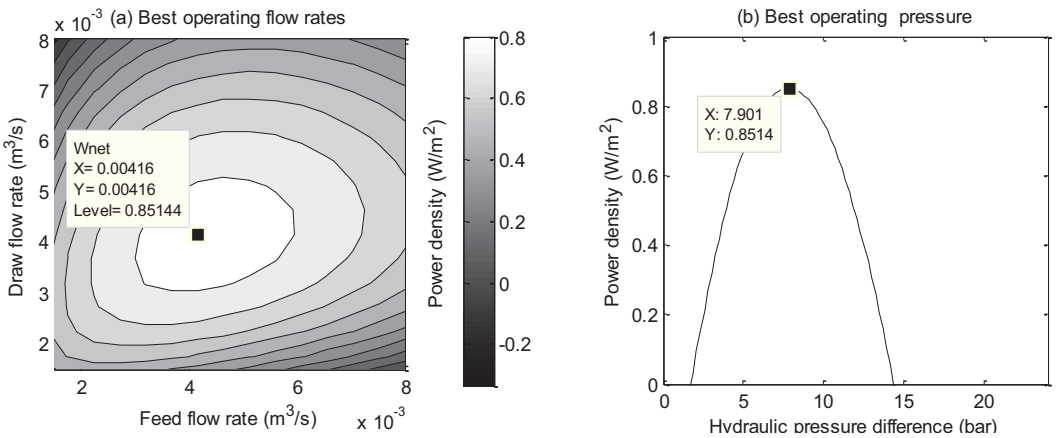

Figure 51. Operating flow rates $\dot{V}_F$ (x = 0) and $\dot{V}_D$ (x = 0) and hydraulic pressure difference $\overline{\Delta P}$ for achieving maximum net electric power density w_{net}^{e}

Table 17 provides a summary of the power flow throughout the system and shows where the majority of the losses occur. An impressive maximum power density of w_{max} = 15.74 W/m^2 is theoretically available from the PRO process under such conditions. Non-ideal membrane effects reduce the gross PRO power density $\hat{w}_{gross}^{PRO}$ = 1.84 W/m^2. Finally, mechanical and electrical inefficiencies and pump loads leave w_{net}^{e} = 0.85 W/m^2 of net electric power available for the grid. The efficiency of the power plant is η_{plant} = 5.4%. In terms of energy, 7.7% of the energy available in the salinity gradient is harvested. This is significantly less than the 48% system efficiency suggested by [56]. This discrepancy may be due to the prototype's use of small scale equipment which often has lower efficiency; however it also suggests the need for further investigation of osmotic power processes at the system scale.

Table 17. Prototype performance

	Power W (W)	Power density W / a_m (W/m^2)	Energy density $W / \dot{V}_F$ (kWh/m^3)
Maximum PRO	14 000	15.74	0.65
Gross PRO	1 630	1.84	0.11
Gross electric	1 400	1.56	0.09
Net electric	760	0.85	0.05

When comparing the performance of this system with other data in the literature it is important to note that most published results report gross PRO power only. Operating conditions can be selected so as to favour the gross PRO power; however such improvement can ultimately be detrimental to net electric power output. For example, in the case of this prototype, by adjusting operating conditions the gross PRO power can actually exceed the 5 W/m^2 target. The resulting net electric power however would be negative.

5.5.4. Case Study: Osmotic Power Plant Prototype for Kuujjuarapik

The potential to use osmotic power for electrification of remote micro-grids can be illustrated by considering a case study of the OSMOP prototype in the community of

Kuujjuarapik, which is located at the estuary between the Great Whale River and the Hudson Bay. The Kuujjuarapik grid is diesel powered. It has annual electricity consumption of 11 GWh and peak demand of 2 MW. Electricity is produced at a cost of 0.70 $/kWh and the related greenhouse gas emissions are on the order of 7400 equivalent CO_2 tonnes/year [29, 30]. The Great Whale River has an average discharge of 670 m^3/s and an average concentration and temperature of c_F = 0.1 g/l and T = 0 °C. The Hudson Bay has an average concentration and temperature of c_D = 30 g/l and T = 0 °C.

Assuming that the prototype's energy extraction efficiency (0.05 kWh/m^3) remains constant during scale-up, the energy that could be extracted from the total discharge of the Great Whale River is 1056 GWh/yr, as shown in **Erreur ! Source du renvoi introuvable.**. Only a small fraction of this potential would suffice to meet the energy needs of Kuujjuarapik. A feed flow rate of 11.1 m^3/s diverted from the river and supplied to a PRO power station equipped with $2.35 \cdot 10^6$ m^2 of membrane surface area would be able to meet peak power demand for the community. This represents less than 2% of the river's average flow rate, which is within the recommended limits for environmentally sustainable river use [31]. Assuming that capital costs are proportional to membrane surface area at a rate of 10 $\$/m^2$ and assuming a membrane life of 10 years [100], the electricity price of osmotic power in Kuujuarapik is projected at 0.13 $/kWh. This is much less than the current price of 0.70 $/kWh.

Table 18. Potential for osmotic power plant near the remote community of Kuujjuarapik

	Net power density (W/m^2)	Net energy density (kWh/m^3)	Source potential (GWh/yr)	Required membrane area (m^2)	Required flow rate (m^3/s)	Capital cost ($/W)	Electricity price ($/kWh)
Commercial membrane	0.85	0.05	1 056	$2.35 \cdot 10^6$	11.1	11.75	0.13
Target membrane	1.68	0.11	2 324	$1.19 \cdot 10^6$	5.6	5.95	0.07

It is also encouraging to consider the potential improvements that can be realized by advances in membrane technology. The performance of the prototype, equipped with the target membrane is illustrated in **Erreur ! Source du renvoi introuvable.**. In this case, power and energy extraction efficiencies are approximately double those of the commercially available membrane. The result is an electricity price of 0.07 $/kWh, which would be competitive not only in remote regions but throughout Quebec. It should be recognized however that these energy price estimates are based on several major assumptions.

5.6. Summary

The net power potential of 10 rivers in remote regions of Quebec is determined as a function of annual variations in temperature, concentration and river flow. It is determined that only a small percentage of even the minimum monthly power potential

can satisfy peak power demand for each of the river's corresponding nearby communities. This suggests that PRO power can be a reliable and predictable renewable energy source capable of meeting the base load as well as peak loads of the remote micro-grids.

The preliminary design is presented of an osmotic power plant prototype for Quebec. The procedure used for the design is explained and illustrated with data from the actual prototype design. The prototype has a net electric power capacity of 760 W and plant efficiency of 5.4 %. The prototype is being developed in partnership with Hydro-Québec and H_2O Innovation, and is now in the financing stages.

A case study of the prototype's performance in the community of Kuujjuarapik (Quebec) is presented. Using commercially available membrane technology, the cost of osmotic energy is estimated at 0.13 $/kWh, which is significantly lower than rates for current electricity from diesel generators. Niche markets such as these can provide the incentive for commercial development of osmotic power technology. Future membranes may reduce the price of osmotic power to 0.07 $/kWh, making it competitive not only in niche markets but also in mainstream power generation markets.

6. CONCLUSIONS AND RECOMMENDATIONS

6.1. Conclusions

Mathematical Model of PRO Power System

- Improving power production by PRO is a matter of reducing non-ideal effects around the semi-permeable membrane and throughout the power plant. Most research and development efforts have focused on improving membrane materials by optimizing the trade-off between permeability and selectivity. Another approach is to consider trade-offs in operating conditions that exits at the power plant scale.
- Non-ideal effects such as concentration polarization and spatial variations in concentration can be reduced with high cross-flow rates; however high flow rates lead to high pressure loss due to friction. It is possible to balance these non-ideal effects such that there overall effect on power is minimized.
- A detailed mathematical model of PRO power production is developed. The model considers:
  - Concentration polarization across the membrane support layer (internal concentration polarization)
  - Concentration polarization across the feed and draw side boundary layers (external concentration polarization)
  - Spatial variations along the length of the membrane due to water and salt flux

  - Pressure drop along the length of the membrane due to friction
  - Pressure drop from pre-filtration and pick-up head
  - Efficiency of mechanical and electrical equipment
- Using the mathematical model, the best operating conditions for several scenarios are identified. Best operating conditions are specific to the system being considered however they are not necessarily equal to the rule of thumb conditions that have been used in the literature.
- In general the best operating conditions will be along the following lines:
  - As the membrane permeability and selectivity improve, the best operating flow rates and hydraulic pressure difference will increase
  - As the length of the membrane is reduced, the best operating flow rates will increase
  - As the cross sectional area of the flow channel is increased, the best operating flow rates will increase
  - As equipment efficiencies are improved, the best operating flow rates and hydraulic pressure difference will increase

Experimental Investigation of PRO

- Experimentally observed PRO power densities have increased steadily in recent years. The target power density of 5 W/m^2 has now been surpassed in several laboratories.

- Laboratory tests are generally conducted under conditions that favor gross PRO power density but these conditions cause significant pressure drops that are often unreported and that result in low or even negative net power densities. These results therefore can be deceiving and will translate poorly to the commercial scale because the operating conditions will not be appropriate for industrial power applications.
- It is suggested that future laboratory tests be conducted under conditions that favor net power density as oppose to gross power density. Results obtained under these conditions will be more representative of expected performance at the commercial scale.
- An experimental investigation of PRO is conducted.
  - Gross PRO power density of 7.1 W/m^2 is obtained using a commercially available semi-permeable membrane under standard test conditions.
  - Net PRO power density of 4.5 W/m^2 is achieved when operating conditions are adjusted to minimize non-ideal effects.
  - Experimental results agree well with the simulation results for a range of operating flow rates and hydraulic pressure differences.

Analog Electric Circuit for PRO

- The flow of water across a semi-permeable membrane, driven by some pressure difference can be analogous to the flow of electric charge across a resistance, driven by some potential difference. A similar analogy can be made for the flow

of salt across a semi-permeable membrane, driven by some concentration difference. These analogies are used to develop an electric circuit that represents the PRO process.

- Simulation results generated from the analog circuit agree well with results from the validated mathematical model.
- The analog circuit is used to develop strategies for controlling operating conditions by either load control or flush valve control. Load control provides better overall efficiency but flush valve control allows the system to operate with variable loads. Both control strategies provide satisfactory tracking of the desired operating conditions.
- The analog circuit is used to develop a strategy for tracking the operating conditions that give the maximum power point.

Osmotic Power Potential in Remote Regions of Quebec

- Remote communities in Quebec are supplied electricity by local micro-grids, most of which are powered by diesel generators. The cost of transporting fuel to these locations is high, resulting in expensive energy prices. Environmental impacts of the current system include high greenhouse gas emissions and air pollution. Also, the reliance of these communities on a foreign energy source makes them vulnerable to disturbance. For all these reasons, there is interest in developing local and renewable energy alternatives.

- PRO power potential is evaluated for selected rivers in remote regions. It is found that only a small portion of river flow rates would be required to meet the peak power demand of communities. Using a small portion of river flow would mitigate environmental impacts and also insulate the power plant against strong seasonal variations in river flow rates.
- The preliminary design is presented for an osmotic power plant prototype for Quebec. The power plant has net electric power capacity of 760 W. Scaling up the prototype could achieve electricity prices of 0.13 $/kWh with commercially available membranes and 0.07 $/kWh with future improved membranes

6.2. Proposed Future Research

- Improvements in the mathematical model can be made by considering membrane distortion, membrane fouling, and by verifying the constants used in the expressions for mass transfer coefficient and friction factor.
- The analog circuit can be improved by addressing the major simplifications that were used in the model.
  - Mass transfer coefficients and salt diffusion coefficients were assumed constant and consequently gave some constant resistance to salt flux. These values should be calculated as functions of concentration and flow rate and modeled as variable resistance.

  - The pressure exchanger should be considered as part of the osmotic power plant. This is an important system component that has its own unique behavior.
  - The lack of any inductive behavior in the analog circuit is clearly a shortcoming of the model. Both pumps and pressure exchangers will exhibit a certain inertia or inductive behavior. The resistive load should be replaced with an inductive load to represent a hydro turbine which would be used as the prime mover in power production applications.
  - The analog circuit should be built and tested, either with hardware or in dSPACE.
- The OSMOP power plant prototype is now in the financing stages. Following this, future work should include detailed design, especially for the turbine and generator. Extensive testing should be done with the prototype to validate commercial scale PRO dynamics and power plant performance and operation.

6.3. Contributions

The following is the technical output of the presented research work in this thesis:

6.3.1. Journal Papers

1. J. Maisonneuve, P. Pillay, and C. B. Laflamme, “Pressure-Retarded Osmotic Power System Model Considering Non-Ideal Effects,” Renewable Energy, vol. 75, pp. 416-424, 2015.

2. M. F. Naguib, J. Maisonneuve, C. B. Laflamme, and P. Pillay, "Modeling Pressure-Retarded Osmotic Power in Commercial Length Membranes," Renewable Energy, vol. 76, pp. 619-627, 2015.
3. J. Maisonneuve, P. Pillay, and C. B. Laflamme, "Osmotic Power Potential in Remote Regions of Quebec," Renewable Energy, vol. 81, pp. 62-70, 2015.
4. J. Maisonneuve, C. B. Laflamme, and P. Pillay, "Experimental Investigation of Pressure Retarded Osmosis for Renewable Power Applications: Towards Improved Net Power Density," under review.
5. J. Maisonneuve and P. Pillay, "A Simplified Equivalent Circuit Model for Salinity Gradient Energy Conversion by Pressure Retarded Osmosis," in progress.

6.3.2. Conference Papers

1. J. Maisonneuve and P. Pillay, "Pressure-Retarded Osmotic Power for Remote Communities in Quebec," Power and Energy Society (PES) General Meeting, Washington, DC, USA, July 2014.
2. J. Maisonneuve and P. Pillay, "Osmotic Power Prototype for Generating Electricity and Reducing Greenhouse Gas Emissions in Remote Regions of Quebec," Engineering Institute of Canada (EIC) Climate Change Technology Conference (CCTC), Montreal, QC, Canada, May 2015.

REFERENCES

[1] M. I. Hoffert, K. Caldeira, G. Benford, D. R. Criswell, C. Green, H. Herzog, A. K. Jain, H. S. Kheshgi, K. S. Lackner, J. S. Lewis, H. D. Lightfoot, W. Manheimer, J. C. Mankins, M. E. Mauel, L. J. Perkins, M. E. Schlesinger, T. Volk and T. M. L. Wigley, "Advanced technology paths to global climate stability: Energy for a greenhouse planet," *Science,* vol. 298, pp. 981-987, 2002.

[2] R. E. Pattle, "Production of electric power by mixing fresh and salt water in hydroelectric pile," *Nature,* vol. 660, p. 174, 1954.

[3] G. L. Wick and W. R. Schmitt, "Prospects for renewable energy from the sea," *Marine Technology Journal,* vol. 11, pp. 16-21, 1977.

[4] J. W. Post, J. Veerman, H. M. V. Hamelers, G. J. W. Euverink, S. J. Metz, K. Nymeijer and C. J. N. Buisman, "Salinity-gradient power evaluation of pressure-retarded osmosis and reverse electrodialysis," *Journal of Membrane Science,* vol. 288, pp. 218-230, 2007.

[5] O. Levenspiel and N. de Nevers, "The osmotic pump," *Science,* vol. 183, pp. 157-160, 1974.

[6] J. N. Weinstein and F. B. Leitz, "Electric power from differences in salinity: The dialytic battery," *Science,* vol. 191, pp. 557-559, 1976.

[7] M. Olsson, G. L. Wick and J. D. Isaacs, "Salinity gradient power: Utilizing vapor pressure differences," *Science,* vol. 206, pp. 452-454, 1979.

[8] A. Daniilidis, D. A. Vermaas, R. Herber and K. Nijmeijer, "Experimentally obtainable energy from mixing river water, seawater or brines with reverse electrodialysis," *Renewable Energy,* vol. 64, pp. 123-131, 2014.

[9] B. E. Logan and M. Elimelech, "Membrane-based processes for sustainable power generation using water," *Nature,* vol. 488, pp. 313-319, 2012.

[10] A. Achilli and A. E. Childress, "Pressure retarded osmosis: From the vision of Sydney Loeb to the first experimental installation - Review," *Desalination,* vol. 261, pp. 205-211, 2010.

[11] F. Helfer, L. C. and Y. Anissimov, "Osmotic power with pressure retarded osmosis: Theory, performance and trends - A review," *Journal of Membrane Science,* vol. 2014, pp. 337-358, 2014.

[12] R. Norman, "Water salination: A source of energy," *Science,* Vols. 350-352, p. 186, 1974.

[13] S. Loeb and R. Norman, "Osmotic power plants," *Science,* vol. 189, pp. 654-655, 1975.

[14] S. Loeb, "Method and apparatus for generating power utilizing pressure-retarded osmosis". U.S. Patent 3,906,250, June 1971.

[15] S. Loeb, "Production of energy from concentrated brines by pressure-retarded osmosis: I. Preliminary technical and economic consideration," *Journal of Membrane Science,* vol. 1, pp. 49-63, 1976.

[16] S. Loeb, F. Van Hessen and D. Shahaf, "Production of energy from concentrated brines by pressure-retarded osmosis: II. Experimental results and projected energy costs," *Journal of Membrane Science,* vol. 1, pp. 249-269, 1976.

[17] S. Loeb, "Large-scale power production by pressure-retarded osmosis, using river water and sea water passing through spiral modules," *Desalination,* vol. 143, pp. 115-122, 2002.

[18] I. L. Alsvik and M. B. Hagg, "Pressure retarded osmosis and forward osmosis membranes: Materials and methods," *Polymers,* vol. 5, pp. 303-327, 2013.

[19] Statkraft, "The world's first osmotic power prototype opens today," November 2009. [Online]. Available: http://ww.statkraft.com/media/press-releases/press-releases-archive/2009/the-worlds-first-osmotic-power-prototype-opens-today. [Accessed May 2014].

[20] S. Loeb, "Energy production at the Dead Sea by pressure-retarded osmosis: Challenge or chimera?," *Desalination,* vol. 120, pp. 247-262, 1998.

[21] S. Loeb, "One hundred and thirty benign and renewable megawatts from the Great Salt Lake? The possibilities of hydroelectric power by pressure retarded osmosis," *Desalination,* vol. 141, pp. 85-91, 2001.

[22] R. L. McGinnis, J. R. McCutcheon and M. Elimelech, "A novel ammonia-carbon dioxide osmositc heat engine for power production," *Journal of Membrane Science,* vol. 305, pp. 13-19, 2007.

[23] W. He, Y. Wang and M. H. Shaheed, "Stand-alone seawater RO (reverse osmosis) desalination powered by PV (photovoltaic) and PRO (pressure retarded osmosis)," *Energy,* in press, 2015.

[24] D. D. Anastasio, J. T. Arena, E. A. Cole and J. R. McCutcheon, "Impact of temperature on power density in closed-loop pressure retarded osmosis for grid storage," *Journal of Membrane Science,* vol. 479, pp. 240-245, 2015.

[25] B. J. Feinberg, G. Z. Ramon and E. M. V. Hoek, "Thermodynamic analysis of osmotic energy recovery at a reverse osmosis desalinition plant," *Environmental Science & Technology,* vol. 47, pp. 2982-2989, 2013.

[26] J. L. Prante, J. A. Ruskowitz, A. E. Childress and A. Achilli, "RO-PRO desalination: An integrated low-energy approach to seawater desalination," *Applied Energy,* vol. 120, pp. 104-114, 2014.

[27] A. Achilli, J. L. Prante, N. T. Hancock, E. B. Maxwell and A. E. Childress, "Experimental results from RO-PRO: A next generation system for low-energy desalination," *Environmental Science & Technology,* vol. 48, pp. 6437-6443, 2014.

[28] C. B. Laflamme, "Challenges facing osmotic power in Canada," in *INES Meeting*, Netherlands, 2013.

[29] Hydro-Québec Distribution, "Plan d'approvisionnement 2014-2023 des réseaux autonome," Hydro-Québec, 2013.

[30] Hydro-Québec Distribution, "Plan d'approvisionnement 2011-2020 des réseaux autonome," Hydro-Québec, 2010.

[31] S. Ortega, P. Stenzel, O. Alvarez-Silva and A. F. Osorio, "Site-specific potential analysis for pressure retarded osmosis (PRO) power plants - The Léon River example," *Renewable Energy,* vol. 68, pp. 466-474, 2014.

[32] N. Y. Yip and M. Elimelech, "Performance limiting effects in power generation from salinity gradients by pressure-retarded osmosis," *Environmental Science & Technology,* vol. 45, pp. 10273-10282, 2011.

[33] J. G. Wijmans and R. W. Baker, "The solution-diffusion model: A review," *Journal of Membrane Science,* vol. 107, pp. 1-21, 1995.

[34] K. L. Lee, R. W. Baker and H. K. Lonsdale, "Membranes for power generation by pressure-retarded osmosis," *Journal of Membrane Science,* vol. 8, pp. 141-171., 1981.

[35] J. R. McCutcheon and M. Elimelech, "Modeling water flux in forward osmosis: Implications for improved membrane design," *American Institute of Chemical Engineers Journal,* vol. 53, pp. 1736-1744, 2007.

[36] S. Achilli, T. Y. Cath and A. E. Childress, "Power generation with pressure retarded osmosis: An experimental and theoretical investigation," *Journal of Membrane Science,* vol. 343, pp. 42-52, 2009.

[37] G. Z. Ramon, B. J. Feinberg and E. M. V. Hoek, "Membrane-based production of salinity-gradient power," *Energy & Environmental Science,* vol. 4, pp. 4423-4434, 2011.

[38] N. Y. Yip, A. Tiraferri, W. A. Phillip, J. D. Schiffman, L. A. Hoover, Y. C. Kim and M. Elimelech, "Thin-film composite pressure retarded osmosis membranes for sustainable power generation from salinity gradients," *Environmental Science & Technology,* vol. 45, pp. 4360-4369, 2011.

[39] A. P. Straub, N. Y. Yip and M. Elimelech, "Raising the bar: Increased hydraulic pressure allows unprecedented high power densities in pressure-retarded osmosis," *Environmental Science & Technology,* vol. 1, pp. 55-59, 2014.

[40] S. E. Skilhagen, J. E. Dugstad and R. J. Aaberg, "Osmotic power production based on the osmotic pressure difference between waters with varying salt gradients," *Desalination,* vol. 220, pp. 476-482, 2008.

[41] K. Gerstandt, K. V. Peinemann, S. E. Skilhagen, T. Thorsen and T. Holt, "Membrane processes in energy supply for an osmotic power plant," *Desalination,* vol. 224, pp. 64-70, 2008.

[42] T. Thorsen and T. Holt, "The potential for power production from salinity gradients by pressure retarded osmosis," *Journal of Membrane Science,* vol. 335, pp. 103-110, 2009.

[43] S. Chou, R. Wang, L. Shi, Q. She, C. Tang and A. G. Fane, "Thin-film composite hollow fiber membranes for pressure retarded osmosis (PRO) process with high power density," *Journal of Membrane Science,* vol. 389, pp. 25-33, 2012.

[44] S. Chou, R. Wang and A. G. Fane, "Robust and high performance hollow fiber membranes for energy harvesting from salinity gradients by pressure retarded osmosis," *Journal of Membrane Science,* vol. 448, pp. 44-54, 2013.

[45] Y. Xu, X. Peng, C. Y. Tang, Q. S. Fu and S. Nie, "Effect of draw solution concentration and operating conditions on forward osmosis and pressure retarded osmosis performance in a spiral wound module," *Journal of Membrane Science,* vol. 348, pp. 298-309, 2010.

[46] Y. C. Kim, Y. Kim, D. Oh and K. H. Lee, "Experimental investigation of a spiral-wound pressure-retarded osmosis membrane module for osmotic power generation," *Environmental Science & Technology,* vol. 47, pp. 2966-2973, 2013.

[47] J. Kim, M. Park, S. A. Snyder and J. H. Kim, "Reverse osmosis (RO) and pressure retarded osmosis (PRO) hybrid processes: Model-based scenario study," *Desalination,* vol. 322, pp. 121-130, 2013.

[48] A. P. Straub, S. Lin and M. Elimelech, "Module-scale analysis of pressure retarded osmosis: Performance limitations and implications for full-scale operation," *Environmental Science & Technology,* 2014.

[49] B. J. Feinberg, G. Z. Ramon and E. M. V. Hoek, "Scale-up characteristics of membrane-based salinity-gradient power production," *Journal of Membrane Science,* vol. 476, pp. 311-320, 2015.

[50] F. Millero and W. Leung, "The thermodynamics of seawater at one atmosphere," *American Journal of Science,* vol. 276, pp. 1035-1077, 1976.

[51] J. Van't Hoff, "The function of osmoitc pressure in the analogy between solutions and gases," *Proc. Phys. Soc. London,* vol. 9, pp. 307-334, 1887.

[52] Koch Membrane Systems Inc., "About hollow fiber membranes," 2015. [Online]. Available: http://www.kochmembrane.com/Learning-Center/Configurations/What-are-Hollow-Fiber-Membranes.aspx. [Accessed June 2015].

[53] Koch Membrane Systems Inc., "About spiral membranes," 2015. [Online]. Available: http://www.kochmembrane.com/Learning-Center/Configurations/What-are-Spiral-Membranes.aspx. [Accessed June 2015].

[54] Statkraft, "Membrane system for pressure retarded osmosis (PRO)". World Intellectual Property Organization Patent WO 2012/084960 A1, 28 June 2012.

[55] T. Y. Cath, A. E. Childress and M. Elimelech, "Forward osmosis: Principles, applications, and recent developments," *Journal of Membrane Science,* vol. 281, pp. 70-87, 2006.

[56] N. Y. Yip and M. Elimelech, "Thermodynamic and energy efficiency analysis of power generation from natural salinity gradients by pressure retarded osmosis," *Environmental Science & Technology,* vol. 46, pp. 5230-5239, 2012.

[57] G. D. Mehta and S. Loeb, "Internal polarization in the porous substructure of a semi-permeable membrane under pressure-retarded osmosis," *Journal of Membrane Science,* vol. 4, p. 261, 1978.

[58] J. R. McCutcheon and M. Elimelech, "Influence of concetrative and dilutive internal concentration polarization on flux behavior in forward osmosis," *Journal of Membrane Science,* vol. 284, pp. 237-247, 2006.

[59] M. F. Naguib, J. Maisonneuve, C. B. Laflamme and P. Pillay, "Modeling pressure-retarded osmotic power in commercial length membranes," *Renewable Energy,* vol. 76, pp. 619-627, 2015.

[60] G. Schock and A. Miquel, "Mass transfer and pressure loss in spiral wound modules," *Desalination,* vol. 64, pp. 339-352, 1987.

[61] R. Perry and D. Green, Perry's Chemical Engineer's Handbook, McGraw-Hill: 6, 1984.

[62] G. B. Van Den Berg, I. G. Racz and C. A. Smolders, "Mass transfer coefficients in cross-flow ultrafiltration," *Journal of Membrane Science,* vol. 47, pp. 25-51, 1989.

[63] A. R. Da Costa, A. G. Fane and D. E. Wiley, "Spacer characterization and pressure drop modelling in spacer-filled channels for ultrafiltration," *Journal of Membrane Science,* vol. 87, pp. 79-98, 1994.

[64] Z. V. P. Murthy and K. Gupta, "Estimation of mass transfer coefficient using a combined nonlinear membrane transport and film theory model," *Desalination,* vol. 109, pp. 39-49, 1997.

[65] C. P. Koutsou, S. G. Yiantsios and A. J. Karahelas, "Direct numerical simulation of flow in spacer-filled channels: Effect of spacer geometrical characteristics," *Journal of Membrane Science,* vol. 291, pp. 53-69, 2007.

[66] C. P. Koutsou, S. G. Yiantsios and A. J. Karahelas, "A numerical and experimental study of mass transfer in spacer-filled channels: Effect of spacer geometrical characteristics and Schmidt number," *Journal of Membrane Science,* vol. 2009, pp. 234-251, 2009.

[67] T. Y. Cath, M. Elimelech, J. R. McCutcheon, R. L. McGinnis, A. Achilli, D. Anastasio, A. R. Brady, A. E. Childress, I. V. Farr, N. T. Hancock, J. Lampi, L. D. Nghiem, M. Xie and N. Y. Yip, "Standard methodology for evaluating membrane performance in osmotically driven membrane processes," *Desalination,* vol. 312, pp. 31-38, 2013.

[68] C. J. Geankopolis, Transport processes and unit operations, Second ed., Boston: Allyn & Bacon, 1983.

[69] J. Kim, M. Wilf, J. S. Park and J. Brown, "Boron rejection by reverse osmosis membranes: National reconnaissance and mechanism study," Desalination and Water Purification Research and Development Program No. 127, US Department

of the Interior, Bureau of Reclamation, Denver, Colorado, 2009.

[70] A. F. Pillsbury, "The salinity of rivers," *Scientific American,* vol. 245, pp. 54-65, 1981.

[71] K. Touati, F. Tadeo and T. Schiestel, "Impact of temperature on power recovery in osmotic power production by pressure retarded osmosis," *Energy Procedia,* vol. 50, pp. 960-969, 2014.

[72] D. E. Wiley and D. F. Fletcher, "Techniques for computational fluid dynamics modelling of flow in membrane channels," *Journal of Membrane Science,* vol. 211, pp. 127-137, 2003.

[73] J. Farkova, "The pressure drop in membrane module with spacers," *Journal of Membrane Science,* vol. 64, pp. 103-111, 1991.

[74] J. Schwinge, P. R. Neal, D. E. Wiley, D. F. Fletcher and A. G. Fane, "Spiral wound modules and spacers: Review and analysis," *Journal of Membrane Science,* vol. 242, pp. 129-153, 2004.

[75] S. Loeb, "Large-scale power production by pressure-retarded osmosis, using river water and sea water passing through spiral modules," *Desalination,* vol. 143, pp. 115-122, 2002.

[76] E. Sivertsen, T. Holt, W. Thelin and G. Brekke, "Modelling mass transport in hollow fiber membranes used for pressure retarded osmosis," *Journal of Membrane Science,* Vols. 417-418, pp. 69-79, 2012.

[77] J. P. MacHarg, "Energy optimization of brackish groundwater reverse osmosis desalination," Texas Water Development Board, Austin, Texas, 2011.

[78] J. M. Chapallaz, H. P. Mombelli and A. Renaud, "Turbines hydraulique: Petites centrales hydrauliques," Office fédéral des questions conjoncturelles, Switzerland, 1995.

[79] I. B. Cameron and R. B. Clemente, "Seawater reverse osmosis with ERI's PX pressure exchanger device: A global survey," *Desalination,* vol. 221, pp. 136-142, 2008.

[80] J. Maisonneuve, P. Pillay and C. B. Laflamme, "Pressure-retarded osmotic power model considering non-ideal effects," *Renewable Energy,* vol. 75, pp. 416-424, 2015.

[81] Q. She, D. Hou, J. Lio, H. G. Tan and C. Y. Tang, "Effect of feed spacer induced membrane deformation on the performance of pressure retarded osmosis (PRO): Implications for PRO process operation," *Journal of Membrane Science,* vol. 445, pp. 170-182, 2013.

[82] A. C. Schonfeld, "Analogy of hydraulic, mechanical, acoustic and electric systems," *Applied Scientific Research,* vol. 3, pp. 417-450, 1954.

[83] J. Horno, C. F. Gonzalez-Fernandez, A. Hayas and F. Gonzalez-Caballero, "Application of network thermodynamics to the computer modelling of nonstationary diffusion through heterogeneous membranes," *Journal of Membrane Science,* vol. 42, pp. 1-12, 1989.

[84] J. Horno, C. F. Gonzalez-Fernandez, A. Hayas and F. Gonzalez-Caballero, "Simulation of concentration polarization in electrokinetic processes by network thermodynamic methods," *Biophysical Journal,* vol. 55, pp. 527-535, 1989.

[85] S. Hong, R. S. Faibish and M. Elimelech, "Kinetics of permeate flux decline in crossflow membrane filtration of colloidal suspensions," *Journal of Colloid and Interface Science,* vol. 196, pp. 267-277, 1997.

[86] P. Raphals, S. Krohn and M. Tampier, "Technologies permettant de réduire l'utilisation du diesel dans les territoires des réseaux autonomes d'Hydro-Québec," Centre Helios, 2006.

[87] D. B. Stewart and W. L. Lockhart, "An overview of the Hudson Bay Marine Ecosystem," *Can Tech Rep Fish Aquat Sci,* vol. 2586, pp. 1-243, 2005.

[88] C. L. Tang and C. K. Wang, "A gridded data set of temperature and salinity for the northwest Atlantic Ocean," *Can Data Rep Hydro Ocean Sci,* vol. 148, pp. 1-45, 1996.

[89] M. Gagnon, "Bilan régional Gaspésie-Nord zone d'intervention prioritaire 20A," Environment Canada, 1998.

[90] Centre d'Expertise Hydrique du Québec, "Historique des niveaux et des débits de différentes stations hydrométriques," [Online]. Available: http://www.cehq.gouv.qc.ca/hydrometrie/historique_donnees/default.asp. [Accessed January 2014].

[91] Environment Canada, "Water survey of Canada," [Online]. Available: http://www.wsc.ec.gc.ca/applications/H2O/index-eng.cfm. [Accessed January 2014].

[92] O. Paish, "Small hydro power: Technology and current status," *Renewable and Sustainable Energy Reviews,* vol. 6, pp. 537-556, 2002.

[93] O. Dzune Mipoung, P. Pillay and L. A. C. Lopes, "Generator selection for rural electrification from renewable energy," in *IEEE International Electric Machines and Drives*, Niagara Falls, 2011.

[94] S. E. Skilhagen, J. W. Brekke, I. Machenbach, M. Havskjold, W. K. Nielsen and S. Guldberg, "Competitiveness of osmotic power in the renewable energy market," in *IDA WC13*, 2013.

[95] T. Pankratz, "PRO plant's basic deisgn complete," *Water Desalination Report,* vol. 49, p. 1, 2013.

[96] Statkraft, "Statkraft halts osmotic power investments," December 2013. [Online]. Available: http://www.statkraft.com/media/news/News-archive/2013/Statkraft-halts-osmotic-power-investments. [Accessed February 2014].

[97] A. Tanioka, K. Saito, M. Irie, S. Zaitsu, H. Sakai, H. Hayashi and A. Kumano, "Power generation by pressure retarded osmosis using concentrated brine from sea water desalination," in *IDA WC13*, 2013.

[98] A. Seppala and M. J. Lampinen, "Thermodynamic optimizing of pressure retarded osmosis power generation systems," *Journal of Membrane Science,* vol. 1999, pp. 115-138, 1999.

[99] S. Loeb, T. Honda and M. Reali, "Comparative mechanical efficiency of several plant configurations using a pressure-retarded osmosis energy converter," *Journal of Membrane Science,* vol. 51, pp. 323-335, 1990.

[100] R. Kleitarp, "The feasibility of a commercial osmotic power plant," Ph.D. dissertation, Department of Hydraulic Engineering, Delft University of Technology, 2012.